UC Berkeley
UC Berkeley Electronic Theses and Dissertations

Title
Understanding Naphthenic Acid Corrosion in Refinery Settings

Permalink
https://escholarship.org/uc/item/40x9d0x7

Author
Patrick, Brian Neil

Publication Date
2015

Peer reviewed|Thesis/dissertation

eScholarship.org Powered by the California Digital Library
University of California

Understanding Naphthenic Acid Corrosion in Refinery Settings

By

Brian Neil Patrick

A dissertation submitted in partial satisfaction of the

requirement for the degree of

Doctor of Philosophy

in

Engineering – Materials Science & Engineering

in the

Graduate Division

of the

University of California, Berkeley

Committee in Charge:

Professor Thomas Devine, Chair
Professor Digby Macdonald
Professor Paulo J.M. Monteiro

Summer 2015

Abstract

Understanding Naphthenic Acid Corrosion in Refinery Settings

by

Brian Neil Patrick

Doctor of Philosophy in Engineering – Materials Science and Engineering

University of California, Berkeley

Professor Thomas Devine, Chair

Naphthenic acid corrosion has plagued refineries for nearly a century. However, the vast majority of naphthenic acid corrosion research to date is solely focused on remediation, and not understanding the fundamental mechanism of corrosion. To further the current state of understanding in order to mitigate corrosion, experiments were performed to address the corrosion mechanism of iron, as well as of the ferrous alloying elements. In addition, electrochemical methods were used to determine the presence of acids within nonpolar solvents, such as a crude. The structure of the acids in solution was studied with FT-IR and Raman spectroscopy to understand how the acids self-associate as a function of temperature, concentration and presence of a metal. The results have yielded that iron corrodes via an etch pitting mechanism. In addition, this work has determined that the mechanism of resistance of chromium and molybdenum are their passive films, and that these metals are susceptible to naphthenic acid attack if the passive films break down. The mechanism of resistance of these elements provides insight into the failure mode of 304 and the 400 series stainless steels in naphthenic acid service. A particular result of interest is that nickel catalytically decomposes naphthenic acids at high temperatures (e.g. 270°C) via a catalytic mechanism. Finally, a palladium hydride reference electrode was developed that functions in aprotic solvents, and an ionic liquid was synthesized that allowed for the electrochemical detection of naphthenic acids in toluene.

Table of Contents

Introduction **1**
- **Crude Oil Refining** **1**
- **Corrosion in the Refining Industry** **4**
- **Naphthenic Acids** **4**
  - Characterizing Naphthenic Acids 6
- **Corrosion Testing** **7**
- **Scope of Research** **9**

Experimental **10**
- **Microgravimetry** **10**
  - Autoclave Descriptions and Procedure 10
  - Data Acquisition 15
  - Microgravimetry Sample Preparation 15
  - Mock Crude Oil Preparation 16
  - In-situ Oxide Stripping 16
- **Total Acid Number** **18**
- **Raman Spectroscopy** **19**
- **Solution Conductivity** **20**
- **Palladium Hydride Reference Electrode** **22**
- **Supporting Electrolyte Selection via Voltammetry** **25**
- **Single Acid Voltammetry** **25**

Results **27**
- **Introduction to Experimental Results** **27**
- **Characterization and Structure of Naphthenic Acids** **27**
  - Total Acid Number 27
  - Raman Vibrational Spectroscopy to Determine Acid Structure 29
- **Microgravimetry** **39**
  - Microgravimetric Measurements of Iron 41
  - Microgravimetry of Iron exposed to Single Acids 47
  - Activation Energy Estimation for Cyclohexanebutyric Acid 50
  - Microgravimetry of Transition Metals 52
  - In-situ Oxide Stripping 62
- **Electrochemical Studies of the Solution** **64**
  - Supporting Electrolytes and Solution Conductivity 65
  - Supporting Electrolyte Voltage Stability 66
  - Palladium Hydride Reference Electrode 69
  - Voltammetric Identification of Single Carboxylic Acid 79

Discussion **83**
- **Raman and FT-IR Study of Structure of Acids in Solution** **83**
  - Introduction 83
  - High Temperature MicroRaman study of individual carboxylic acids in their neat form. 84
  - High Temperature MicroRaman study of naphthenic acid mixtures in neat form. .. 87

High temperature MicroRaman study of naphthenic acid mixtures dissolved in mineral oil. 87
MicroRaman and FT-IR spectroscopic study of a binary mixture of 20% naphthenic acid in mineral oil in the presence of metals 89
Microgravimetry 92
Introduction to Theory 92
Microgravimetry of Iron 96
Effect of Acid Structure and Activation Energy 99
Microgravimetry of Transition Metals 100
Electrochemical Study of Solutions 106
Nature of the Corrosion Reaction 106
Applicability of Electrochemistry 107
IR Drop 109
Cyclic Voltammetry 110
Supporting Electrolytes 112
Palladium Hydride Reference Electrode 115
Naphthenic Acid Identification by Cyclic Voltammetry 122
Conclusions 127
References 130

Table of Figures.

Figure 1. Schematic of atmospheric and vacuum distillation columns (Anon 2014b)..... 3
Figure 2. Plot of corrosion rate vs. TAN for several crude oils (Eberle 2004)..... 7
Figure 3. Drawing of glass Autoclave. Units in inches 11
Figure 4. Cross sectional schematic of glass autoclave 12
Figure 5. Assembled front of stainless steel autoclave 13
Figure 6. Autoclave body without insulation..... 14
Figure 7. Block diagram of stainless steel autoclave..... 14
Figure 8. Schematic of stainless steel autoclave operation (Patrick et al. 2015a) 15
Figure 9 Schematic of microbalance sample prior to experimentation 16
Figure 10. Schematic of Oxide Removal Autoclave. 17
Figure 11. Nickel sample mounted in top of oxide removal autoclave 18
Figure 12. Assembled Oxide Removal Autoclave..... 18
Figure 13. Four point probe inside of Faraday cage 22
Figure 14. Example potentiometric titration of test solution (3 wt. percent naphthenic acid in RLOIP 600)..... 28
Figure 15. Raw Raman spectra showing the gradual change of the relative concentration of monomer and multimer in propionic acid: (A) Room Temperature (B) 40°C (C) 60°C (D) 80°C. (Chakravarti et al. 2013) Reprinted with permission from Energy and Fuels. Copyright 2013 American Chemical Society..... 30
Figure 16. Band-resolved Raman spectrum of propionic acid (1) at room temperature (2) at 80^0C. (Chakravarti et al. 2013) Reprinted with permission from Energy and Fuels. Copyright 2013 American Chemical Society 30
Figure 17. Raman spectra showing the gradual change of the relative concentration of monomer and multimer in cyclohexane acetic acid. (A) Room temperature (B) 100°C (C) 150°C. (Chakravarti et al. 2013) Reprinted with permission from Energy and Fuels. Copyright 2013 American Chemical Society..... 31
Figure 18. Band-resolved Raman spectrum of cyclohexane acetic acid at room temperature (1) and 150^0C (2). (Chakravarti et al. 2013) Reprinted with permission from Energy and Fuels. Copyright 2013 American Chemical Society 31
Figure 19. Raw Raman spectra of neat cyclohexane butyric acid with increasing temperature, where the gradual change of the relative concentration of monomer and multimer are not apparent due to overlapping peaks (A) Room temperature (B) 100°C (C) 150°C. (Chakravarti et al. 2013) Reprinted with permission from Energy and Fuels. Copyright 2013 American Chemical Society..... 32
Figure 20. Band-resolved spectrum of cyclohexane butyric acid (1) at room temperature (2) at 100^0C (3) at 150^0C. (Chakravarti et al. 2013) Reprinted with permission from Energy and Fuels. Copyright 2013 American Chemical Society 33
Figure 21. Plot of the ratios (A) Ratio of linear dimer/cyclic dimer (B) Ratio of monomer/cyclic dimer of the cyclohexanebutyric acid as a function of temperature. (Chakravarti et al. 2013) Reprinted with permission from Energy and Fuels. Copyright 2013 American Chemical Society 33
Figure 22. Full spectra of naphthenic acid mixtures showing the variation of the C=O peak with temperature (A) Room temperature (B) 100°C (C) 150°C (D) 185°C. (Chakravarti et al. 2013) Reprinted with permission from Energy and Fuels. Copyright 2013 American Chemical Society 34

Figure 23. Band-resolved spectrum of naphthenic acid mixtures showing a gradual increase in monomer concentration as a function of temperature: (1) Room temperature (2) 100°C (3) 150°C (4) 185°C. (Chakravarti et al. 2013) Reprinted with permission from Energy and Fuels. Copyright 2013 American Chemical Society..... 35
Figure 24. Plot of the ratios of the molecular species as a function of temperature. (A) Ratio of linear dimer/ cyclic dimer (B) Ratio of monomer/cyclic dimer of the molecular species as a function of temperature. (Chakravarti et al. 2013) Reprinted with permission from Energy and Fuels. Copyright 2013 American Chemical Society..... 36
Figure 25. Band-resolved spectrum of naphthenic acid-mineral oil mixtures at room temperature, with (1) 80% naphthenic acid, (2) 50% naphthenic acid, and (3) 20% naphthenic acid. (Chakravarti et al. 2013) Reprinted with permission from Energy and Fuels. Copyright 2013 American Chemical Society..... 37
Figure 26. Band-resolved spectrum of the 20% naphthenic acid mixtures at (1) Room temperature and (2) 180°C. (Chakravarti et al. 2013) Reprinted with permission from Energy and Fuels. Copyright 2013 American Chemical Society 37
Figure 27. Curve fitted C=O region of NA in the presence of iron at 200°C (1) 2h (2) 3h. (Chakravarti et al. 2013) Reprinted with permission from Energy and Fuels. Copyright 2013 American Chemical Society 38
Figure 28. FT-IR spectrum of the metal naphthenates formed in-situ by the reaction of 20% naphthenic acid with corresponding metal powders held for 5h at 200°C. (Chakravarti et al. 2013) Reprinted with permission from Energy and Fuels. Copyright 2013 American Chemical Society 39
Figure 29. Change in frequency from maximum value vs. temperature for a y 12.5° cut GAPO crystal(Patrick et al. 2015b) 40
Figure 30. Viscosity comparison of RLOP600 base oil using macro viscometer and microbalance (Patrick et al. 2015b) 41
Figure 31. XRD Pattern of iron coated GAPO crystal..... 42
Figure 32. Left. As deposited iron structure 7500x, 5kV. Right. As deposited iron structure 52kx 5kV. (Patrick et al. 2015b)..... 42
Figure 33. Corrosion rate vs. time for iron in 3 wt. percent naphthenic acid at 220°C. Red line indicates average curve fit 42
Figure 34. Corrosion rate vs. time for iron in 3 wt. percent naphthenic acid at 260°C. Red line indicates average curve fit 43
Figure 35. Corrosion rate vs. time for iron in 3 wt. percent naphthenic acid at 270°C. Red line indicates average curve fit (Patrick et al. 2015b)..... 43
Figure 36. Corrosion rate vs. time for iron in 3 wt. percent naphthenic acid at 280°C. Red line indicates average curve fit 44
Figure 37. Corrosion rate vs. time for iron in 3 wt. percent naphthenic acid at 290°C. Red line indicates average curve fit 44
Figure 38. Corrosion rate vs. time for iron in 3 wt. percent naphthenic acid at 320°C. Red line indicates average curve fit 44
Figure 39. Corrosion rate vs. time plot for interrupted tests in 3 wt. percent naphthenic acid at 270°C. Blank: First interrupt. Red: Second Interrupt. Blue: Uninterrupted behavior..... 46

Figure 40. SEM micrographs of corroded surface of iron with progression of time at 270°C in 3 wt. percent naphthenic acid (A) Surface of as-sputtered iron (B) Surface of iron sample after a small positive corrosion rate was measured in Stage II. (C) Iron surface associated with larger positive corrosion in Stage II. (D) Iron surface after achieving steady state corrosion rate for 2.5 hours in Stage III. All images were obtained with a 5 kV beam. See blue curve in Figure 39. (Patrick et al. 2015b) 46
Figure 41 . High magnification SEM image of corrosion pits that formed in iron's surface oxide during early part of Stage II. Image was acquired with a 5 kV electron. (Red curve in Figure 39).(Patrick et al. 2015b) 47
Figure 42. Corrosion rate vs. time for iron in 85 mM cyclohexanecarboxylic acid at 270°C. Red line indicates average curve fit 47
Figure 43. Corrosion rate vs. time for iron in 85 mM cyclohexaneacetic acid at 270°C. Red line indicates average curve fit 48
Figure 44. Corrosion rate vs. time for iron in 85 mM cyclohexanebutyric acid at 270°C. Red line indicates average curve fit 48
Figure 45. Corrosion rate vs. time for iron in 85 mM octanoic acid at 270°C. Red line indicates average curve fit 49
Figure 46. Corrosion rate vs. time for iron in 85 mM dodecanoic acid at 270°C. Red line indicates average curve fit 49
Figure 47. Corrosion rate vs. time for iron in 85 mM stearic acid at 270°C. Red line indicates average curve fit 50
Figure 48. Corrosion rate vs. time for iron in 85 mM cyclohexanebutyric acid at 240°C. Red line indicates average curve fit 50
Figure 49. Corrosion rate vs. time for iron in 85 mM cyclohexanebutyric acid at 270°C. Red line indicates average curve fit 51
Figure 50. Corrosion rate vs. time for iron in 85 mM cyclohexanebutyric acid at 300°C. Red line indicates average curve fit 51
Figure 51. Corrosion rate vs. time for iron in 85 mM cyclohexanebutyric acid at 320°C. Red line indicates average curve fit 51
Figure 52. Corrosion rate vs. time for chromium in 3 wt. percent naphthenic acid at 270°C. Red line indicates curve fit 52
Figure 53. Corrosion rate vs. time for molybdenum in 3 wt. percent naphthenic acid at 270°C. Red line indicates average curve fit 53
Figure 54. Corrosion rate vs. time for Zinc in 3 wt. Percent Naphthenic acid at 200°C. Red line indicates average curve fit 53
Figure 55. Corrosion rate vs. time for copper in 3 wt. percent naphthenic acid at 270°C. Red line indicates average curve fit 53
Figure 56. Corrosion rate vs. time for nickel in 3 wt. percent naphthenic acid at 270°C. Red line indicates average curve fit 54
Figure 57. Corrosion rate vs. time for Silicon in 3 wt. percent naphthenic acid at 270°C. Red line indicates average curve fit. 54
Figure 58. a) Chromium as sputtered 5kV. b) Chromium after 2 hours in 3 wt. NA at 270°C 5kV. 54
Figure 59. a) Molybdenum as sputtered 5kV. b) After 2 hours 3 wt. Percent NA at 270°C 5kV 55

Figure 60. a) Zinc as sputtered 5kV. b) Zinc surface after corrosion in 3 wt. percent naphthenic acid 200°C for 20 minutes 5kV 55
Figure 61. a) Copper as sputtered 5kV. b) Copper surface after corrosion in 3 wt. percent naphthenic acid 200°C for 20 minutes 5kV 55
Figure 62. a) As sputtered nickel surface. b) Edge region of nickel sample after 200 minutes in 3 wt. percent NA at 270°C. c) Central region of nickel sample after 200 minutes in 3 wt. percent NA at 270°C 56
Figure 63. a) Silicon as sputtered 5kV. b) Silicon after 2 hours in 3 wt. NA at 270°C 5kV 56
Figure 64. XRD pattern of chromium crystal as deposited. 57
Figure 65. XRD pattern of chromium crystal after immersion in 3 wt. percent NA at 270°C 57
Figure 66. XRD pattern of copper crystal after immersion in 3 wt. percent NA at 270°C 58
Figure 67. XRD pattern of molybdenum crystal as deposited 58
Figure 68. XRD pattern of molybdenum crystal after immersion in 3 wt. percent NA at 270°C 59
Figure 69. XRD pattern of nickel crystal as deposited 59
Figure 70. XRD pattern of nickel crystal after immersion in 3 wt. percent NA at 270°C 60
Figure 71. XRD pattern of silicon crystal as deposited 60
Figure 72. XRD pattern of silicon crystal after immersion in 3 wt. percent NA at 270°C 61
Figure 73. XRD pattern of zinc crystal as deposited 61
Figure 74. XRD pattern of zinc crystal after immersion in 3 wt. percent NA at 270°C.. 62
Figure 75. Results from FT-IR spectrometry experiments on powder samples. * signifies active corrosion occurring during test 62
Figure 76. a) Ground uncorroded iron surface after immersion in acid-free oil for 4 h at 270°C. 5kV. b) Ground iron surface after immersion in 3 wt. percent naphthenic acid for 4 hours at 270°C. 5kV 63
Figure 77. a) Ground uncorroded chromium surface after immersion in acid-free oil for 4 h at 270°C. 5kV. b) Ground chromium surface after immersion in 15 wt. percent naphthenic acid for 4 hours at 270°C 5kV 63
Figure 78. a) Ground uncorroded molybdenum surface after immersion in acid-free oil for 4 h at 270°C. 5kV. b) Ground molybdenum surface after immersion in 15 wt. percent naphthenic acid for 4 hours at 270°C. 5kV 64
Figure 79. a) Ground uncorroded copper surface after immersion in acid-free oil for 4 h at 270°C. 5kV. b) Ground copper surface after immersion in 3 wt. percent naphthenic acid for 4 hours at 270°C. 5kV 64
Figure 80. a) Image of ground nickel surface after immersion in acid-free oil for 4 h at 270°C. 5kV. b) Image of ground nickel surface after immersion in 3 wt. percent NA for 4 hours at 270°C. 5kV 64
Figure 81. Randles equivalent circuit. R_s=Solution resistance, R_p=Polarization resistance, C_p=Double layer capacitance 65
Figure 82. Voltammogram for stability of 0.4M $P_{6,6,14}$ [Cl] in Benzyl Benzoate 67
Figure 83. Voltammogram for stability of 0.4M $P_{6,6,14}$ [Br] in Benzyl Benzoate 67
Figure 84. Voltammogram for stability of 0.4M $P_{6,6,14}$ [BIS] in Benzyl Benzoate 68
Figure 85. Voltammogram for stability of 0.4M $P_{6,6,14}$ [DCN] in Benzyl Benzoate 68

Figure 86. Voltammogram for stability of 0.4M $P_{6,6,14}$ [TKIS] in Benzyl Benzoate 68
Figure 87. Potential vs. pH diagram of PdH vs. SCE electrode in commercial pH buffers containing 0.1M KCl 73
Figure 88. Open circuit potential of PdH vs. SCE in pH 4 buffered 0.1M potassium chloride in water. Potential drift of 10 mV over 8 hours 73
Figure 89. Open circuit potential of PdH electrode vs. modified SCE in 0.2M TBAP in CAN 73
Figure 90. I vs. V plot of β-PdH UME in 0.2M [bmim][TFB] in DCM saturated with Forming Gas during polarization from 0 to +10 mV to -10 mV at a rate of 10 mV/s. The curve obtained by sweeping the potential in the positive direction was identical to the curve obtained by sweeping the potential in the negative direction. 74
Figure 91. I vs. V plot of ß-PdH UME in 0.2M [bmim][TFB] in DCM saturated with forming gas during 10mV small polarizations from open circuit at a rate of 10 mV/s, cathodic scan first 74
Figure 92. I vs. V plot of ß-PdH UME in 0.1M HCl saturated with forming gas during 10mV small polarizations from open circuit at a rate of 10 mV/s, anodic scan first. Platinum foil counter/reference electrode 75
Figure 93. Cyclic voltammogram of Pt UME WE immersed in 0.2M [bmim][TFB] in DCM with 1 mM ferrocene, 1 mM anthraquinone, and 1 mM decamethylferrocene. The cell was a two electrode cell containing a 1 in2 PdH RE/CE 75
Figure 94. IR-correction of CV presented in Figure 93 76
Figure 95. Background subtracted current response of first and last pulses from chromoamperometry experiments on PdH microelectrode. ±500mV pulses for 5 seconds each 76
Figure 96. I/I_{limit} vs. $t^{1/2}$ for multistep chronoamperometry of PdH microelectrode to 10 ±500mV pulses for 5 seconds each. Only first and last pulses are shown*. I_{limit} was taken as current at $t=t_{max}$ 77
Figure 97. Background subtracted current response of first and last pulses from chromoamperometry experiments on PdH microelectrode. ±500mV pulses for 50 seconds each 77
Figure 98. I/I_{limit} vs. $t^{1/2}$ for multistep chronoamperometry of PdH microelectrode to 10 ±500mV pulses for 50 seconds each. Only first and last pulses are shown*. I_{limit} was taken as current at $t=t_{max}$ 78
Figure 99. Background subtracted current response of first and last pulses from chromoamperometry experiments on PdH microelectrode. ±500mV pulses for 500 seconds each 78
Figure 100. I/I_{limit} vs. $t^{1/2}$ for multistep chronoamperometry of PdH microelectrode to 10 ±500mV pulses for 500 seconds each. Only first and last pulses are shown*. I_{limit} was taken as current at $t=t_{max}$ 79
Figure 101. Voltammogram of 0.5 mM benzoic acid in 0.3M $P_{6,6,14}$[TKIS] in toluene after background subtraction 80
Figure 102. Voltammogram of 0.5mM cyclohexaneacetic acid in 0.3M $P_{6,6,14}$[TKIS] in toluene after background subtraction 80
Figure 103. Voltammogram of 0.5mM cyclohexanebutyric acid in 0.3M $P_{6,6,14}$[TKIS] in toluene after background subtraction 81

Figure 104. Voltammogram of 0.5mM dodecanoic acid in 0.3M $P_{6,6,14}$[TKIS] in toluene 81
Figure 105. Voltammogram of 0.1mM stearic acid in 0.3M $P_{6,6,14}$[TKIS] in toluene..... 82
Figure 106. Schematic representation of the probable mechanistic pathways, forming different soluble corrosion products. . (Chakravarti et al. 2013) Reprinted with permission from Energy and Fuels. Copyright 2013 American Chemical Society.. 84
Figure 107. Schematic of the (a) monomer, (b) linear dimer/multimer, and (c) cyclic dimer configurations. . (Chakravarti et al. 2013) Reprinted with permission from Energy and Fuels. Copyright 2013 American Chemical Society 84
Figure 108. Structures of typical NAs studied, where z= -2. . (Chakravarti et al. 2013) Reprinted with permission from Energy and Fuels. Copyright 2013 American Chemical Society 86
Figure 109. Time dependence of Fe-naphthenate formation[a]. (Chakravarti et al. 2013) Reprinted with permission from Energy and Fuels. Copyright 2013 American Chemical Society 90
Figure 110. 2d representation showing dipole production from piezoelectric effect.(Ramadan et al. 2014)..... 93
Figure 111. Simplified schematic of crystal microbalance experimental setup(Kumar 2000) 94
Figure 112. Conductance vs. frequency for crystal microbalance upon loading. (A. Langhoff) 94
Figure 113. Schematic diagram of plausible mechanism of the corrosion at the interface of iron and naphthenic acid..... 98
Figure 114. Arrhenius plot of corrosion rate of cyclohexanebutyric acid on iron..... 100
Figure 115. Example I-V curve from cyclic voltammetry experiment at macroelectrode 111
Figure 116. Example I-V curve from cyclic voltammetry experiment at UME..... 112
Figure 117. Schematic of four point probe measurement. Current is driven across the outer electrodes and potential drop is measured across the inner electrodes..... 113
Figure 118. Relationship between calculated pKa and corrosion rate..... 125
Figure 119. Steady State Current vs. Experimental Corrosion Rate..... 126

To Suann Kessler,
for your unwavering patience and support.

Introduction

Crude Oil Refining

Crude oil refining is an elaborate process that involves separating various economically significant petroleum products from a mixture, and processing them into useful products for various purposes. Crude oil is extremely complex, and contains more than 11,000 individual components. (Hughey et al. 2002) While the vast majority of the species in crude are hydrocarbons, there is a small amount of compounds that contain oxygen, sulfur, nitrogen, and metal ions. (Fahim et al. 2010) The hydrocarbons present in crude oil are primarily paraffinic, although there are some naphthenes and simple and complex aromatic structures. Marshall et al. showed via mass spectrometry that the composition of crude is extremely complex, where they identified 11,127 separate species in a crude sample. (Hughey et al. 2002) Given the variety of species present in crude and the fact that the number of isomers increases greatly with carbon chain length, it is not surprising that characterizing crude oil is a difficult task. To understand what is present in crude, an overview of each of the types of non-hydrocarbon constituents present is included below.

Sulfur species generally are present in crude in the range of 0.05-10 wt. percent, with the vast majority of crudes falling in the 1-4 wt. percent range. (Fahim et al. 2010) The identity of the sulfur species ranges from elemental sulfur, to hydrogen sulfide, carbonyl sulfide, as well as inorganic and organic sulfur compounds. (Ho et al. 1974) The majority of the species are organic sulfur compounds in the form of thiols or polycyclic sulfides. At high temperature, many of the organic sulfides either react directly with steel or break down forming hydrogen sulfide, which is very corrosive to steels. (Hau 2009)

Oxygen compounds are found in lower concentrations than sulfur species in oil, and generally represent two wt. percent of the crude's weight. (Fahim et al. 2010) The structures of oxygen compounds are varied, and include alcohols ethers, carboxylic acids, phenolic compounds, ketones, esters and anhydrides. Most of these species are minimally corrosive, however the carboxylic acids, which are as a group called naphthenic acids, pose severe corrosion problems during the refining process. (Turnbull et al. 1998)

Nitrogen compounds in crude are found in very small amounts, accounting for 0.05-2 wt. percent of the mixture. (Fahim et al. 2010) The nitrogen compounds as a whole are generally more stable than the corresponding sulfur species. The most common nitrogen containing structures in crude are quinolones and pyrroles. (Fahim et al. 2010) The nitrogen containing species are generally noncorrosive, but they often poison catalysts and are present as contaminants in petroleum based products. (Gary & Handwerk 1994)

Metallic compounds are found in nearly all crudes in small quantities, generally between 1-1000 ppm. (Gary & Handwerk 1994) The metal containing species appear as both inorganic metal salts, as well as oil-soluble metalorganic compounds. (Fahim et al. 2010) The inorganic metal salts are primarily chloride salts based upon sodium, magnesium, potassium and calcium ions. The metalorganic species in a crude are generally zinc, titanium, vanadium, nickel, copper, and iron based. (Fahim et al. 2010) The inorganic salts undergo hydrolysis during the distillation process, releasing corrosive acid gas, and many of the metalorganic species poison catalysts throughout the refinery. (Gary & Handwerk 1994)

The final non-hydrocarbon species in crude are asphaltenes and resins. (Fahim et al. 2010) These species have a very high molecular weight and a high concentration of heteroatoms. However, most of the asphaltenes and resins are solid, do not melt, and leave a residue upon heating. The asphaltenes species cause severe fouling problems within the refinery, especially in the furnace for crude distillation and the thermal cracking units. (Fahim et al. 2010)

Geography has a significant influence on both the species present within a crude and the reactivity of those species. (Meredith et al. 2000) Depending on the particular origin of the crude, it will have varying concentrations of each of the non-hydrocarbon constituents mentioned above. In particular crudes from China, Venezuela, India, Russia, and some fields in California have high concentrations of oxygen containing compounds in the form of carboxylic acids. (Fahim et al. 2010) In addition, as global crude supplies are decreasing, the crudes that contain more reactive and difficult to process species are being refined. The reason for lower quality crudes being processed is primarily economic, as crudes that are more difficult to process trade at lower prices. (Bacon & Tordo 2005)

The refinery is a very complex system; however, this research focuses on the very beginning of the process in the crude distillation unit (CDU) where naphthenic acid corrosion occurs. In essence, the CDU is a large fractional distillation column. The crude oil is heated above its boiling point, and is then separated based upon the boiling points of the constituent components. A more technical description of the processes that occur in the CDU is included below.

The refining process begins with crude oil stored in tanks after being transported from the well to the refinery, normally via pipeline or supertanker. The crude is pumped from the storage tank into a desalter. The desalter is used to remove inorganic salts that are present in water droplets emulsified by the oil. (Fahim et al. 2010) In the desalter, the crude oil is heated and mixed with water, which then forms an emulsion, while the inorganic metal salts are solvated by the water. Next, demulsifiers are added to the mixture and the solution is separated using electrostatic water separation. (Abdel-Aal et al. 2003) The separation of water soluble species prevents the inorganic metal salts from undergoing hydrolysis in the distillation column, which ultimately avoids the creation of corrosive acid gasses and solid hydroxides. (Piehl 1959) After the water is extracted, the

oil is removed from the desalter and heated for introduction into the atmospheric distillation column.

During the heating process, the crude is heated to between 330-385°C in a furnace in order to cause partial vaporization. (Gary & Handwerk 1994) The crude is then transferred into the flash zone near the bottom of the atmospheric column, which is approximately 50m tall and contains 30-50 trays.(Simanzhenkov & Idem 2003) The trays remove the partially refined products. A schematic of the atmospheric and vacuum distillation columns can be seen in

Figure 1, illustrating how to the process occurs. (Anon 2014b) The vaporized portion of the crude travels up the column with its constituents condensing out based upon their boiling point. Each tray only captures hydrocarbons within a small range of boiling points, allowing many different compounds to be separated out. Commonly, bubble trays are used for capturing the hydrocarbons with a particular boiling point. (Anon 2014b) There are pressure and temperature gradients along the length of the column, which allow for condensation of products with a specific boiling point range between each tray. (Gary & Handwerk 1994) The precipitate caught by a particular tray, or side cut, is then brought to another portion of the refinery for subsequent processing.

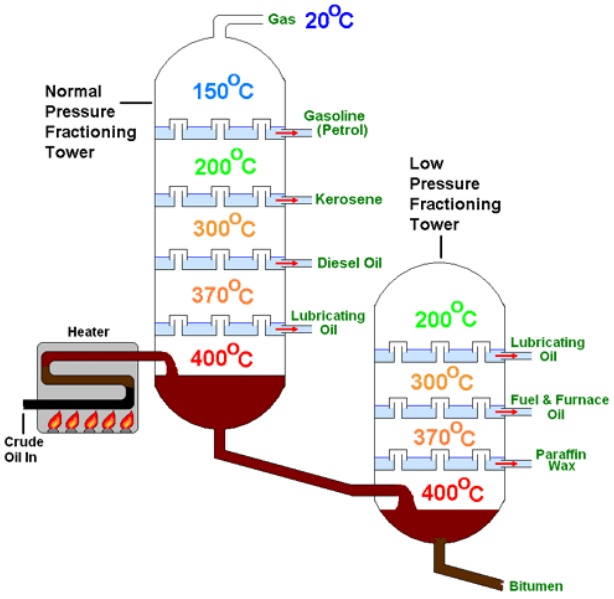


Figure 1. Schematic of atmospheric and vacuum distillation columns (Anon 2014b)

The heavy ends of the crude that have a high boiling point and did not volatilize in the atmospheric distillation fall to the bottom of the column, as shown in

Figure 1. These heavy ends are the atmospheric residue, which are pumped to another furnace and heated again to 380-415°C. (Fahim et al. 2010) The additional heating again partially vaporizes the oil, and the oil is then introduced into the flash zone of the column. Steam is injected during the heating process to prevent coking inside the furnace tubes, as well as to increase the surface area of the oil in order to increase yield. (Fahim et al. 2010) The pressure inside of the vacuum distillation unit is generally 25-40

mmHg, which is approximately 30 times lower than the atmospheric unit. (Gary & Handwerk 1994) The products are removed via side cuts from the vacuum distillation column and are subsequently processed in other parts of the refinery. The residual liquid at the bottom of the vacuum distillation column is reclaimed using a visibreaker, coker, or deasphalter. (Simanzhenkov & Idem 2003)

Corrosion in the Refining Industry

A landmark study by NACE in 1998 estimated the annual cost of corrosion during petroleum refining to be a staggering 3.7 billion USD, which accounting for inflation increases to 5.3 billion USD in 2015. (Virmani 2003) In the United Kingdom, corrosion in the oil and chemical industry accounted for over 13 percent of all corrosion related costs. (Kruger 2011) If the proportions from the U.K. carry over to the United States, then nearly 36 billion dollars were spent in 1998 combatting corrosion in the chemical and oil industries. Even with such a large sum being spent combatting corrosion, catastrophic failures still occur. Refinery failures often cause fatalities, environmental pollution, and severe financial burdens. While corrosion and failures occur in many places in the oil industry, refinery failures draw much attention due to their scale and severity. Catastrophic failures due to corrosion in oil refineries are surprisingly common, with the Silver Eagle Refinery in 2009, the Regina Refinery in 2011, and Richmond Refinery in 2012 all being caused by corrosion (Anon 2014a; Anamet 2013; Anon 2013). Given the number and extent of refinery failures just in the past five years in North America, it is not surprising that corrosion has been a problem for refiners for many years, with the first literature report nearly 60 years ago. (Derungs 1956) This work will focus on one particular type of refinery corrosion that occurs in the crude distillation unit, the corrosion caused by naphthenic acids.

Naphthenic Acids

Given the large concentration of non-hydrocarbon species present in crude, as well as the high temperatures present inside of the distillation columns, it is not surprising that corrosion poses a significant problem. One of the primary aggressive species present that causes corrosion issues is the naphthenic acids. (Fahim et al. 2010; Dettman et al. 2009) In order to address the issue of naphthenic acid corrosion, first understanding the structure and behavior of these acids is imperative. Naphthenic acids are described as aliphatic acids with zero to three fused cycloalkane rings, an alkane chain, and a terminal carboxylic acid group. (Qu et al. 2007) The general formula a naphthenic acid is $C_nH_{2n+z}O_2$, where z is the hydrogen deficiency (a negative even integer). (Barrow et al. 2003) Many possible structures can be generated from a single hydrogen deficiency, and the number of possible isomers increases rapidly with molecular weight. As many different structures of naphthenic acids are possible, the geographic region the crude forms has a great influence on the particular acid structure distribution. (Behar & Albrecht 1984) The differing naphthenic acid structure is related to the biodegration of the oil, which occurs as the oil field matures. (Whitby 2010)

Naphthenic acids are noncorrosive at room temperature, and become increasingly corrosive at temperatures where refining occurs. For carbon steel, the acids are initially corrosive in the range of 180-220°C, then become increasingly corrosive, with a maximum between 280 and 385°C, and finally breakdown above 400°C. (Gutzeit 1977; Dettman et al. 2009) The acid breakdown above 400°C is due to thermal decarboxylation of the acid. (Yang et al. 2013) The reason that naphthenic acids are problematic in refineries is that the distillation columns operate primarily between 250-400°C region. (Slavcheva et al. 1999) To compound the problem, naphthenic acids volatilize along with the hydrocarbons in the CDU, and then either condense on the distillation column walls or on a narrow range of trays. (Slavcheva et al. 1999) The condensation of naphthenic acids creates microenvironments in the refinery with much higher concentrations of naphthenic acids than the bulk crude.

The overall corrosion reaction of naphthenic acid with steel can be described in the following manner. Iron is the major component of carbon steel (approx. 98-99.8% Fe), which is the material of construction for the majority of the refinery. It is well known that the naphthenic acids present in crude attack steel and the steel in contact with the crude is destroyed, creating a soluble corrosion product that is released into the oil stream. (Derungs 1956) The corrosion process has been studied, and it amounts to an endothermic metal-ligand reaction between iron and naphthenic acid in oil media.(Stahl & Ke 2002) The overall reaction can be expressed as follows: (Slavcheva et al. 1999)

$$Fe + 2RCOOH \leftrightarrow Fe(RCOO)_2 + H_2 \quad \{1\}$$

The reaction shown in *equation 1* involves two naphthenic acid molecules coordinating to a single iron atom, which forms an oil soluble iron naphthenate, and hydrogen gas is released. The corrosion product is $Fe(RCOO)_2$, where R is the cycloalkane portion of the acid, and is highly soluble in oil. The corrosion reaction results in a steady depletion of Fe from the surface until the one of the reactants is consumed. In practice, the corrosion reaction only ceases when either steel is corroded through, or the acid in the crude is at a concentration below the threshold of the reaction. Naphthenic acid corrosion is generally worst within the vacuum distillation column, where the temperatures of the condensates are within the 250-400°C range. (Derungs 1956; Piehl 1988; Slavcheva et al. 1999) Due to the condensation, corrosion is worst in a narrow band in the column. The areas subject to the most severe corrosion are the bubble caps, valve trays, and the side cuts pipes coming from the column. (Piehl 1988) The morphology of naphthenic acid attack is generally described as a localized attack similar to pitting, with sharp edged holes in the metal surface. (Babaian-Kibala 1993) In some areas, such as those subjected to condensed naphthenic acid vapors, the morphology is described as similar to a plastically deformed metal with an orange peel type behavior. (Babaian-Kibala 1993)

To prevent corrosion, there are several techniques that refineries employ. One of the most effective is pre-topping the oil. (Breen 1974) Pre-topping is a process that occurs before distillation, in which the oil is heated to high temperatures in order to

breakdown the acids. However, pre-topping requires a large amount of energy and is an expensive proposition for refiners. Another technique that has been used with success is the addition of corrosion inhibitors, which prevent naphthenic acid from contacting the metal. (Babaian-Kibala 1994; Saxena 2013) The most common technique used to mitigate naphthenic acid corrosion is blending. (de Bruyn 1998; Qu et al. 2006; Qu et al. 2007) During a blending process, a corrosive high acid crude is mixed with a non-corrosive crude in order to reduce the corrosion occurring to a manageable level. However, it has been reported that blending may in fact cause additional problems during refining if the crude being used for blending contains large quantities of sulfur compounds or other corrosive agents. (Dettman et al. 2010) Finally, the most effective method of naphthenic acid corrosion mitigation is upgrading the metallurgy of the refinery to more corrosion resistant alloys. (Stahl & Ke 2002; Anon 1977; X. Q. Wu et al. 2004)

Characterizing Naphthenic Acids

As naphthenic acid corrosion is a serious problem in refineries, there has been a significant research thrust to identify the acids present in a crude. (Hsu et al. 2000; Rogers et al. 2002; Saab et al. 2005; Da Campo et al. 2009; Mohammed & Sorbie 2009) However, identification of all of the naphthenic acids is a very difficult task, as crude contains many different compounds with similar sizes and shapes. An outline of the different techniques that have been applied, as well as their strengths and weaknesses are below.

One of the methods often used by oil companies to determine the corrosivity of a crude before refining is the total acid number, or TAN. (ASTM Standard 2009) TAN is a potentiometric titration in which a small sample of a crude is dissolved in a mixture of toluene and 2-propanol. The oil and titration solvent mixture is then titrated potentiometrically with alcoholic potassium hydroxide, against a silver-silver chloride referenced glass pH electrode. The titration is performed until the potential of the pH electrode has achieved a value equivalent of a strong basic solution (-300mV vs. Ag/AgCl). TAN is then calculated using the difference between the two points of inflection in the titration curve, and is reported in mg of KOH per gram of oil. A TAN value below 0.5 is considered noncorrosive, while anything above is considered a high acid, corrosive crude.

TAN has developed a poor reputation in the oil industry due its mediocre ability of determining the corrosivity of oil. (Slavcheva et al. 1999; Yépez 2005; Dettman et al. 2009) The plot in

Figure 2 shows the relationship between TAN and corrosivity for several crudes, and illustrates the poor correlation.(Eberle 2004) There have been several explanations for the poor correlation, including reaction between the metal naphthenate and potassium hydroxide, as well as reactions with other acidic species in the crude sample. However, there has been very little work in to evaluate the other possible reacting species.

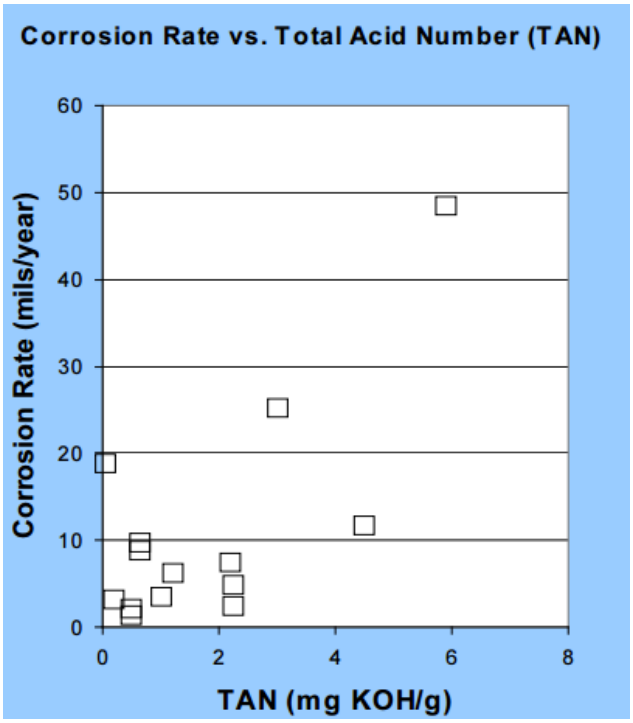


Figure 2. Plot of corrosion rate vs. TAN for several crude oils (Eberle 2004)

Throughout the years, there have been many attempts to identify the acids within crude oil and to determine which acids are responsible for corrosion. The techniques that have been used include nuclear magnetic resonance (NMR), gas chromatography (GC), many types of mass spectrometry (MS), Fourier transform infrared spectroscopy (FT-IR), and high performance liquid chromatography (HPLC). (Mohammed & Sorbie 2009; Hsu et al. 2000; Saab et al. 2005; Tomczyk & R.E. 2001; Rogers et al. 2002) These studies have been successful in identifying a plethora of acids that are present within the crude oil, but they can only identify the size of the molecule and the overall structure based upon the molecular formula. (Barrow et al. 2003) The aforementioned techniques all lack the ability to distinguish isomers, as well as the strength and reactivity of the acids. (Fan 1991; Seifert & Teeter 1970; Holowenko et al. 2002; Hughey et al. 2002) The reason for the difficulty in d etermining corrosivity is that the position of the carboxylic acid group with respect to the rest of the molecule has a large effect on the reactivity of the acid. (Davis & Hetzer 1958). However, the work that has been done using these techniques shows the range of variability in the composition of naphthenic acids. Seifert et al. showed the presence of aromatic structures within naphthenic acids, in addition to just cycloalkane structures. (Seifert & Teeter 1970) The presence of additional aromatic structures makes determination of corrosivity from the above-mentioned techniques even more difficult.

Corrosion Testing

In order to determine the corrosivity of a crude without performing the complex characterization techniques noted in the previous section, bulk corrosion measurements on coupons are commonly used. The bulk corrosion tests are performed using standard

coupons or powders in various types of autoclaves. Hau et al. used iron powders in order to determine whether corrosion took place by measuring the concentration of dissolved iron in the oil. (Hau et al. 1999) Other researchers have used various test geometries, including high velocity impingement, rocking autoclaves, rotating autoclaves, and flow loops to study naphthenic acid corrosion. (X. Wu et al. 2004; Gutzeit 1977; Slavcheva et al. 1999; Kanukuntla et al. 2009) Each of the previously mentioned autoclave configurations attempts to emulate a particular condition that is found within the refinery. (Slavcheva et al. 1999)

The majority of research that has been performed to date has looked at the effect of temperature, pressure, state, time of exposure, flow, and to a limited extent the structure of the acid. The effect of temperature was studied extensively by Gutzeit and Turnbull, which established the temperature range for naphthenic acid attack as well as guidelines for corrosion prevention. (Gutzeit 1977; Slavcheva et al. 1999) The effect of pressure on NAC was found to be minimal, and is believed to cause a significant effect only changing the physical state of the acid. (Slavcheva et al. 1999; Gutzeit 1977) The effect of the physical state of the acid has also been extensively studied, and the studies have found that naphthenic acids are most corrosive near their boiling points and when in the liquid/condensed state. (Derungs 1956; Gutzeit 1977; Turnbull et al. 1998; Dettman et al. 2009; Dettman et al. 2010) The effect of exposure time also has been found to influence corrosion rates. The effect of time was studied by Yu et al. who found that the corrosion rate of a sample exposed to naphthenic acid decreases with increasing exposure times in a mock crude. (Yu et al. 2008) Turnbull studied the effect of time and attributed it was due to thermal decarboxylation occurring during the test, but was not able to confirm this hypothesis. (Turnbull et al. 1998) The effect of flow has been studied in several configurations that emulate conditions present in a refinery. The flow rate studies found that high flow rates in general product higher corrosion rates, which may be due either to sulfide scale inhibition, or to increased diffusion rates.(X. Q. Wu et al. 2004; N. Wu et al. 2004; X. Wu et al. 2004)

To date, there have been several attempts to correlate the structure of the acid to its corrosivity, however identifying a relationship has been very difficult using conventional means. Turnbull looked at the corrosivity of a series of acids with one ring, and found a maximum corrosivity with a carbon number of 9. (Turnbull et al. 1998) Dettman et al. also studied the influence of structure extensively, and found that the boiling point of the structure has the biggest influence on corrosivity, with the lowest boiling point acid being the most corrosive.(Dettman et al. 2009) Additionally, they found that acids with more than one ring are generally less corrosive than their single ringed equivalent. (Dettman et al. 2009; Dettman et al. 2010) In addition, Dettman et al. found that for corrosion of coupons placed above the oil, naphthenic acid corrosion did not occur until the temperature was approximately at the acid's boiling point. (Dettman et al. 2009; Dettman et al. 2010)

Much empirical work has also been performed in order to determine which alloys are resistant to naphthenic acid corrosion. The main purpose of studies using corrosion resistant alloys was to provide guidelines for refiners to know when to upgrade the metallurgy, and which alloy to use. The alloys most commonly used within the CDU are

carbon steel, low alloy Cr steels, and the 300/400 series stainless steels. Other high alloy corrosion resistant materials such as Hastelloy and Inconel are used to a lesser extent, owing to their high cost. 410 stainless steel is regarded to be more resistant to naphthenic acids than standard carbon steel, but it is not sufficient for high acid crude exposure. (Derungs 1956; Gutzeit 1977) In general, the chromium containing alloys are more resistant than carbon steels to naphthenic acid corrosion, but research has found that iron-chrome alloys fail due to pitting in many circumstances. (Nugent & Dobis 1998) Within the 300 series of stainless steels, the addition of roughly 2.5 wt. percent molybdenum for 316 shows a vast improvement over 304, as the behavior of 304 stainless steel is erratic. (Piehl 1988; Derungs 1956; Farraro & Stellina Jr. 1996). 316 and 317 stainless steel have long been the material of choice in high TAN applications due to its consistent corrosion resistance. (Derungs 1956; Gutzeit 1977; Slavcheva et al. 1999; Breen 1974; Farraro & Stellina Jr. 1996) In severe service, high nickel alloys such as Hastelloy C276 are employed, but these exotic alloys are only applied in rare circumstances due to their high cost. (Farraro & Stellina Jr. 1996)

Scope of Research

Despite the number of studies that have been done to assess the naphthenic acid corrosion resistance of alloys and to identity the acids present in crude oil, there is little information available about the mechanism of the attack on refinery materials by naphthenic acids. In addition, currently there are not any economical and reliable methods for determining the corrosivity of a crude prior to actually processing it in the refinery.

To approach the study of naphthenic acid corrosion of refinery materials, two experimental paths were taken. The first is based upon using in-situ corrosion experiments to determine the kinetics of the corrosion reaction on refinery materials. This experimental path utilizes the crystal microbalance technique. The second path is based upon identifying the corrosive acids present inside of a crude oil. Raman and FT-IR spectroscopy were used to understand the coordination of naphthenic acids in oil, and electrochemical techniques were used to determine the reactivity of these acids based upon their structure.

The primary scientific question this dissertation seeks to address is: How does the reaction of naphthenic acid with iron and ferrous alloying elements proceed? In addition, this research attempts to develop a technique that can be applied to determine the corrosivity of the acids present in a crude prior to refining. Other authors have done significant research towards determining the identity of the species present in crude and the conditions in which the corrosion occurs. To further the state of understanding, this work seeks to determine indicators for when naphthenic acids in a crude should be corrosive.

Experimental

Microgravimetry

Autoclave Descriptions and Procedure

Glass Autoclave

Initial in-situ corrosion experiments were performed using a custom made two-part borosilicate glass cell (Adams & Chittendon Scientific Glass) including a Hastelloy C276 joint. Check valves (Swagelok) were used to prevent pressure buildup as well as prevent oxygen contamination in the autoclave. The bottom portion of the autoclave held 75 mL of solution, and was equipped with a fritted glass bubbler for degassing of the oil prior to experimentation. The top portion of the autoclave was fitted with two inlet/outlets, as well as ground glass connections. An insulated heating mantle (Cole-Parmer) was used in conjunction with a PID controller to set the testing temperature in the lower portion of the autoclave. A heating tape (Cole-Parmer) was used in conjunction with an on/off controller to regulate the temperature of the upper portion of the autoclave. The top and bottom portions of the autoclave have independent gas inlets and lift check valves. All tubing was ¼" PFTE and all connections were made with 316L Swagelok connectors with PFA ferrules. Seals between the glass/metal interfaces were reinforced with fireproof clay (McMaster Carr) on the outside edge of the seal. A scored glass disc was used as a breakable gasket that separated the oil from the sample during the preheating stage of the experiment. The disc was scored using a silicon carbide glasscutter to ensure a clean break of the gasket with minimal force.

A high temperature oil and gas gasket maker (Permatex) was used to seal the top of the sample holder to the autoclave, and the seal was maintained by placing a five-pound weight on top of the autoclave. A syringe was inserted into a PFTE feed through located at the gas outlet of the bottom portion of the autoclave to allow for aliquots to be taken throughout the experiment. Drawings, as well as pictures of each of the components of the autoclave are included in Figure 3 and
Figure 4. Heated oil was admitted into the sample's chamber by breaking the scored disc.

A Maxtek cool drawer sensor head was used in conjunction with a Maxtek RQCM system for crystal microbalance measurement of weight changes of thin film samples that had been deposited onto gallium orthophosphate crystals. The sensor head was electroplated with platinum before use in order to prevent corrosion of the 304SS base material using a chloroplatinic acid bath and a nickel adhesion layer. The procedure used to electrodeposit platinum is described by Baumgartner. (Baumgartner & Raub 1988)

During experimentation, test solution was added to the bottom of the autoclave such that after inserting the sample, the solution level would rise 15 mm above the top of the sample holder (~75 mL). The metal joint, glass gasket, and top portion of the

autoclave were then placed into position and sealed together. The solution was then degassed with house nitrogen for a minimum of 4 hours at 80°C at a high rate without foaming over. Throughout the test, the solution was stirred with a glass coated magnetic stir bar at a slow rate (300 rpm) in order to maintain homogeneity in the solution. The sample was inserted into the sample holder, and then put into the top portion of the cell after degassing was complete. The sample holder portion of the autoclave was then degassed with house nitrogen for five minutes. Both portions of the autoclave were then brought to the testing temperature, and thermal equilibrium was established. After thermal equilibrium was established, the holder was pressed through a glass membrane to admit the test solution into the sample chamber. The crystal shunt capacitance was tuned using the RQCM interface, and data was collected at a rate of 300 points/minute. The sample was promptly removed after completion of the experiment, cooled to room temperature, and cleaned by sonication in hexane.

For selected tests samples of the solution were taken throughout the experiment. To remove an aliquot, a glass syringe was used in conjunction with a 10-gauge 8 in. long stainless steel needle. The glass syringe was locked onto the needle and a two mL sample of the solution was extracted from the autoclave. The oil was cooled in the syringe, and then stored in glass sample vials.

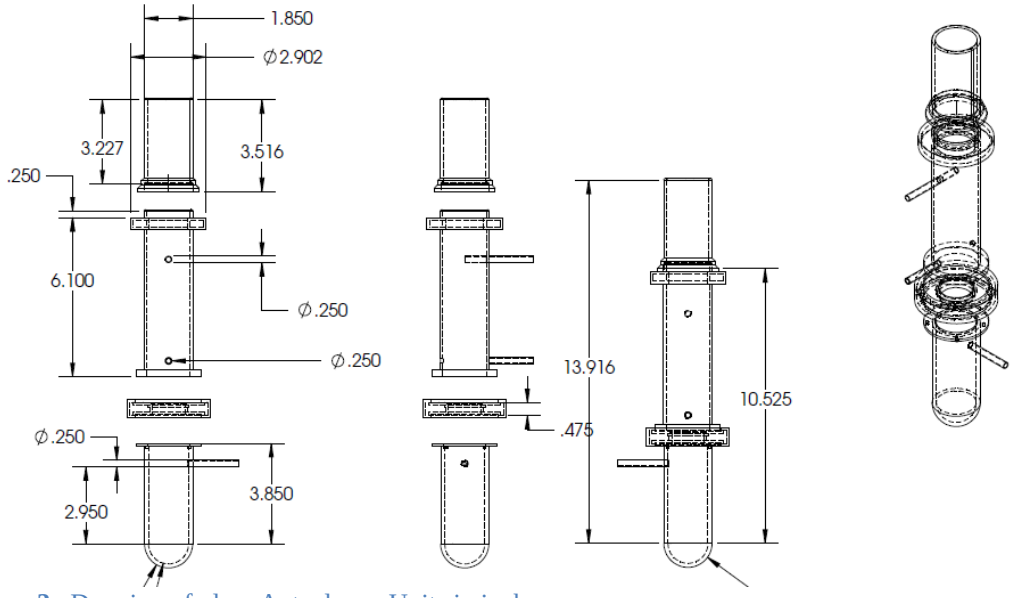


Figure 3. Drawing of glass Autoclave. Units in inches

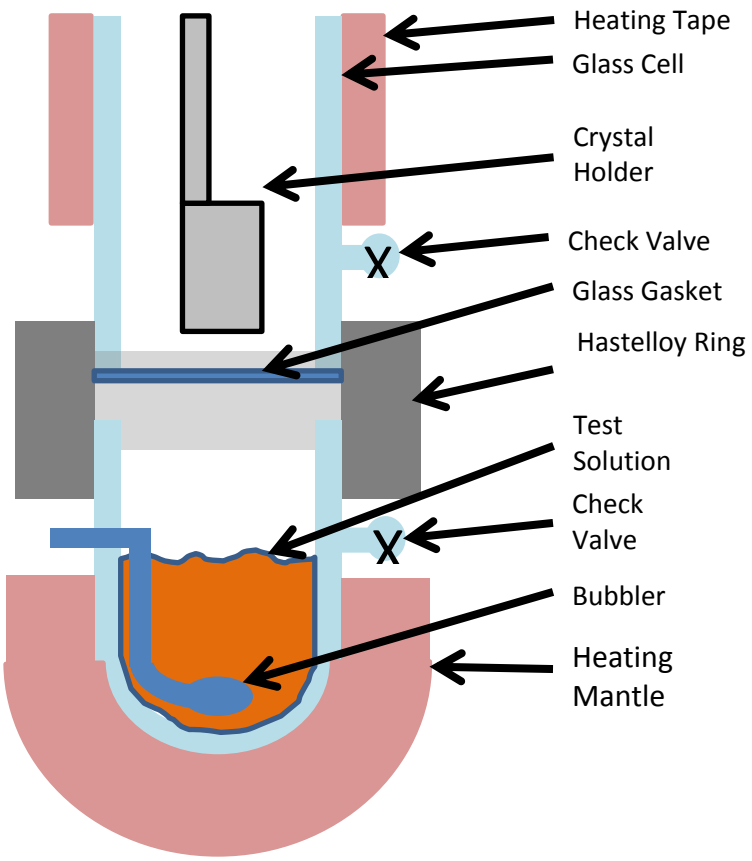


Figure 4. Cross sectional schematic of glass autoclave

Stainless Steel Autoclave

To ensure greater temperature stability, as well as to increase the sample volume and prevent volatilization of the acids, a stainless steel autoclave was designed and fabricated. The stainless steel system was created to allow for testing at temperatures above the flash point of the base oil, and allows for testing at pressures greater than ambient. The autoclave, connectors, and tubing that contacted the oil were all made of 316 stainless steel to minimize corrosion. The autoclave consisted of two chambers, a preheating chamber where the oil is brought up to the testing temperature, and a test chamber where the sample was exposed to the test solution. The two chambers were encased in an aluminum heat sink, which acted to increase the heating rate and minimize hot spots. Six band heaters (Watlow) were used in conjunction with a PID controller (Watlow) and a solid-state relay (Watlow) to control the temperature. Type K thermocouples were positioned in both the preheating and testing chambers to maintain a constant oil temperature throughout the experiments. High temperature oil compatible ball valves (McMaster) were used to control flow between the chambers, and a nitrogen spring was used to move the oil between chambers. To prevent over pressurization during the experiment pressure relief valves (Swagelok) were connected to both autoclave chambers. An Inficon bakeable sensor head was used in the stainless steel autoclave with

a Maxtek RQCM controller. The sensor head was electroplated with platinum using the same method as the glass autoclave sensor head. To seal the sensor head to the autoclave, a Conflat flange (NorCal. Products) with a graphite gasket (McMaster-Carr) was used. Pictures and schematics of the stainless steel autoclave are provided in

Figure 5 -
Figure 8.

For experimentation, 450mL oil samples were degassed in a gas wash bottle (Ace Glass) using house nitrogen at 80°C for at least 4 hours to remove dissolved oxygen. A metal-coated crystal was placed into the sensor head, and the sensor head was sealed to the autoclave using a graphite gasket. After sealing the autoclave, the system was degassed with nitrogen for five minutes at a very high flow rate. A rotary vacuum pump was then used to transfer the oil from the gas wash bottle into the preheating chamber using two valves to the facilitate transfer. After transferring the oil into the preheating chamber, the autoclave was sealed and brought up to the testing temperature. After thermal equilibrium was established, the valve to the test chamber was opened, and oil was pumped from the preheating chamber into the test chamber using nitrogen gas at 35 psi. Once the oil was transferred, the valve was closed and data acquisition began. Aliquots of the test solution were taken throughout the experiment using a needle valve attached to the sensor head. The positive pressure in the test chamber allowed for small samples to be extracted during testing. After data acquisition was completed, nitrogen gas was used to drain the sample chamber, and the autoclave was cooled to room temperature. After cooling to room temperature, the sample was removed and sonicated in hexane.



Figure 5. Assembled front of stainless steel autoclave



Figure 6. Autoclave body without insulation

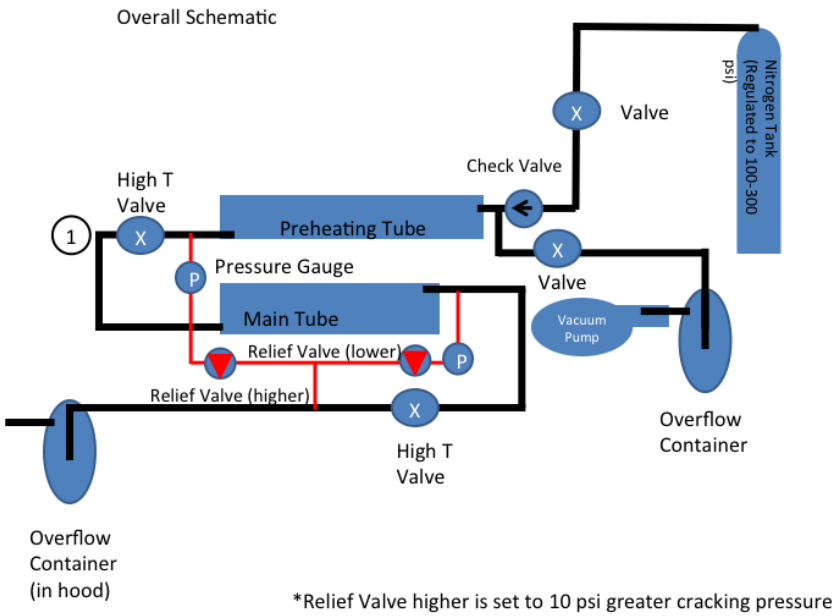


Figure 7. Block diagram of stainless steel autoclave

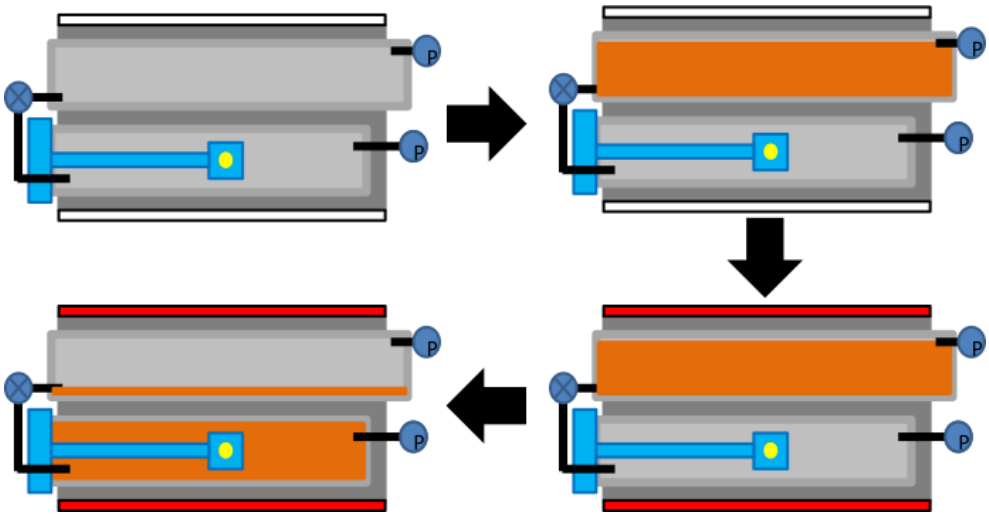


Figure 8. Schematic of stainless steel autoclave operation (Patrick et al. 2015a)

Data Acquisition

All data were acquired at a rate of 300 points/minute, except for tests over 3 hours in duration, which occurred at 60 points/minute. Tuning of the crystal's capacitance was done after 30 seconds of immersion in the test solution, and was done using the RQCM controller. Data recorded included frequency, resistance, oil temperature, and time.

Microgravimetry Sample Preparation

6 MHz gallium orthophosphate crystal resonators with inbuilt gold electrodes were obtain from Piezocryst. The surface area of each electrode was 1.53 cm^2. The resonant frequency of each crystal was measured to be 5.8±0.1 MHz prior to thin-film sample deposition. Before deposition, crystals were sonicated in acetone and isopropanol to remove any surface contaminants. All thin film samples were prepared using vacuum deposition techniques to maximize uniformity and minimize oxidation of the samples. Sputtered samples were deposited using a shadow-mask to hold the crystals in place and control the sample area to 0.87 cm^2. A schematic of a prepared sample can be seen in Figure 9. Chromium, copper, iron, molybdenum, nickel, and silicon were deposited in a Perkins Elmer Randex RF sputtering system and the target purity was greater than 99.9%. The base pressure for all depositions was less than $9x10^{-6}$ torr. Two μm of each material was deposited using tested recipes. The thickness was confirmed via contact profilometry in an Alpha-Step IQ Surface Profile (KLA Tencor). Iron deposition was performed at 175W at 5 mtorr of Ar, with a rate of 17 nm/min. Chromium was deposited at 200W at 5 mtorr of Ar, with a rate of 17.5 nm/min. Molybdenum was deposited at 200W with 2.3mtorr of Ar, with a rate of 30 nm/min. Nickel was deposited at 150W under 4.7 mtorr of Ar, with a rate of 24 nm/min. Silicon was deposited at 100W under 5 mtorr of Ar, with a rate of 10 nm/min. Zinc and gold were deposited via an Edwards electron beam evaporator, and were of greater than 99.9% purity. Two μm of each metal was deposited, which was monitored by an in-situ thin film deposition

monitor. After deposition, the crystallinity and surface structure of the samples was confirmed by X-ray diffraction (XRD) and scanning electron microscopy (SEM) measurements. The XRD measurements were performed using a Bruker D8 XRD analyzer with a copper K_α X-ray source, or a PANanalytical X'pert Pro diffractometer with an X'cellerator detector and a cobalt K_α X-ray source. SEM surface studies were performed in a JEOL Field emission scanning electron microscope at 5kV with a 12 µA beam current using a secondary electron detector unless otherwise noted.

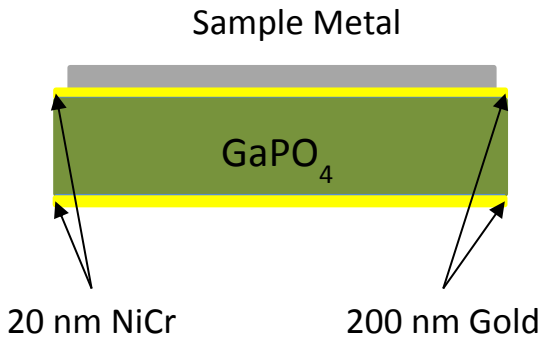


Figure 9 Schematic of microbalance sample prior to experimentation

Mock Crude Oil Preparation

Naphthenic acid was obtained from a commercial source (Sigma-Aldrich) and was of technical purity. RLOP 600N base oil (source: Chevron Energy Technology Company) was used as high purity white oil. Both the Naphthenic acid and Base oil were used as obtained without any further purification. Three weight percent naphthenic acid was prepared in a large batch (approximately five gallons at a time) to ensure consistency of the test solution. Stirring was performed at a high rate for 30 minutes to homogenize the solution prior to experimentation. Experiments were performed in an autoclave as described in the above section.

In-situ Oxide Stripping

Experiments on samples that were stripped in-situ of their surface oxides were performed in a custom-made 316L stainless steel autoclave with a rotating shaft. The shaft was sealed using a PFTE spring-loaded seal (McMaster), and all other seals were made with PFTE O-rings (McMaster). A lift-check valve (Swagelok) and poppet valve (Swagelok) was used to ensure a positive pressure in the autoclave at all times. Four Firerod heaters (Watlow) were used in conjunction with a controller (Watlow) in order to maintain the temperature of the autoclave. ¼" diameter samples of chromium and molybdenum were obtained through ESPI and were of at least 99.9% purity. ½" diameter Alloy 110 copper and Alloy 200 nickel rods were obtained from McMaster-Carr. All metal samples were sequentially ground and polished to a 1 µm finish using metallographic techniques. An ultrafine novaculite grinding stone (Grainger) was used for in-situ grinding. 400 mL samples of 3 and 15 wt. percent naphthenic acid mixtures were used in these experiments. A schematic and pictures of the autoclave are in

Figure 10 -
Figure 12. The oil was degassed in a wash bottle using house nitrogen for at least 24 hours at 80°C in order to remove the maximum amount of oxygen possible.

During experimentation, metal samples were first affixed to a sample holder mounted on the end of a ¼" 316L shaft. The samples were ground to level, and then polished to a 1 µm finish. The shaft was placed in the autoclave and then sealed into the top of the autoclave using a spring loaded PFTE O-ring. The top and bottom portions of the autoclave were sealed with a PFTE O-ring and 4 3/8 in. bolts. The degassed oil was kept heated at 80°C in order to facilitate transfer into the autoclave. The autoclave was then flushed with nitrogen for 5 minutes at a high flow rate and was subsequently heated to 150°C. At 150°C the bolts were re-torqued to ensure a proper seal throughout the experiment. The autoclave was then heated to the testing temperature of 270°C, and then the oil was transferred into the cell using a nitrogen spring. The sample was ground for 2 minutes at 150 rpm and the corrosion reaction proceeded for 4 hours. After the test was completed, the cell was cooled and then the sample was removed, sonicated with hexane, and then imaged in the SEM. Control samples that were used to assess whether corrosion took place utilized the same procedure, except a solution of pure base oil was used to lubricate the grinding stone instead of the naphthenic acid containing solution. FT-IR analysis of the test solution was performed on Thermo Scientific Nicolet iS10 FT-IR spectrometer using attenuated total reflectance (ATR) on diamond crystal. The samples of solution were analyzed as removed from the reaction mixture.

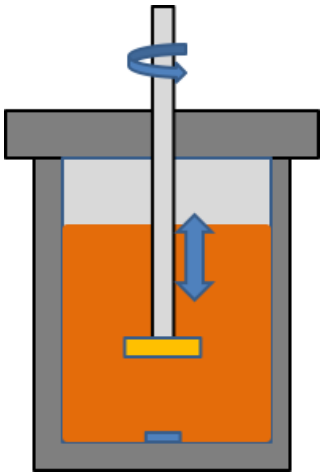


Figure 10. Schematic of Oxide Removal Autoclave.



Figure 11. Nickel sample mounted in top of oxide removal autoclave



Figure 12. Assembled Oxide Removal Autoclave

Total Acid Number

A double junction Ag/AgCl references glass combination pH electrode, as well as pH 4, 7, and 10 buffers were obtained from Fisher Scientific. ACS reagent grade toluene, 2-propanol, ethanol, potassium hydroxide, lithium chloride, and naphthenic acid (technical) were obtained from Sigma Aldrich. All measurements were made following ASTM D664. An outline of the procedure is provided below.

First, a solution of ethanol with 3M lithium chloride was prepared. The reference chamber of the Ag/AgCl reference electrode was drained and rinsed with ethanol 6 times.

The 3M lithium chloride solution was then used to fill the Ag/AgCl reference chamber of the pH electrode. The electrode was then soaked in deionized water for 15 minutes and the potential of the electrode was recorded in pH 4 and pH 7 buffers. The minimum potential difference prior to executing a test was 162 mV. If the electrode potential was less than 162mV, the electrode was treated with 20% ammonium fluoride and 6M hydrochloric acid, followed by soaking in a pH 4 solution overnight. The electrode drift was tested by measuring the potential drift over 1 minute in the titration solvent after stabilizing in pH 4, 7, and 10 solutions. If the electrode drift was more than 3 mV, then the electrode was refreshed using the above method. The titration solution consisted of 0.1M potassium hydroxide in 2-propanol. The solution was created by gently boiling 6 g of potassium hydroxide in 1 L of 2-propanol for 10 minutes. The solution was then covered and allowed to sit for 2 days, then filtered through a sintered glass funnel. The titration solvent was created by mixing 495 mL of 2-propanol with 5 mL of water, and 500 mL of toluene.

During experimentation a burette with 0.05mL resolution was positioned over a 250mL beaker on top of a stir plate. Titration solution was added to the burette, and then a soda-lime carbon dioxide scrubber was positioned on top of the burette. 125 mL of titration solvent was added to the beaker and titration solvent and the electrode was positioned in the solution and allowed to stabilize. The titration was performed by adding 0.05-0.1mL of the KOH solution at a time. The titration continued until the potential of the pH electrode was less than -300mV. The value from the non-acid containing experiment is then taken as TAN value of the titration solvent, and was measured at the beginning of each day of experimentation. After each test, the pH electrode was rinsed in 2-propanol and soaked in water for 15 minutes to re-establish the gel layer. The same procedure was used for measuring the acid number for acid containing oil samples, except a 1mL sample of oil was added to the titration solvent at the beginning of the experiment. The results of the test are plotted as volume of potassium hydroxide added vs. cell potential. The points of inflection for the curve are calculated and then the acid number is calculated using *equation 2*.

$$TAN = (A - B)M\frac{56.1}{W} \qquad \{2\}$$

In the above2, *A* is the volume of potassium hydroxide solution added between the points of inflection for the start and end points of the titration (mL), *B* is the volume of potassium hydroxide required to neutralize the acids present in the titration solvent (mL), *M* is the molarity of the potassium hydroxide solution (M), *W* is the mass of the oil sample (g), and the factor 56.1 is the molar mass of potassium hydroxide. To calculate the TAN, an average value was taken from three separate tests.

Raman Spectroscopy

Cyclohexane acetic acid, naphthenic acid technical solution, and activated carbon adsorbent were purchased from Sigma Aldrich, and metal powders of iron, zinc, and

copper were purchased from Alfa Aesar. All the chemicals were used as obtained. Raman spectra were generated by irradiating samples with 632.8 nm light from a Spectra-Physics Model 127 HeNe laser. The laser light passed through a Corion 632.8 nm plasmaline filter and was directed onto the sample surface by a set of Newport 632.8 nm dielectric mirrors and an Olympus metallurgical microscope (Olympus BH2-UMA). The scattered light was collected and was then directed by another set of dielectric mirrors, passing through a Kaiser Optics (Ann Arbor, MI) Super Holographic SuperNotch Filter to reduce the elastically scattered signal before being directed into a SPEX 275 M spectrometer (Jobin Yvon, Inc., Edison, NJ) having an effective bandwidth of 4 cm−1 and equipped with a 1200 groove/mm diffraction grating. The spectrometer was controlled by SPEX DM3000S software running on a generic 486 DOS PC. The intensity of the dispersed light was measured with a nitrogen-cooled Spectrum One Charge Coupled Device (CCD) detection system. The high temperature micro-Raman stage (FT-IR-THS 600) was procured from Linkam Scientifics, U.K. FT-IR analysis was performed on Thermo Scientific Nicolet iS10 FTIR spectrometer using attenuated total reflectance (ATR) on diamond crystal. Samples were studied as isolated from the reaction mixture.

Bright yellow naphthenic acid technical solution (Sigma-Aldrich) was found to fluoresce heavily, while being subjected to Raman spectral measurements using 632.8 nm line of He−Ne laser. Therefore, it was initially processed by using the procedure reported by Brown et al.(Ahmadjian & Brown 1976; Sunder et al. 1976) Naphthenic acid technical solution (2 mL) was diluted with 25 mL of n-hexane, and the resulting mixture was filtered through 4 g of activated carbon. It is believed that the minute amounts of the bulky aromatic molecules acting as a fluorescence source were largely removed from the sample by being entangled in the pore spaces of the activated carbon. Any residual activated carbon remaining in the hexane extract was removed by filtering the solution through Whatman filter paper (P8). The solvent was subsequently evaporated at room temperature to yield a very pale yellowish naphthenic acid sample, which was then used in all the naphthenic acid mineral oil mixtures (v/v) made during the course of the spectroscopy portion of the work. All mixture and neat samples were degassed overnight under nitrogen atmosphere by bubbling nitrogen gas overnight through them at 40 °C. The samples were then transferred under nitrogen atmosphere to the heating cell used for spectral measurements. For high temperature studies, all the samples were heated in a quartz crucible in the cell under nitrogen atmosphere at the rate of 10 °C/min, and held at a specific temperature reported later for 10 min before measuring the spectrum. All percentage mixtures of naphthenic acid in oil are in volume/volume (v/v) ratio.

Solution Conductivity

Several ionic liquids were obtained from commercial suppliers. Trihexyltetradecylphosphonium based ionic liquids with the anions chloride ($P_{6,6,14}$ [Cl]), bromide ($P_{6,6,14}$ [Br]), *bis*(2,4,4trimethylpentyl)phosphinate ($P_{6,6,14}$[BIS]), decanoate ($P_{6,6,14}$ [DCN]), and dodecylbenzenesulfonate ($P_{6,6,14}$Do[DBS]) were obtained from Cytec. 99.9% Tetrabutylammonium perchlorate ([TBAP]) and anhydrous 99.9% 1-methyl-3-butyl imidazolium tetrafluoroboate ([bmim][TFB]) was obtained from Sigma Aldrich and were used as received. Toluene was obtained from Sigma Aldrich, and was

dried by distillation over calcium hydride. 0.4M or saturated solution of each of the ionic liquids was used for testing.

Trihexyltetradecylphosphonium tetrakispenta(fluorophenyl)borate ($P_{6,6,14}$[TKIS]) was created in house by mixing equal molar proportions of trihexyltetradecylphosphonium chloride with potassium tetrakispenta(fluorophenyl)borate (Boulder Scientific) in an excess of acetone (Sigma-Aldrich), and stirring vigorously for 48 hours at room temperature. After 48 hours, the solution was filtered with filter paper (P8, Fisher Scientific). After filtering, the solvent was removed with a rotary evaporator, and subsequently dried in a vacuum oven at 75°C for 24 hours. Structure measurements were performed in an AVQ-400 spectrometer via ^{19}F NMR.

Conductivity measurements were performed in a custom made quartz and glass cell (Adams and Chittendon Scientific Glass). The test cell is shown in Figure 13. Platinum wire was sealed into glass, which was fused into quartz, creating quartz-insulated electrodes. For four-point probe measurements of conductivity, electrodes were sealed into a glass plate, using a high resistance epoxy, in an equally spaced linear configuration with a spacing of 0.628 cm. Electrodes were connected to electrical contacts using an electrically conducting epoxy (Cotronics Corp.). The electrode assembly was then ground flat using a grinding wheel. Samples were placed within a quartz dish inside and the electrode assembly was placed on top of the dish such that the electrodes were flush with the surface of the liquid. A high voltage power source (Hypot II) was connected to the outer electrodes in series with a picoammeter for making measurements. A current limiting resistor was used with high resistance solutions to prevent damage to the equipment in the case of an electrical arc. A high voltage voltmeter (Pintek) was placed across the inner electrodes for measuring the voltage drop in solutions with a resistivity less than 10^6 Ω-m. A potential was applied across the outer electrodes, and the corresponding current was recorded after steady state value was obtained (1-5 minutes). The corresponding voltage drop across the voltmeter was recorded also. For extremely high resistivity solutions (>10^6 Ω-m) a two-point probe configuration was used due to the limited input impedance of the voltmeter. For these tests, the voltmeter was removed from the inner electrodes, and the potential and current across the outer electrodes were recorded.

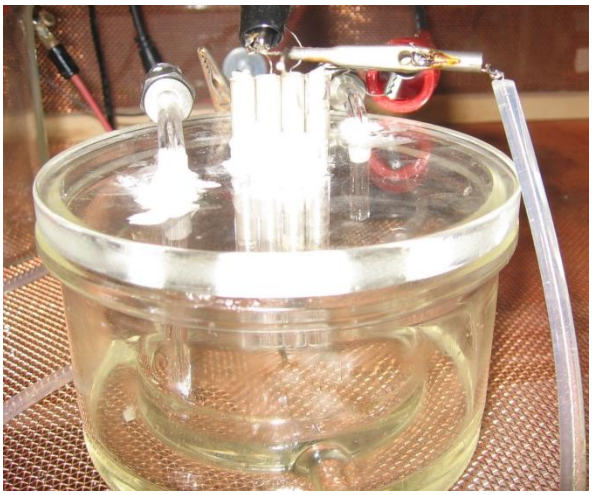


Figure 13. Four point probe inside of Faraday cage

Electrochemical impedance spectroscopy (EIS) was also used to measure the resistivity of solutions. EIS experiments were performed in a custom made PFTE cell with a confined circular geometry. ¼" nickel rods were used as the working and counter electrodes. The cell was filled with solution from a filling port on the top with approximately 1 mL of solution. The EIS measurements were performed at open circuit with a frequency range of 60kHz to 0.1 Hz. The solution resistivity was calculated using the impedance at a frequency of ~10kHz, ensuring that the phase angle at the selected frequency was as close to 0° as possible.

Palladium Hydride Reference Electrode

Electrodes

0.003 in (76 µm) thick 99.99% palladium foil and 0.003 in (76 µm) diameter 99.999% palladium wire were obtained from ESPI Metals, USA. The foil was cut into a 2.54x2.54 cm square (12.9032 cm^2 surface area) and mechanically polished by using 6 µm, 3 µm, 1 µm, and 0.3 µm diamond suspensions sequentially. Mechanical polishing was repeated periodically during experimentation to refresh the electrode's surface. A 5 cm length of the palladium wire was tack welded to the foil in order to electrically connect the foil to electronic instrumentation. Prior to each set of experiments, the electrode was cleaned by dipping it in concentrated sulfuric acid, followed by rinsing it in doubly deionized water, then acetone, and finally hexane. Square platinum counter electrodes measuring 2.54x2.54 cm were prepared from 0.002" thick platinum foil and 0.003 in. (76 µm) diameter 99.999% platinum wire. The platinum counter electrodes were prepared following the same procedure as used for the large palladium electrode.

Palladium-palladium hydride (PdH) electrodes were prepared by immersing Pd electrodes in solutions saturated with forming gas. Foils of PdH served as combination counter electrodes and reference electrodes (CE/RE) in electrochemical tests in which the working electrode (WE) was an ultramicroelectrode (UME) of either platinum (10 µm diameter disk) or PdH (76 µm diameter disk). The PdH isotherms measured as a function

of temperature indicate that the PdH electrodes, which were formed by immersed of Pd in solutions saturated with forming gas, consist of an outer layer of β-PdH.(Flanagan and Oates 1991) As the absorption of hydrogen is a kinetically limited process, thickness of the β-PdH layer depends on the time of immersion in the solution. In most cases the electrodes were prepared by immersion for 15 minutes. Assuming that hydride formation is controlled by the diffusion of hydrogen in β-PdH, the thickness of the β-PdH layer is approximately 60 μm.(Flanagan & Oates 1991a)

Selected electrochemical tests were conducted with PdH CE/RE created from palladized palladium foil. The results were similar to tests with palladium foil. Deposition of palladium black was accomplished in an aqueous solution of dilute palladium chloride in 0.1M hydrochloric acid and a cathodic current density of 50 mA/dm^2.

A 10 μm diameter platinum UME was obtained from C-H Instruments. Palladium ultramicroelectrodes were produced by first sealing 0.003 in (76 μm) diameter palladium wire into a soft glass capillary. The end of the tube in which the Pd wire was sealed was then mechanically ground and then polished using 6 μm, 3 μm, 1 μm, and 0.3 μm diamond suspensions. The polished, circular, 0.003 in (76 μm) diameter end-face of the wire served as a palladium UME. Prior to each test, the UME was polished using a 0.3 micron diamond suspension.

Solutions

Anhydrous dichloromethane (DCM), ferrocene (Fc), decamethylferrocene (dmFc), anthraquinone (AQ), and 1-methyl-3-butyl imidazolium tetrafluoroborate [bmim][TFB], anhydrous acetone, and n-hexane were obtained from Sigma-Aldrich and used without further purification. All solvents were stored over 4A molecular sieves in a glove box filled with forming gas. All experiments, unless noted, were performed in a VAC glove box under an atmosphere of forming gas (96% N_2, 4% H_2). The glove box atmosphere was periodically refreshed to ensure a dry, oxygen free environment. Test solutions were deoxygenated by vigorous bubbling for 30 minutes with forming gas inside the glove box prior to each experiment. Experiments in dichloromethane were conducted using 0.2M [bmim][TFB] as a supporting electrolyte, and the solution resistivity was approximately $7.8x10^2$ Ω-cm.(Hunger et al. 2008) The electrochemical window for [bmim][TFB] is approximately 4V, and was stable at potentials used during experimentation. For experiments on AQ with water added, a very small amount of water was introduced to the dried dichloromethane. The addition of water did not introduce any anomalous peaks in the voltammograms.

Electrochemical Tests

Briefly stated, the objective of the electrochemical tests was to determine the suitability of PdH as a reference electrode. Five tests were conducted. (1) Estimates of the electrochemical potential of PdH in DCM containing 0.2M [bmim][TFB] were obtained by measuring the half-wave potentials of AQ, Fc and dmFc in a two-electrode

cell consisting of a platinum UME and a PdH CE/RE. (2) The stability of the PdH electrode was evaluated by measuring its potential vs. a calomel electrode in 0.1M TBAP in acetonitrile (ACN). The reversibility of the PdH electrode in DCM with 0.2M [bmim][TFB] was investigated by (3) small amplitude (±0.010V) cyclic polarization experiments and (4) large amplitude (±0.5V) square-wave polarization tests with step widths of 5s, 50s and 500s. Both types of reversibility experiments (i.e., (3) and (4)) were carried out in a two-electrode cell in which an UME of PdH was the WE and a large PdH foil served as a CE/RE. Nernstian behavior of PdH immersed in aprotic solutions was evaluated by (5) measuring changes in the potential of PdH due to changes in partial pressure of hydrogen gas (two values of partial pressure were investigated: ≈0.04 atm and ≈1.0 atm of H_2. Details are provided at the end of the present subsection). All electrochemical experiments were carried out with a Gamry PCI4-750 potentiostat.

All experiments performed in DCM with 0.2M [bmim][TFB] were conducted with a 2 electrode cell consisting of a working electrode (WE) with very small surface area (UME) and a large counter/reference electrode (CE/RE). That is, the second electrode served as a combination counter and reference electrode (CE/RE). Because the ratio of the areas of the UME and the counter/reference electrode was so small (i.e., $7x10^{-6}$) the current density flowing through the counter/reference electrode is insignificant, and does not polarize the reference electrode's potential.

Tests in aqueous 0.1M HCl were performed in a custom glass electrochemical cell in a three-electrode configuration, using an Accumet SCE reference electrode and a large Pt foil counter electrode.

The stability of the potential of PdH was tested by measurements of the potential of a PdH UME vs. the potential of a calomel reference electrode as a function of time. The test was conducted in 0.1M TBAP in acetonitrile (ACN), which was selected because its chemistry was compatible with the calomel electrode and the PdH electrode. The calomel electrode was formed by replacing the aqueous KCl electrolyte of a conventional SCE with lithium chloride saturated acetonitrile. It should be noted that while the SCE is not normally used in acetonitrile containing solutions, its potential with respect to an aqueous silver chloride reference electrode was determined to be the same before and after experimentation.

Experiments to determine the Nernstian behavior of PdH in different aprotic solvents were conducted by measuring the change in open circuit potential of the PdH vs. a known reference in several solutions associated with changing of the partial pressure of hydrogen. A custom made two-electrode cell was used, consisting of a large PdH working electrode and an aqueous SCE. The solvents chosen were acetonitrile, dimethylsulfoxide, dimethylformamide, and dichloromethane; each solvent was of reagent grade (Sigma-Aldrich). The supporting electrolyte was 0.2M [bmim][TFB] in each of the solvents. The solutions were bubbled vigorously with forming gas until a stable potential was reached, and then subsequently bubbled with 1 atm of H_2 until a stable potential was reached. The half potential shift of dmFc was also measured in

DCM after saturating with forming gas and H_2 to ensure the potential of the SCE remained constant throughout the experiment.

Safety regulations imposed on the Hearst Mining Building in which our laboratory is located prohibit canisters of pressurized gas with more than 4% hydrogen. A partial pressure of $H_{2(g)}$ of 1 atm was established in solutions of 0.2M (bmim][TFB] in various solvents by on demand hydrogen generation using the ferrosilicon process.(Weaver 1920) A 316 stainless steel pressure cooker with emergency pressure relief was used as a reaction vessel. Silicon powder and sodium hydroxide were obtained by Fisher Scientific and were used as received. Approximately 200mL of concentrated (20 wt. %) aqueous sodium hydroxide solution was combined with a small amount of silicon powder (~3g) in the reactor at room temperature, and the vessel was purged with nitrogen and subsequently sealted. A hot plate was used to bring the reagents to 50°C. After reaching the temperature the hot plate was turned off, and the silicon reacted with the sodium hydroxide to produce hydrogen gas and sodium silicate. Large double layered thick latex balloons were used to store the generated hydrogen, so that a constant hydrogen flow could be supplied to the dichloromethane solution. A liquid nitrogen cold trap was used to remove all humidity from the hydrogen before entering the electrochemical cell. Hydrogen gas flow was controlled with a flow meter (Cole Parmer) to ensure a constant flow rate for forming gas as well as hydrogen.

Supporting Electrolyte Selection via Voltammetry

Reagent Plus grade benzyl benzoate was obtained from Sigma Aldrich. 0.4M solutions of each of the ionic liquids employed in the conductivity measurements were prepared in benzyl benzoate. Electrochemical measurements were performed using a Gamry PCI4-750. The ionic liquid stability tests were performed using a 10 µm platinum UME (CH Instruments) and 1 in. x 1 in. foil palladium hydride counter/reference electrode. Tests were performed using the same solution preparation methods and equipment as the forming gas saturated palladium hydride tests. Scans were performed over a large voltage range (up to ±6V vs. PdH) and utilized a scan rate of 250 mV/s. A series of three scans were conducted. Scanning began at 0Vvs. PdH and the electrode was initially polarized in the positive direction. After initial determination of the stability limits, additional testing was done using a smaller potential range to confirm the stability limits for each ionic liquid. The third scan was used for analysis. The purpose of these experiments was to find the stability limits of the ionic liquid, which was determined by a 1.5 nA increase in current over background.

Single Acid Voltammetry

Benzoic, cyclohexane acetic, cyclohexane butyric, dodecanoic, and stearic acids, along with calcium hydride, and toluene were obtained from Sigma Aldrich and were of reagent grade purity. 4A molecular sieves were obtained from Sigma Aldrich. Toluene was dried using the standard practice of distillation over calcium hydride, and was stored

over molecular sieves. All chemicals were stored in a glove box filled with forming gas (96% N2, 4%H2).

10 mM solutions of each of the acids in toluene were prepared using toluene dried using the above method. Palladium electrodes were prepared as described in the subsection entitled “Electrodes”. Pt UMEs were polished with 0.1µm diamond paste after each experiment. Experiments were performed in a two-electrode configuration inside of a forming gas glove box. 10mL of a 0.4M solution of $P_{6,6,14}$[TKIS] in toluene was prepared in the glove box and the Pt UME and palladium counter/reference electrode were positioned in the solution. Solution was then degassed with forming gas for 15 minutes at a high flow rate. Initially, three successive cyclic voltammograms were performed using a voltage range of 0 V vs. PdH to -2V vs. PdH, and a sweep rate of 25 mV/s. The objective of the three scans was to confirm the absence of peaks within the potential range of 0V to -2V vs PdH. After confirmation, 0.5 mL of the 10mM solution of an acid was added and the solution was degassed for 5 minutes. Voltammetry experiments containing single acids were performed using the same conditions as for the acid-free solutions.

Results

Introduction to Experimental Results

The results section will present a large amount of data from multiple thrusts to understand different aspects naphthenic acid corrosion. Data will be presented from experiments to understand the coordination of naphthenic acids in solution and to determine mechanism of naphthenic acid corrosion on refinery materials. In addition, results will be presented from electrochemical experiments to develop a technique for determining the corrosivity of a crude. It is important to note that while the experiments while seem unrelated, they are all purposed towards understanding and recognizing naphthenic acid corrosion and their relationship will be expounded upon in the Discussion section.

Characterization and Structure of Naphthenic Acids

This section will present the results for all of the experiments that were performed to understand the current testing performed in industry, as well as the structure of naphthenic acids in the bulk of solution. In order to understand the complex system of naphthenic acid – mineral oil mixtures, several different techniques were used. First, experiments were performed to allow comparison of in-house measurements to those in the literature using TAN measurements. In addition to these measurements, Raman and FT-IR spectroscopy were employed to understand how the structure and coordination of the naphthenic acids change as a function of temperature, concentration, and presence of metals. The Raman and FT-IR experiments aimed to answer the question of why naphthenic acid corrosion begins at approximately 200°C, and of what is the impact of acid concentration as well as presence of a metal susceptible to corrosion.

Total Acid Number

As an initial effort to characterize the test solutions used as well as to understand the current state of the art, TAN measurements were made following ASTM D664. As mentioned earlier, TAN measures the amount of potassium hydroxide (KOH) that is required to neutralize all of the acids present inside of a sample of an oil. Ideally, TAN measures only the corrosive carboxylic acids in a crude, however it is suspected that the KOH also reacts with other species in crude. (Dettman et al. 2009) The titration reaction between the naphthenic acid and the titrant can be described as an exchange between the potassium ion and the proton in the acid. The products from the acid/base reaction are potassium naphthenate, and water. As the potassium naphthenate is a singly charge naphthenate, one acid molecule consumes one potassium hydroxide molecule. To compare the reaction between naphthenic acid and potassium to that of naphthenic acid and iron, which forms a doubly charged ion, two naphthenate ligands are required for iron, while one is required for potassium. Thus, to directly compare TAN to corrosion results neglecting kinetics, it is expected that one half of the amount of iron would be corroded compared to potassium. TAN measurements performed in this work were

compared with measurements performed by Chevron Co. to ensure the compatibility of measurements made between different systems.

An example of a TAN measurement for the three-weight percent NA test solution is shown Figure 14. A table of TAN values or multiple concentrations of naphthenic acid in several different types of mineral oils is shown in
Table 1. The results show a linear relationship between acid concentration and TAN.

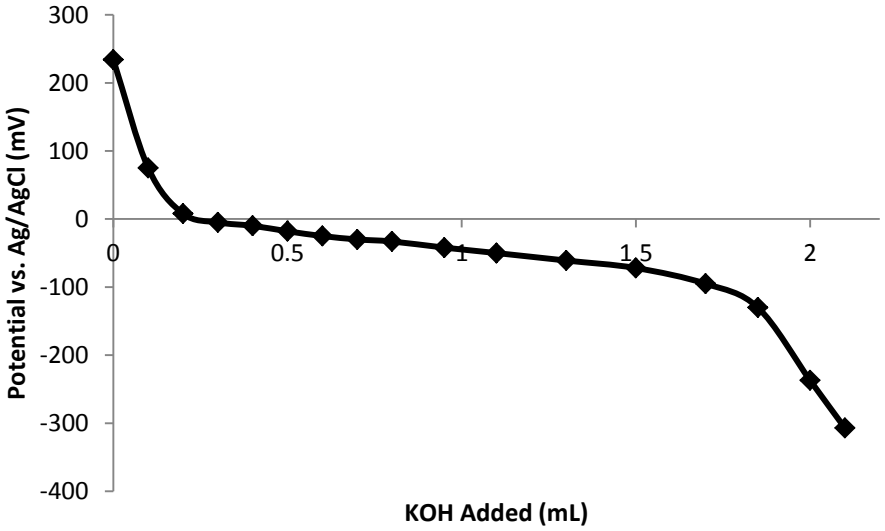


Figure 14. Example potentiometric titration of test solution (3 wt. percent naphthenic acid in RLOIP 600)

Solution	A	B	W	TAN 1	TAN 2
MO+10v/o NA	6	0.25	1	32.25	25.22
Heavy MO + 10 v/o NA	5.4	0.25	1	30.00	28.28
Light MO + 10 v/o NA	4.7	0.25	1	24.90	24.92
MO + 1 v/o NA	2.75	0.2	5.07	2.81	2.51
Heavy MO + 1 v/o NA	2.6	0.2	5.18	2.59	2.97
Light MO + 1 v/o NA	3.8	0.2	5.07	3.97	4.36
MO + 0.1 v/o NA	1.27	0.2	16.9	0.35	0.37
Heavy MO + 0.1 v/o NA	1.45	0.2	17.6	0.39	0.41
Light MO + 0.1 v/o NA	1.35	0.2	16.9	0.38	0.28

Table 1. TAN values for several naphthenic acid mineral oil combinations. A is the amount of KOH solution needed to titrate between inflection points (mL) for the first sample, W is the mass of sample added (g) for the first sample, and TAN 1 and TAN 2 are the calculated total acid numbers for two samples. MO = Mineral Oil

After ensuring viability of my methods, several TAN measurements were made of a mock high TAN crude oil, which was used for these tests. The solutions were made to be three weight percent in high purity base oil (RLOP 600). The results from the in house measurements yielded a TAN value of approximately 9, which was comparable to values obtained by Chevron ETC. on the same solution.

Raman Vibrational Spectroscopy to Determine Acid Structure

Raman and FR-IR spectroscopy was used to understand the chemical structure of the naphthenic acids and their coordination with metal ligands during the corrosion process. As mentioned earlier, the spectroscopic experiments aimed to look at the effect of temperature, concentration, and metals on the coordination of acids in oil solutions. To study the conformation of naphthenic acids in solution the Raman shift of the C=O stretch in the carboxylic acid was studied in the range of 1650-1730 cm^{-1}. The Raman shift of the C=O stretch changes as a function of hydrogen bonding of the acid, as will be expounded upon in the discussion section.

Structure of Single Acids as a Function of Temperature and Concentration

As a first step to understand the behavior of the mixture of naphthenic acids present in crude, single naphthenic acid structures were first studied. The behavior of the very simple carboxylic acid, *n*-propionic acid, was initially observed as a function of temperature using Raman spectroscopy. The raw spectra and peak deconvolutions are shown Figure 15 and Figure 16 respectively, and the peak deconvolution results are presented numerically Table 2. The same procedure was also performed on two single ringed naphthenic acids; cyclohexaneacetic acid and cyclohexane butyric acid, with the results presented in Figure 17-Figure 18 and Figure 19-Figure 20 respectively.

Figure 21 and

Table 3 present the change in ratio of cyclic to linear dimer structures as a function of temperature for cyclohexanebutyric acid.

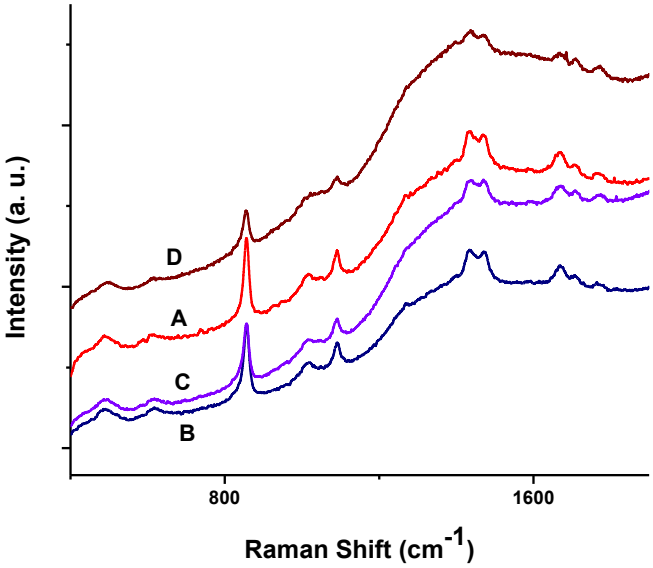


Figure 15. Raw Raman spectra showing the gradual change of the relative concentration of monomer and multimer in propionic acid: (A) Room Temperature (B) 40°C (C) 60°C (D) 80°C. (Chakravarti et al. 2013) Reprinted with permission from Energy and Fuels. Copyright 2013 American Chemical Society

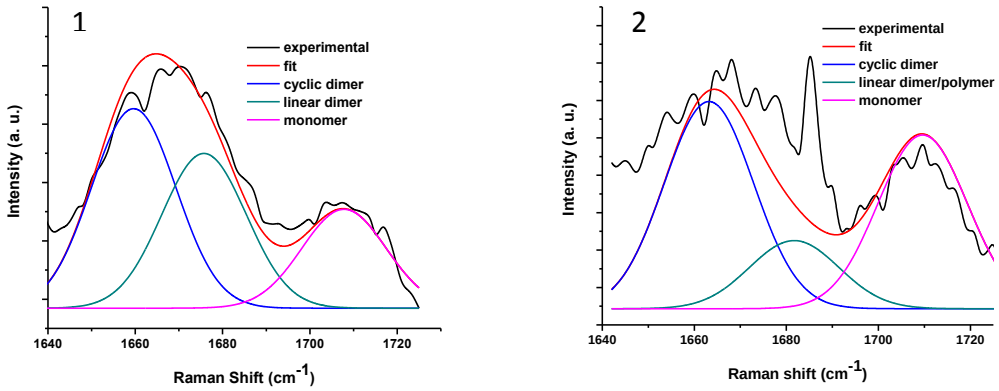


Figure 16. Band-resolved Raman spectrum of propionic acid (1) at room temperature (2) at 80^0C. (Chakravarti et al. 2013) Reprinted with permission from Energy and Fuels. Copyright 2013 American Chemical Society

Species	Room temperature	80^0C
Cyclic dimer	67.06	55.97
Linear multimer	14.63	15.02

Monomer	18.3	29.01

Table 2. Relative concentrations of the molecular species of propanoic acid at various species at different temperatures. (Chakravarti et al. 2013) Reprinted with permission from Energy and Fuels. Copyright 2013 American Chemical Society

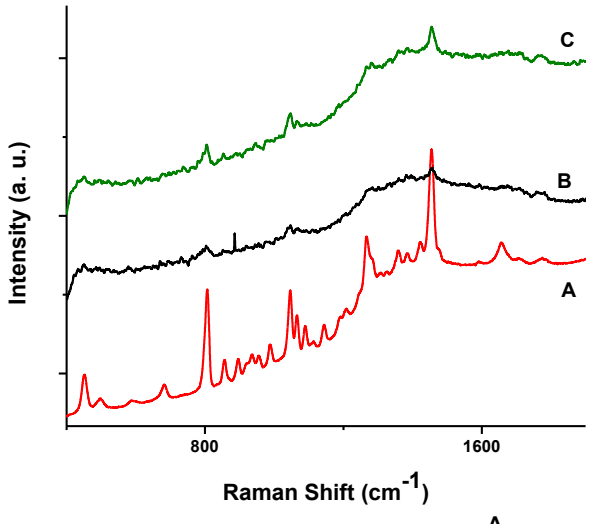


Figure 17. Raman spectra showing the gradual change of the relative concentration of monomer and multimer in cyclohexane acetic acid. (A) Room temperature (B) 100°C (C) 150°C. (Chakravarti et al. 2013) Reprinted with permission from Energy and Fuels. Copyright 2013 American Chemical Society

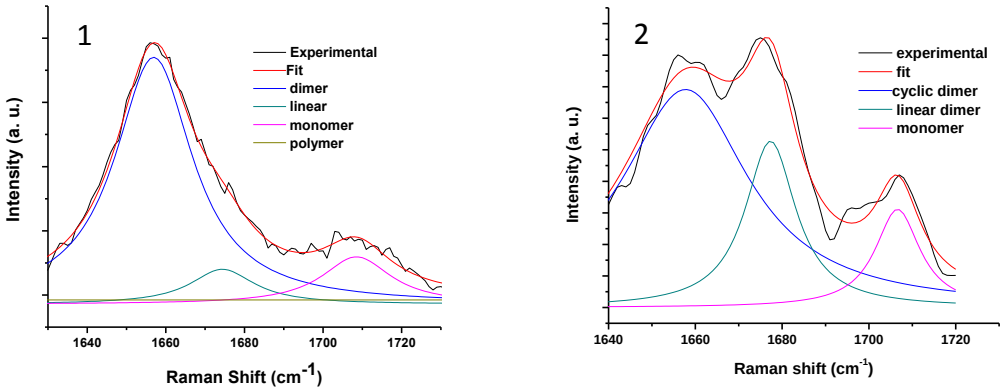


Figure 18. Band-resolved Raman spectrum of cyclohexane acetic acid at room temperature (1) and 150^{0}C (2). (Chakravarti et al. 2013) Reprinted with permission from Energy and Fuels. Copyright 2013 American Chemical Society

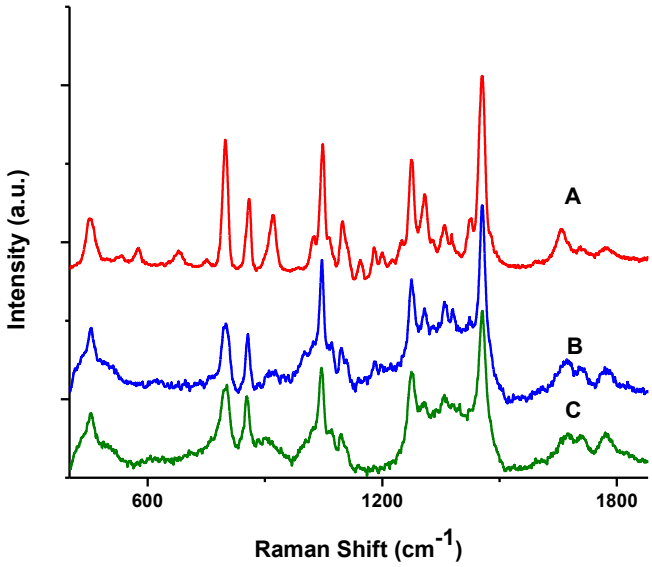
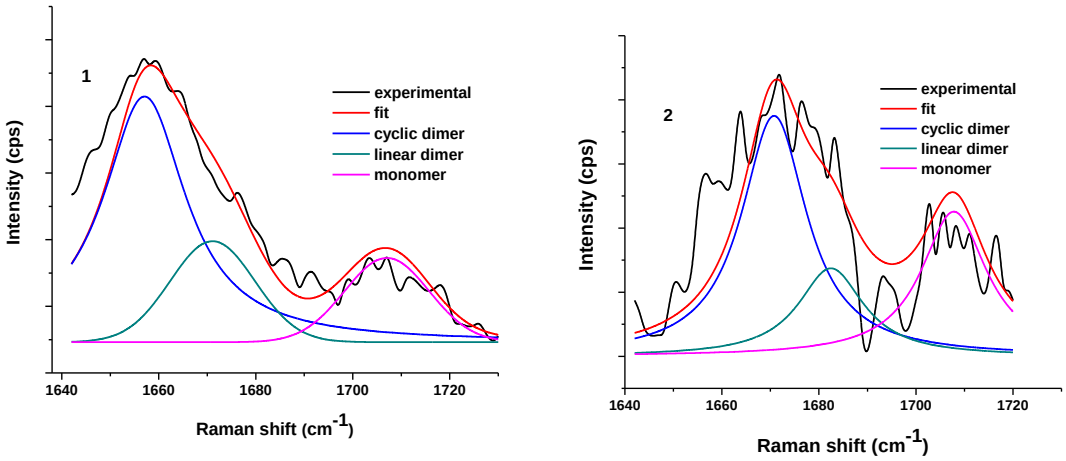


Figure 19. Raw Raman spectra of neat cyclohexane butyric acid with increasing temperature, where the gradual change of the relative concentration of monomer and multimer are not apparent due to overlapping peaks (A) Room temperature (B) 100°C (C) 150°C. (Chakravarti et al. 2013) Reprinted with permission from Energy and Fuels. Copyright 2013 American Chemical Society



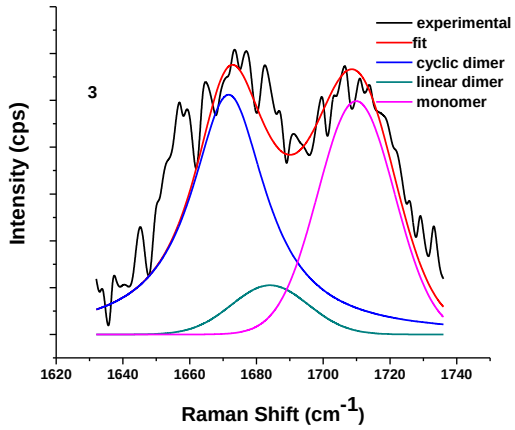


Figure 20. Band-resolved spectrum of cyclohexane butyric acid (1) at room temperature (2) at 100^{0}C (3) at 150^{0}C. (Chakravarti et al. 2013) Reprinted with permission from Energy and Fuels. Copyright 2013 American Chemical Society

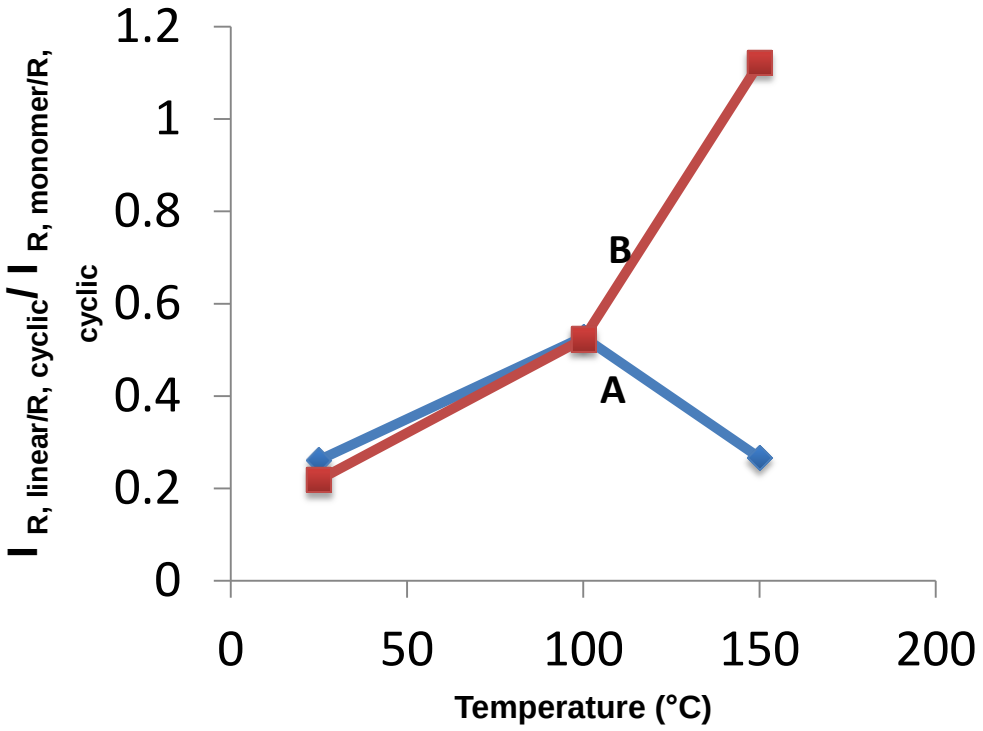


Figure 21. Plot of the ratios (A) Ratio of linear dimer/cyclic dimer (B) Ratio of monomer/cyclic dimer of the cyclohexanebutyric acid as a function of temperature. (Chakravarti et al. 2013) Reprinted with permission from Energy and Fuels. Copyright 2013 American Chemical Society

Species	Room temperature	100°C	150°C
Cyclic dimer	67.58	48.74	41.87
Linear dimer	17.65	25.74	11.15
Monomer	14.77	25.51	46.97

Table 3. Relative concentrations of the molecular species of cyclohexane butyric acid at various temperatures. (Chakravarti et al. 2013) Reprinted with permission from Energy and Fuels. Copyright 2013 American Chemical Society

Structure of Naphthenic Acid Mixtures as a Function of Temperature and Concentration

After performing initial experimentation on single naphthenic acids, the same procedure was applied on a mixture of naphthenic acids, such as what is found in a crude. These Raman experiments were performed to more closely represent a crude, and Raman spectra and peak deconvolution are presented in Figure 22 and Figure 23. The change in the ratio of cyclic to linear dimer as a function of temperature for a naphthenic acid mixture is shown in Figure 24 and
Table 4. For the naphthenic acid mixture, the effect of dilution on the structure of the acids in the bulk of the solution was studied over the range of 20-80% naphthenic acid by volume in a high purity base oil. The peak deconvulution results as a function of dilution are shown in
Figure 25. Finally, the effect of temperature on the acid structure a 20% naphthenic acid solution in base oil was studied, and the results are presented in Figure 26 and Table 5.

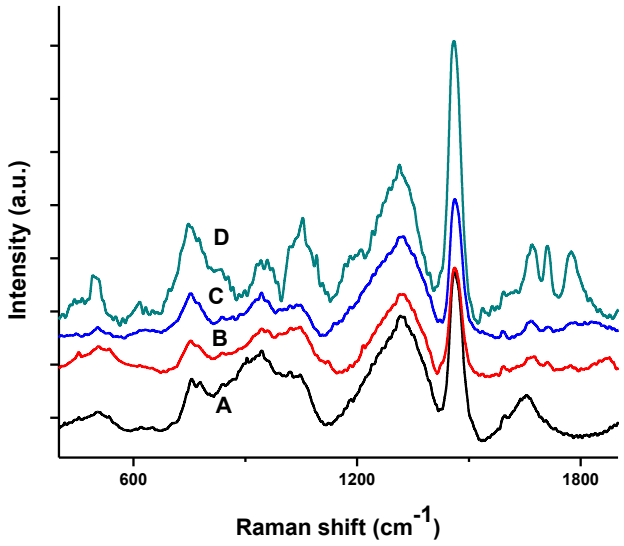
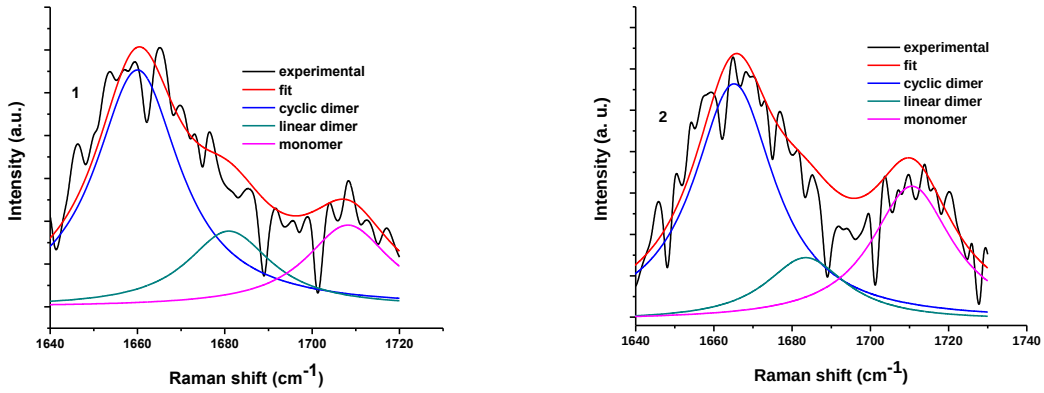


Figure 22. Full spectra of naphthenic acid mixtures showing the variation of the C=O peak with temperature (A) Room temperature (B) 100°C (C) 150°C (D) 185°C. (Chakravarti et al. 2013) Reprinted with permission from Energy and Fuels. Copyright 2013 American Chemical Society



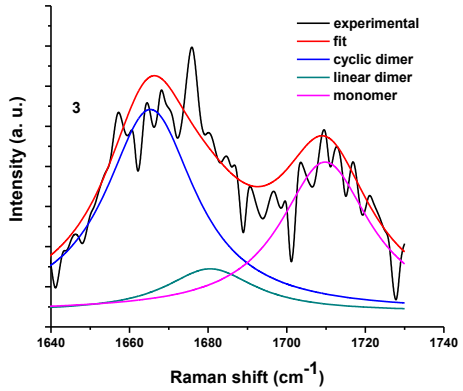


Figure 23. Band-resolved spectrum of naphthenic acid mixtures showing a gradual increase in monomer concentration as a function of temperature: (1) Room temperature (2) 100°C (3) 150°C (4) 185°C. (Chakravarti et al. 2013) Reprinted with permission from Energy and Fuels. Copyright 2013 American Chemical Society

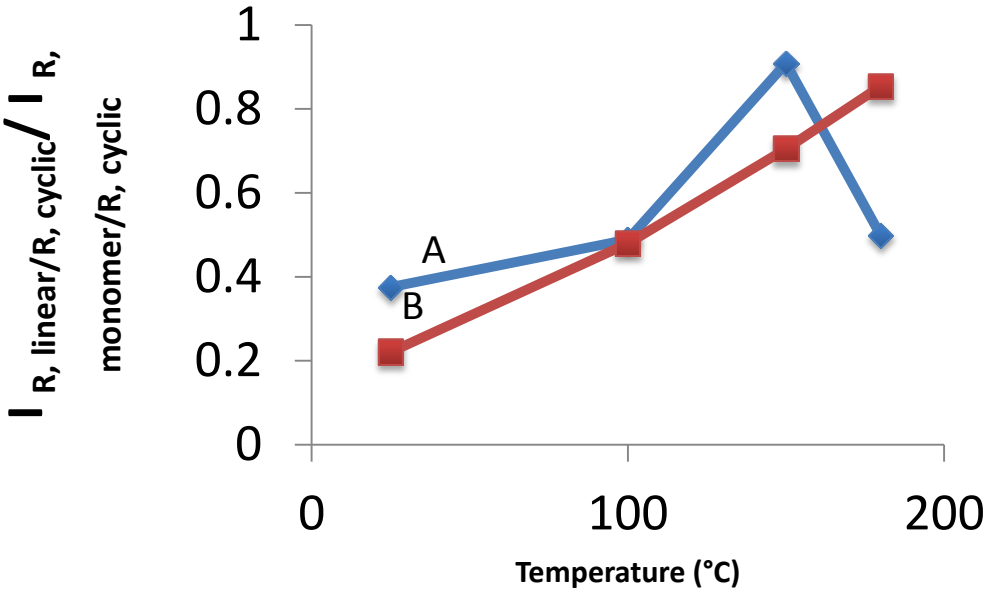


Figure 24. Plot of the ratios of the molecular species as a function of temperature. (A) Ratio of linear dimer/ cyclic dimer (B) Ratio of monomer/cyclic dimer of the molecular species as a function of temperature. (Chakravarti et al. 2013) Reprinted with permission from Energy and Fuels. Copyright 2013 American Chemical Society

Species	Room Temperature	100^{0}C	150^{0}C	180^{0}C
Cyclic dimer	62.65	50.8	38.26	42.51

Linear multimer	23.51	24.83	34.77	21.17
Monomer	13.83	24.36	26.96	36.32

Table 4. Relative concentrations of the molecular species in naphthenic acid mixtures at various temperatures. (Chakravarti et al. 2013) Reprinted with permission from Energy and Fuels. Copyright 2013 American Chemical Society

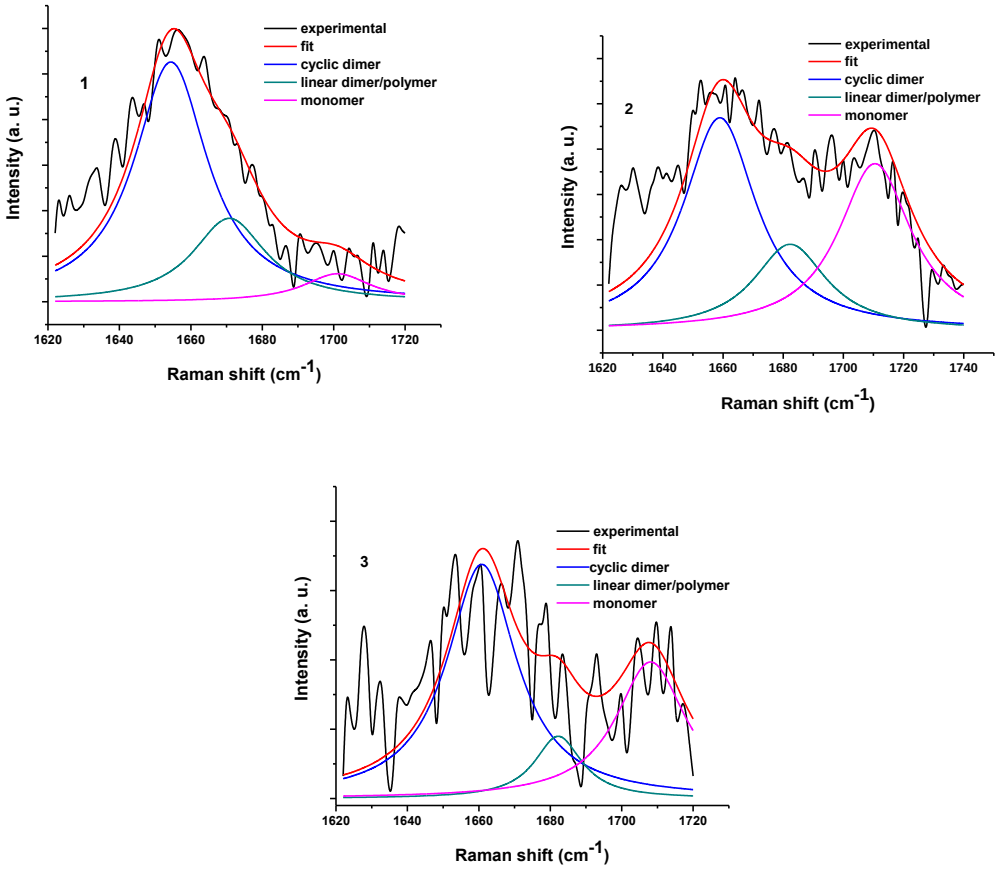


Figure 25. Band-resolved spectrum of naphthenic acid-mineral oil mixtures at room temperature, with (1) 80% naphthenic acid, (2) 50% naphthenic acid, and (3) 20% naphthenic acid. (Chakravarti et al. 2013) Reprinted with permission from Energy and Fuels. Copyright 2013 American Chemical Society

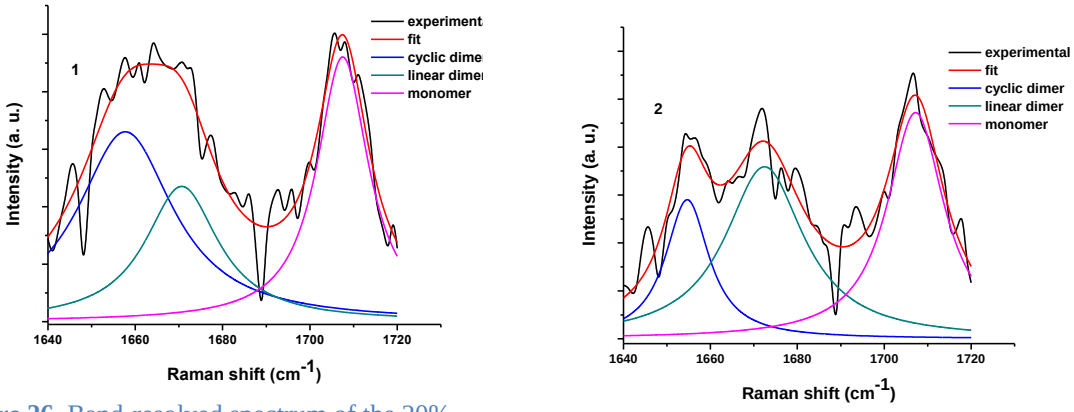


Figure 26. Band-resolved spectrum of the 20% naphthenic acid mixtures at (1) Room temperature and (2) 180°C. (Chakravarti et al. 2013) Reprinted with permission from Energy and Fuels. Copyright 2013 American Chemical Society

Species	Room Temperature	180°C
Cyclic dimer	41	19
Linear multimer	25	42
Monomer	33	38

Table 5. Relative concentrations of the molecular species of naphthenic acid in a 20% naphthenic acid binary mixture at different temperatures. (Chakravarti et al. 2013) Reprinted with permission from Energy and Fuels. Copyright 2013 American Chemical Society

Structure of Naphthenic Acid Mixtures in the Presence of Metals

To represent the situation in which corrosion occurs, experiments were performed at temperature using naphthenic acid mixtures in the presence of a metal. Several metals were selected in order to understand whether the identity of the metal would affect the ligand coordination. The metals selected were iron, zinc, and copper. An experiment showing the effect of time on the structure of acids in the presence of iron at 200°C is shown in

Figure 27 and

Table 6. To confirm the Raman Spectroscopy results, FT-IR spectroscopy was applied. A comparative FT-IR study on the acid conformation after being exposed to metals is shown in Figure 28.

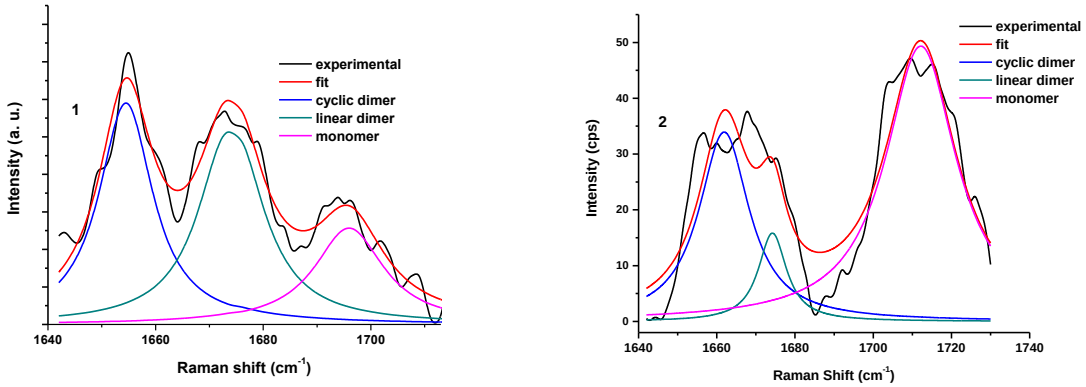


Figure 27. Curve fitted C=O region of NA in the presence of iron at 200°C (1) 2h (2) 3h. (Chakravarti et al. 2013) Reprinted with permission from Energy and Fuels. Copyright 2013 American Chemical Society

Species	20% NA-MO-RT without metal	20% NA-MO-3h
Cyclic dimer	41	31.55
Linear dimer	25	9.05
Monomer	33	59.40

Table 6. Relative concentration variance of the molecular species of naphthenic acid in a binary mixture exposed to iron powder at 200°C for 3h in comparison with that at room temperature. (Chakravarti et al. 2013) Reprinted with permission from Energy and Fuels. Copyright 2013 American Chemical Society

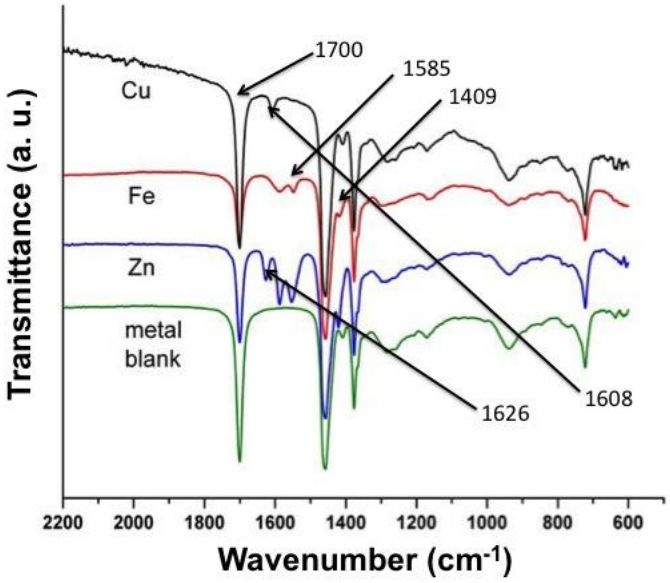


Figure 28. FT-IR spectrum of the metal naphthenates formed in-situ by the reaction of 20% naphthenic acid with corresponding metal powders held for 5h at 200°C. (Chakravarti et al. 2013) Reprinted with permission from Energy and Fuels. Copyright 2013 American Chemical Society

Microgravimetry

In-situ corrosion experiments were performed in order to understand the kinetics of the corrosion reaction between refinery materials and naphthenic acids. The importance of the in-situ testing cannot be understated; by performing these tests with time resolution, much more information about how to the reaction proceeds could be extracted than conventional testing can gain. Finally, to assist in interpreting and understanding the results for iron, experiments were performed on other transition metals. Information about the behavior of other transition metals assists with understanding the behavior of iron, as well as why certain alloys are resistant to naphthenic acid attack. Unless mentioned otherwise, all chemical corrosion data was performed in three-weight percent naphthenic acid in RLOP 600 base oil.

As the weight changes measured by microbalance are extremely small, a calibration of the system was desired. However, as there are several variables that can change the resonant frequency of the piezoelectric crystal, each had to be independently assessed.(Stienhem & Janshoff 2006) First, the change in frequency vs. temperature for the gallium orthophosphate (GAPO) crystals was mapped, as shown in Figure 29. The results from the temperature-frequency experiments were used to map the thermal frequency shift, which was used in calculating the viscosity effect. In order to ensure the viability of the microbalance in high temperature oil, viscosity measurements were used

for calibration. The viscosity of a fluid at a given pressure, temperature, and zero flow rate is a material property, and is thus acceptable for calibration. In addition, as the microbalance reacts to changes in the environment around the crystal, as well as mass loading on the surface of the crystal, viscosity measurements were an efficient way to ensure viability of the technique in the test conditions. For comparison, Chevron Co. obtained viscometric data for the same solution using a macro-viscometer. The results from experiments performed using both techniques are included in Figure 30. The deviation at low temperatures <75°C is due to the extremely high viscosity of the oil which severely damps vibrations and precludes accurate measurements. There is a small deviation at high temperature (200°C), however the discrepancy is corresponds to a small frequency shift (<50Hz) and is likely due to small deviation in temperature from the recorded value. Given that the frequency change during corrosion is often 1000-2500 Hz. per five-minute period, the small steady state deviation is acceptable.

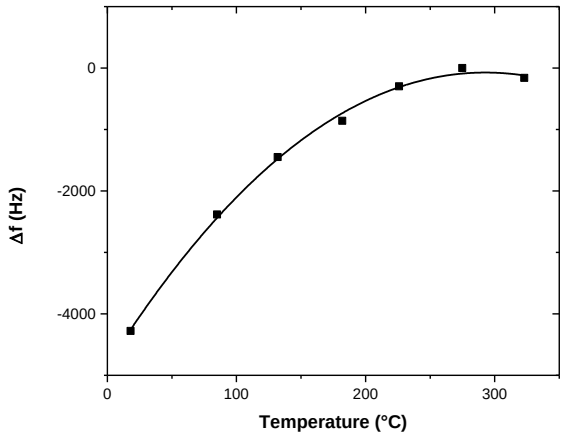


Figure 29. Change in frequency from maximum value vs. temperature for a y 12.5° cut GAPO crystal(Patrick et al. 2015b)

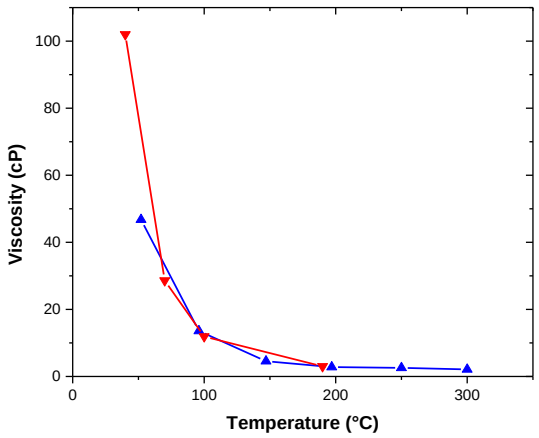


Figure 30. Viscosity comparison of RLOP600 base oil using macro viscometer and microbalance (Patrick et al. 2015b)

Microgravimetric Measurements of Iron

To measure the kinetics of the corrosion process, as well as to understand the mechanism of corrosion, dynamic corrosion experiments utilizing a crystal microbalance were performed. These microbalance experiments utilized commercial GAPO resonators with coated with gold electrodes on both sides. For experimentation, one side of the electrode was coated with approximately two µm of iron using RF sputtering as described earlier. The microstructure of the thin films was confirmed using XRD and SEM, and the crystal structure was found to be consistent with bulk iron (BCC). The XRD and SEM images of an as sputtered crystal can be found in Figure 31 and Figure 32 respectively.

Corrosion experiments were performed at temperatures commonly found within the distillation columns of a refinery (220°C-320°C). This particular range of temperatures was selected to look at how the behavior changes when naphthenic acid corrosion is active. Corrosion experiments performed at temperatures below 220°C did not yield any detectible corrosion within 24 hours. The upper limit of the temperature was determined based upon the flash point of the base oil, to ensure safety when performing tests in a glass cell. The dynamic corrosion rate data for several temperatures between 220°C-320°C are is included in Figure 33 - Figure 38, and key information from each of the plots can be seen in Table 7. It should be noted that a decrease in corrosion rate was seen between 280°C and 290°C, which may be due vaporization of naphthenic acids from the oil solution.

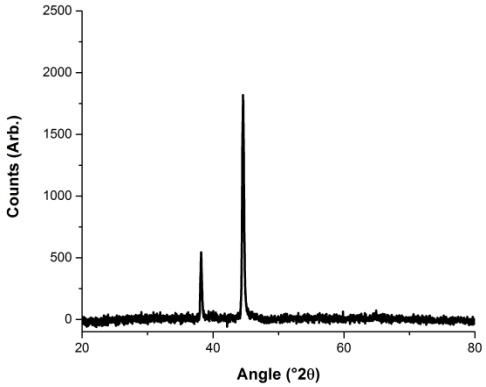


Figure 31. XRD Pattern of iron coated GAPO crystal

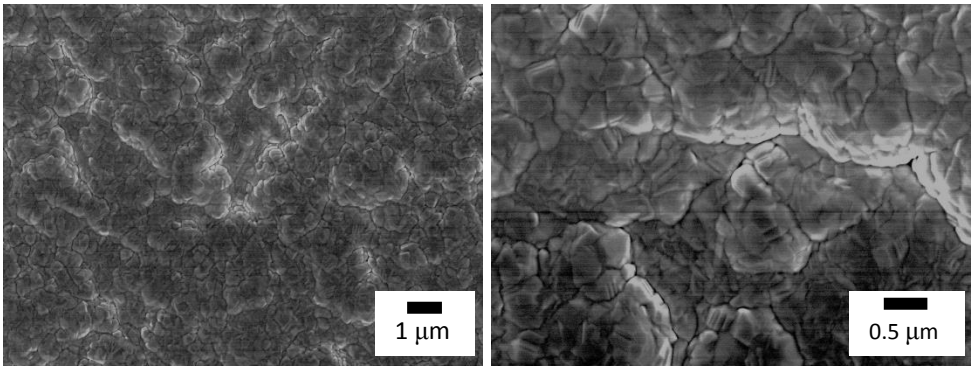


Figure 32. Left. As deposited iron structure 7500x, 5kV. Right. As deposited iron structure 52kx 5kV. (Patrick et al. 2015b)

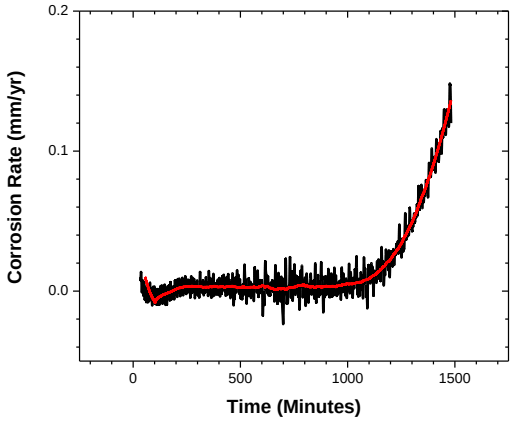


Figure 33. Corrosion rate vs. time for iron in 3 wt. percent naphthenic acid at 220°C. Red line indicates average curve fit

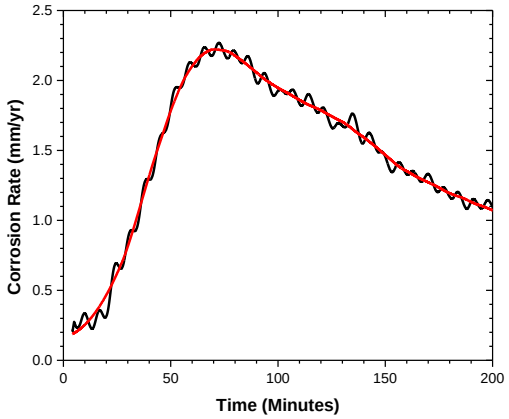


Figure 34. Corrosion rate vs. time for iron in 3 wt. percent naphthenic acid at 260°C. Red line indicates average curve fit

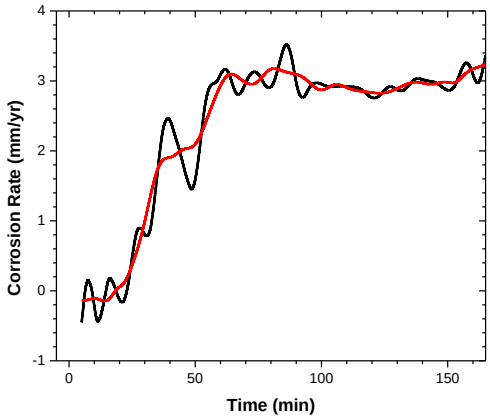


Figure 35. Corrosion rate vs. time for iron in 3 wt. percent naphthenic acid at 270°C. Red line indicates average curve fit (Patrick et al. 2015b)

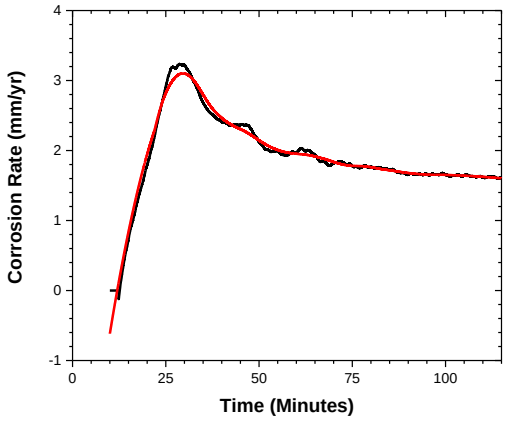


Figure 36. Corrosion rate vs. time for iron in 3 wt. percent naphthenic acid at 280°C. Red line indicates average curve fit

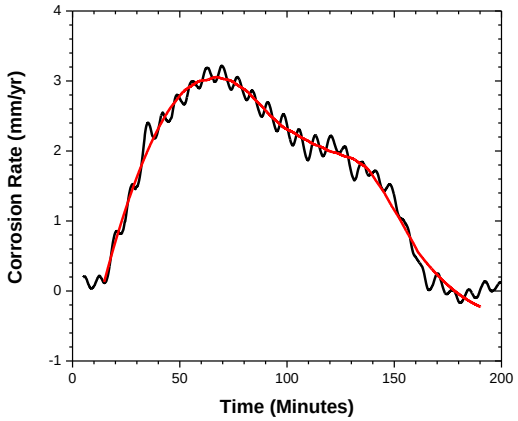


Figure 37. Corrosion rate vs. time for iron in 3 wt. percent naphthenic acid at 290°C. Red line indicates average curve fit

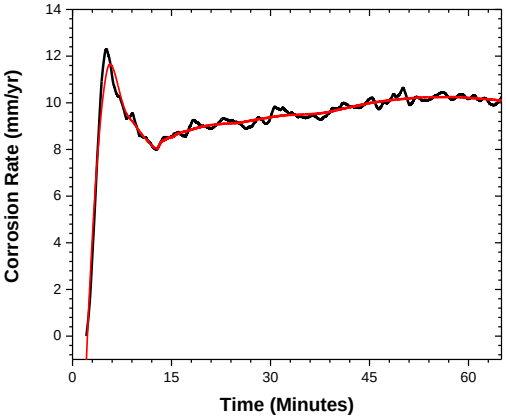


Figure 38. Corrosion rate vs. time for iron in 3 wt. percent naphthenic acid at 320°C. Red line indicates average curve fit

Temperature	Maximum Corrosion Rate (mm/yr)	Time to Lose 300 µg (min)	Time to Reach 2 mm/yr Corrosion Rate (min)
220	0.143	-	-
260	2.25	126.7	57.6
270	3.03	107.9	38.4
280	3.48	128.2	25.38
290	3.18	85.70	32.86
320	10.52	41.0	<5

Table 7. Summarized corrosion behavior of iron in three-weight percent naphthenic acid at several temperatures

The results of microstructural studies over a range of temperatures suggested that the surface structure of the iron changed as the reaction proceeded. The possibility of a surface structure change was further supported by the increasing corrosion rate vs. time seen in all of the experiments on iron, which is atypical for corrosion processes. To further understand the mechanism of corrosion, experiments were performed where the reaction was stopped at key points during the process. These interrupted experiments were performed at 270°C, and the points studied were the beginning of a positive corrosion rate, approximately halfway through the increasing corrosion portion of the curve, and finally after the steady state corrosion rate had been obtained. The interrupted experiments demonstrates another advantage over conventional corrosion testing, as the microbalance corrosion technique gives the researcher the ability to stop the process and to take "snapshots" of what is happening throughout the process. The purpose of these experiments was to address the mechanism of corrosion of iron by naphthenic acids, and the microbalance data for these experiments is in Figure 39. SEM micrographs showing the change in surface structure upon exposure to naphthenic acid as a function of time are in
Figure 40 and
Figure 41.

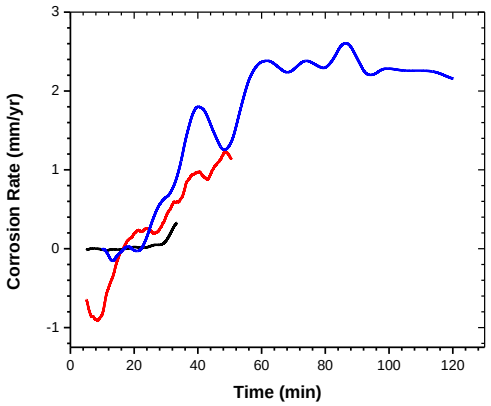


Figure 39. Corrosion rate vs. time plot for interrupted tests in 3 wt. percent naphthenic acid at 270°C. Blank: First interrupt. Red: Second Interrupt. Blue: Uninterrupted behavior

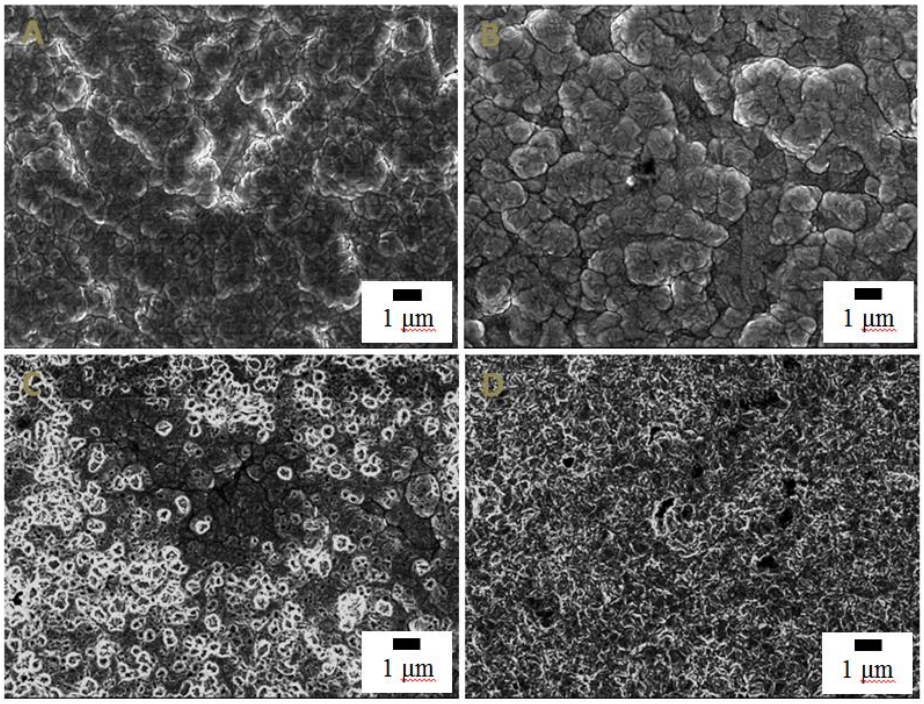


Figure 40. SEM micrographs of corroded surface of iron with progression of time at 270°C in 3 wt. percent naphthenic acid (A) Surface of as-sputtered iron (B) Surface of iron sample after a small positive corrosion rate was measured in Stage II. (C) Iron surface associated with larger positive corrosion in Stage II. (D) Iron surface after achieving steady state corrosion rate for 2.5 hours in Stage III. All images were obtained with a 5 kV beam. See blue curve in Figure 39. (Patrick et al. 2015b)

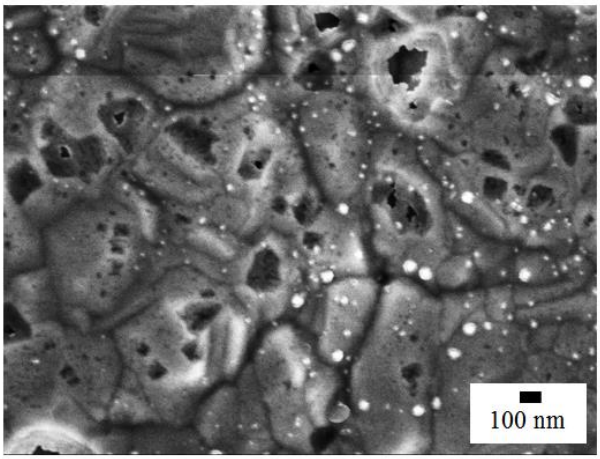


Figure 41 . High magnification SEM image of corrosion pits that formed in iron's surface oxide during early part of Stage II. Image was acquired with a 5 kV electron. (Red curve in Figure 39).(Patrick et al. 2015b)

Micrograviметry of Iron exposed to Single Acids

The term naphthenic acid is used to describe the entire range of carboxylic acids present in crude, being of various structures and sizes. As the corrosivity of crudes vary for similar TAN, it is not surprising that the structure of the acids has an effect on the corrosivity.(Dettman et al. 2009) To address the correlation between acid structure and corrosivity, the corrosion behavior of several single acids exposed to iron were compared using the microbalance technique. The acids tested include octanoic, dodecanoic, stearic, cyclohexanecarboxylic, cyclohexaneacetic, and cyclohexanebutyric acids. Each experiment was conducted at 270°C, 30 psi, and an acid concentration of 85mM. The corrosion rate vs. time plots for each of these acids are shown in Figure 42-Figure 47 below.

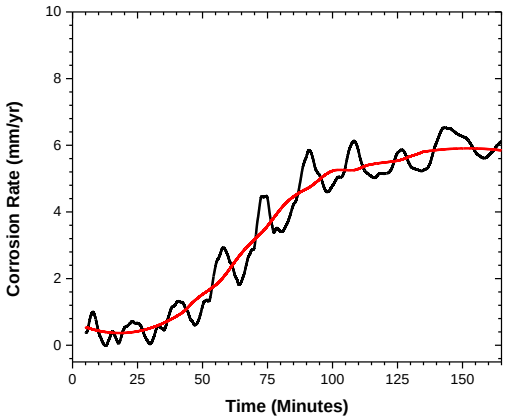


Figure 42. Corrosion rate vs. time for iron in 85 mM cyclohexanecarboxylic acid at 270°C. Red line indicates average curve fit

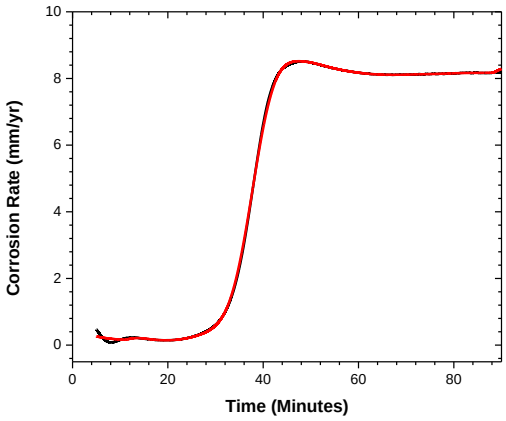


Figure 43. Corrosion rate vs. time for iron in 85 mM cyclohexaneacetic acid at 270°C. Red line indicates average curve fit

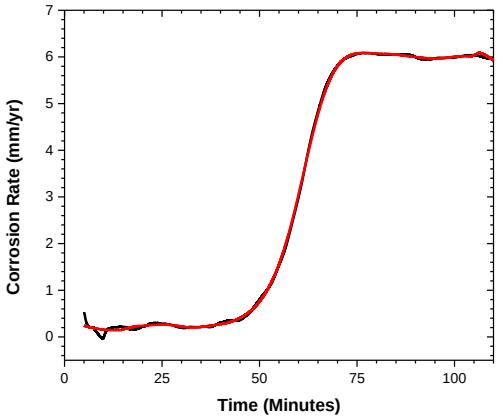


Figure 44. Corrosion rate vs. time for iron in 85 mM cyclohexanebutyric acid at 270°C. Red line indicates average curve fit

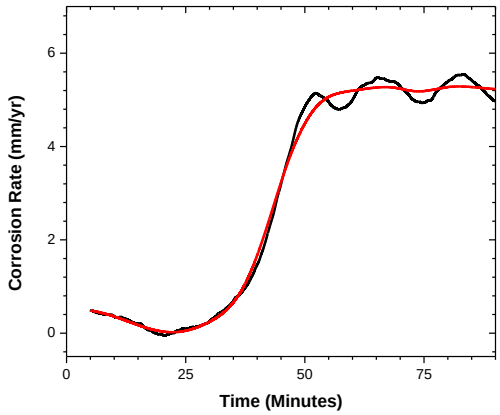


Figure 45. Corrosion rate vs. time for iron in 85 mM octanoic acid at 270°C. Red line indicates average curve fit

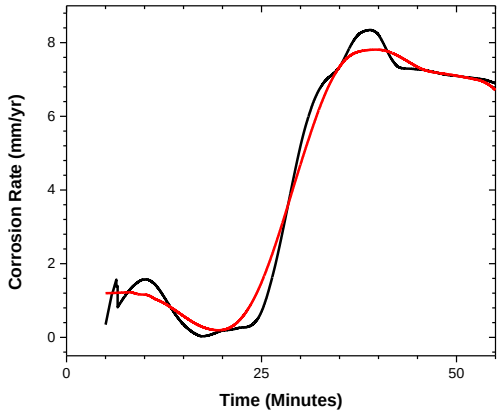


Figure 46. Corrosion rate vs. time for iron in 85 mM dodecanoic acid at 270°C. Red line indicates average curve fit

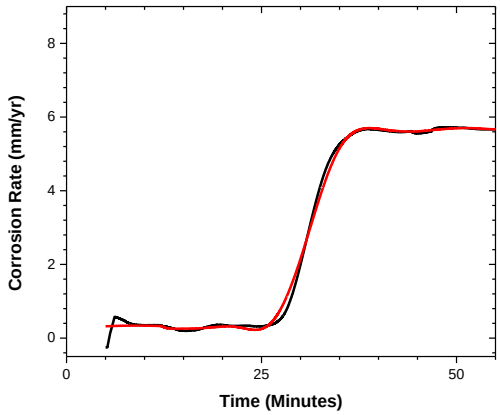


Figure 47. Corrosion rate vs. time for iron in 85 mM stearic acid at 270°C. Red line indicates average curve fit

Activation Energy Estimation for Cyclohexanebutyric Acid

Understanding the kinetics of a reaction is important to developing mitigation techniques for corrosion reactions. One important piece of information that is used to understand the kinetics is the activation energy of the reaction. Given that naphthenic acids are a mixture of acids, there is a range of activation energies present. The presence of a mixture of acids with multiple activation energies makes determination of a single value for activation energy impossible. To understand the corrosion behavior of naphthenic acids, a representative highly corrosive acid, cyclohexanebutyric acid was selected. Cyclohexanebutyric acid was selected due to its position as one of the most corrosive naphthenic acids. (Dettman et al. 2009) Experiments for determination of the activation energy were conducted over a range of temperatures between 240°-320°C. The activation energy was then calculated using the first order kinetics approximations. The corrosion rate vs. time plots for these experiments are shown in Figure 48 - Figure 51.

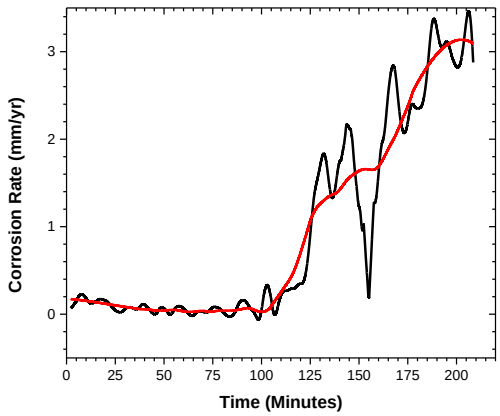


Figure 48. Corrosion rate vs. time for iron in 85 mM cyclohexanebutyric acid at 240°C. Red line indicates average curve fit

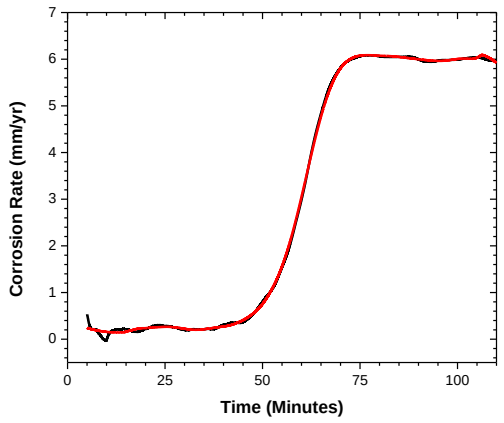


Figure 49. Corrosion rate vs. time for iron in 85 mM cyclohexanebutyric acid at 270°C. Red line indicates average curve fit

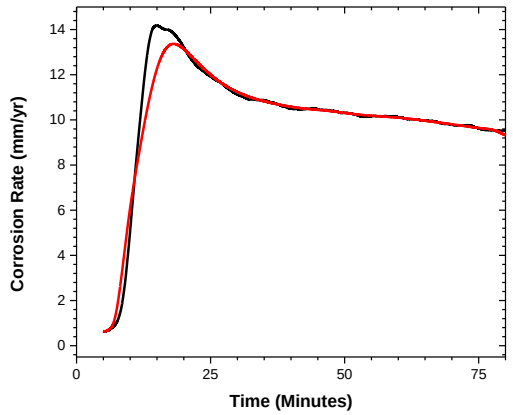


Figure 50. Corrosion rate vs. time for iron in 85 mM cyclohexanebutyric acid at 300°C. Red line indicates average curve fit

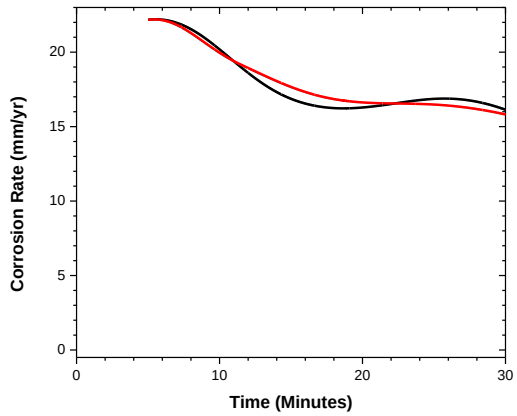


Figure 51. Corrosion rate vs. time for iron in 85 mM cyclohexanebutyric acid at 320°C. Red line indicates average curve fit

Microgravimetry of Transition Metals

As iron is not employed on its own within a refinery, the behavior of corrosion resistant alloys was of interest. However, as the behavior of alloys is complicated, the individual ferrous alloying elements were tested. By understanding how each of the other metals reacted, it was hoped that parallels could be drawn between properties of the metals and their reactivity. In addition, studying the individual alloying elements may help to understand the disparate behavior of commonly used alloys.(Gutzeit 1977; Humphries & Sorell 1976) Several transition metals, as well as common alloying elements used in the refinery were selected. The metals selected were chromium, nickel, copper, silicon (metalloid), and gold. Chromium, nickel, copper and zinc were selected as a series of transition metals in the same row as iron, which also are common alloying elements for iron in corrosion resistant alloys. Silicon was selected due to its unique properties, and the fact that it is commonly alloyed in carbon steels to improve the corrosion resistance. Gold was selected as a standard, and no corrosion was expected. The crystallinity and microstructure of each of the materials was confirmed prior to experimentation. Each of the materials was found to be crystalline via XRD, with a surface structure that was consistent with the deposition method used, studied via SEM. The dynamic corrosion experiments results from each of these metals in in Figure 52 - Figure 57. SEM micrographs showing the change in surface structure of each of the selected elements are presented in
Figure 58 - Figure 63, and the representative XRD patterns before and after experimentation are presented in Figure 64 - Figure 74. FT-IR measurements on aliquots taken after the reaction were used to measure how much of the acid was consumed during the reaction, and the results are summarized in Figure 75.

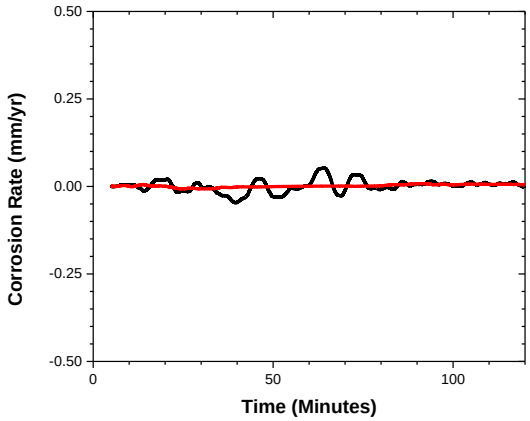


Figure 52. Corrosion rate vs. time for chromium in 3 wt. percent naphthenic acid at 270°C. Red line indicates curve fit

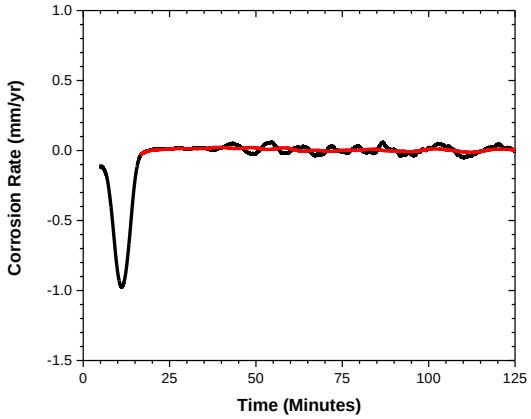


Figure 53. Corrosion rate vs. time for molybdenum in 3 wt. percent naphthenic acid at 270°C. Red line indicates average curve fit

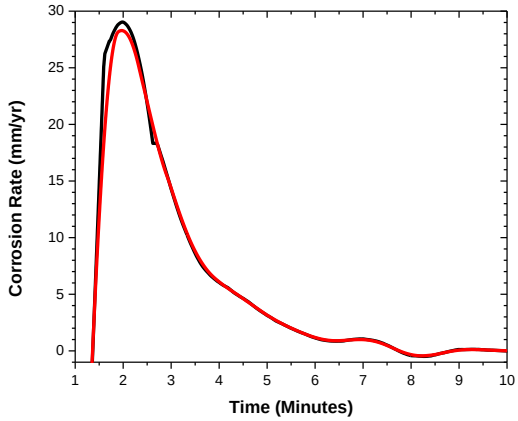


Figure 54. Corrosion rate vs. time for Zinc in 3 wt. Percent Naphthenic acid at 200°C. Red line indicates average curve fit

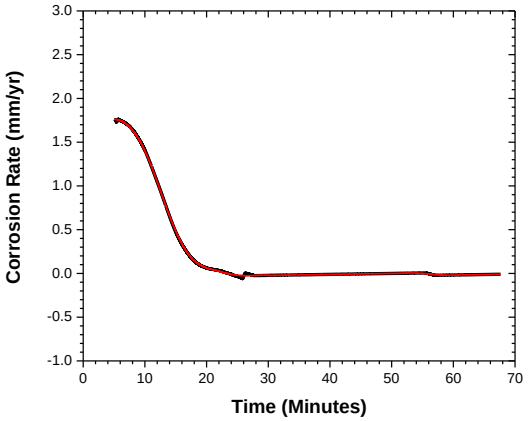


Figure 55. Corrosion rate vs. time for copper in 3 wt. percent naphthenic acid at 270°C. Red line indicates average curve fit

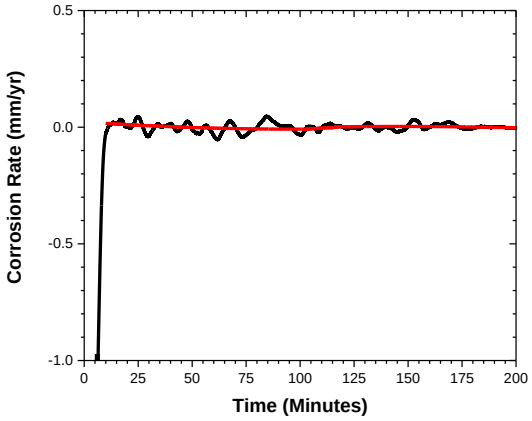


Figure 56. Corrosion rate vs. time for nickel in 3 wt. percent naphthenic acid at 270°C. Red line indicates average curve fit

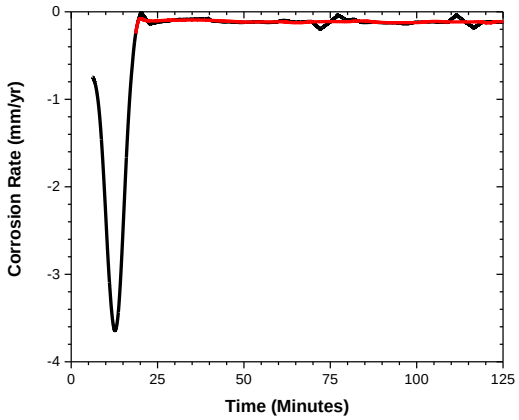


Figure 57. Corrosion rate vs. time for Silicon in 3 wt. percent naphthenic acid at 270°C. Red line indicates average curve fit.

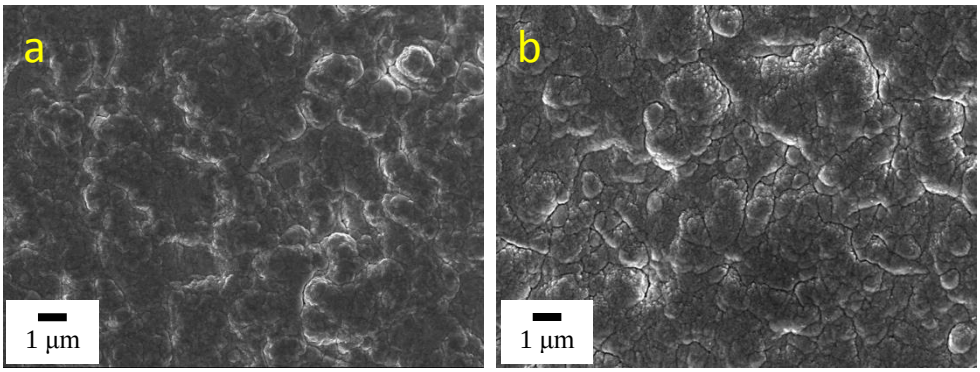


Figure 58. a) Chromium as sputtered 5kV. b) Chromium after 2 hours in 3 wt. NA at 270°C 5kV.

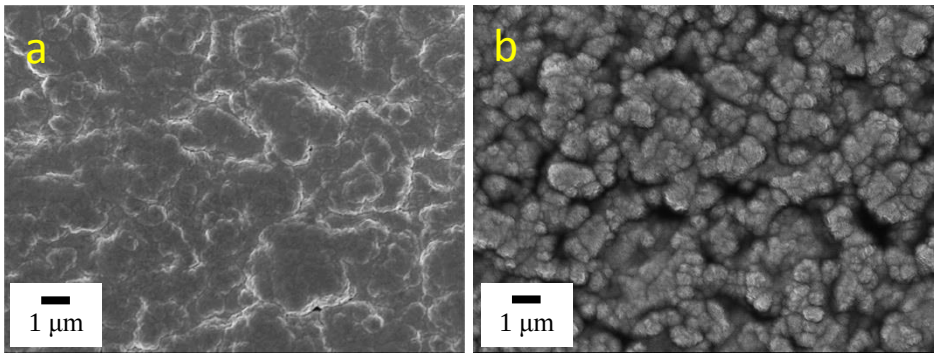


Figure 59. a) Molybdenum as sputtered 5kV. b) After 2 hours 3 wt. Percent NA at 270°C 5kV

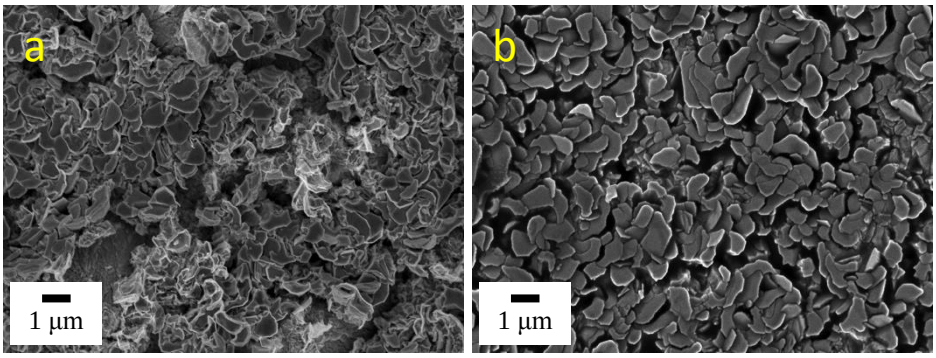


Figure 60. a) Zinc as sputtered 5kV. b) Zinc surface after corrosion in 3 wt. percent naphthenic acid 200°C for 20 minutes 5kV

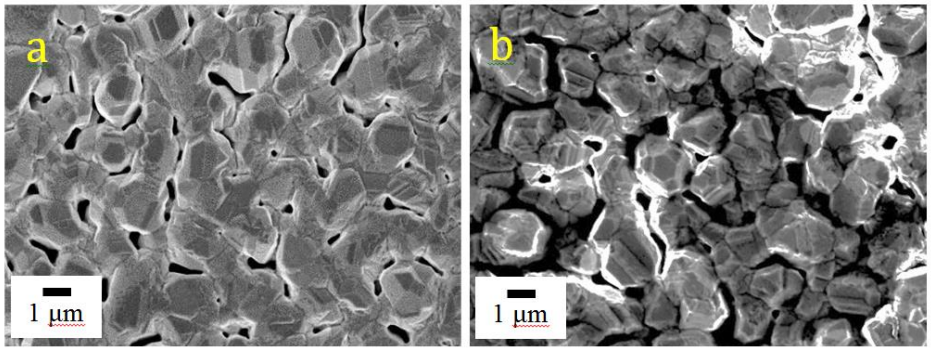


Figure 61. a) Copper as sputtered 5kV. b) Copper surface after corrosion in 3 wt. percent naphthenic acid 200°C for 20 minutes 5kV

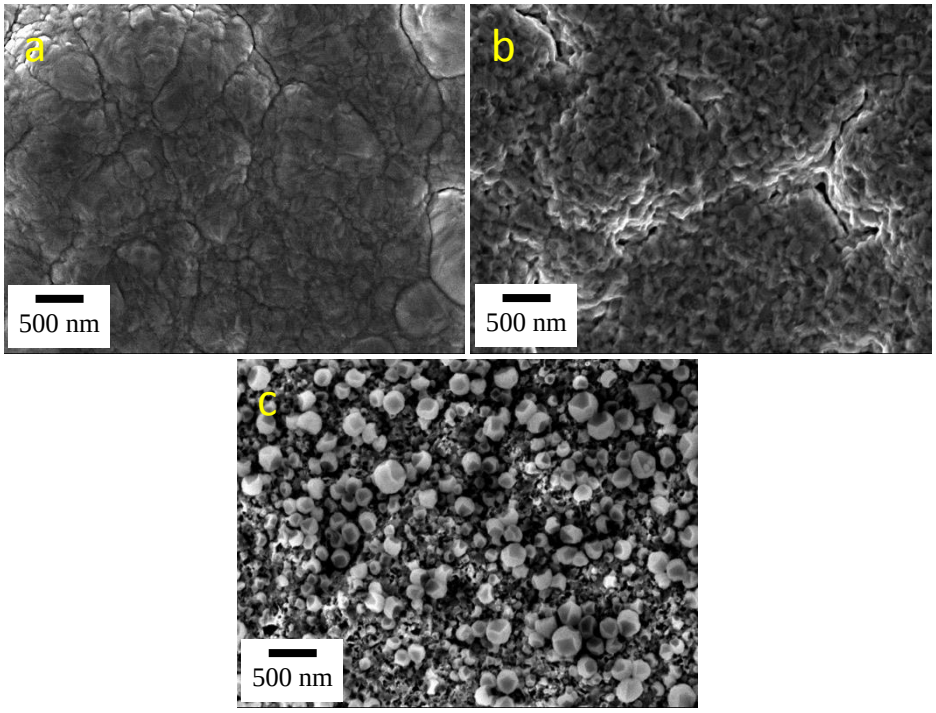


Figure 62. a) As sputtered nickel surface. b) Edge region of nickel sample after 200 minutes in 3 wt. percent NA at 270°C. c) Central region of nickel sample after 200 minutes in 3 wt. percent NA at 270°C

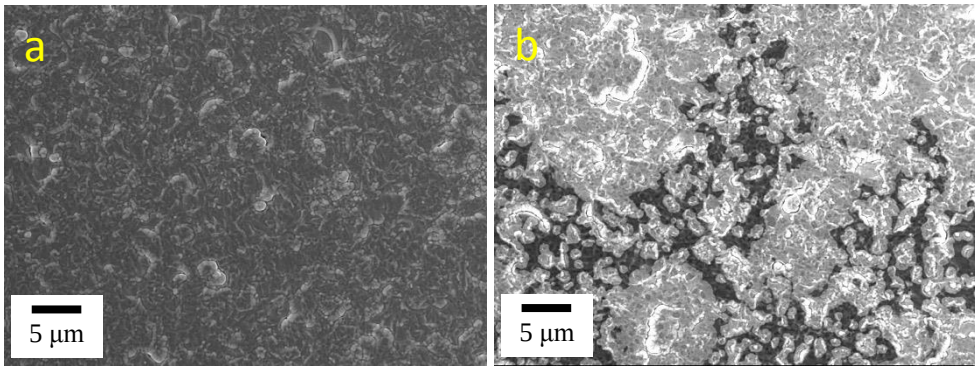


Figure 63. a) Silicon as sputtered 5kV. b) Silicon after 2 hours in 3 wt. NA at 270°C 5kV

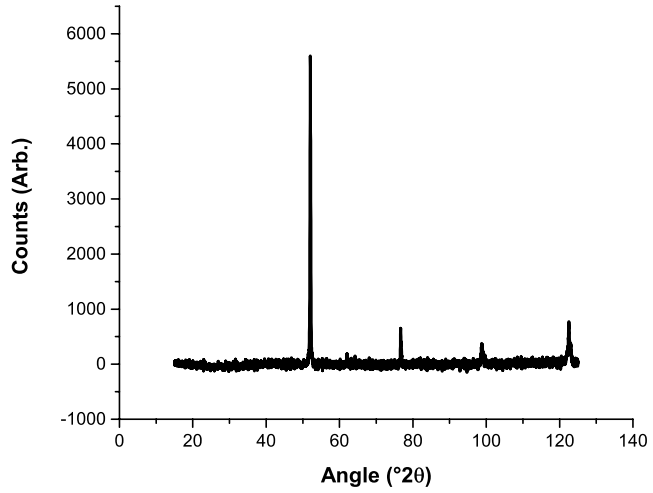


Figure 64. XRD pattern of chromium crystal as deposited.

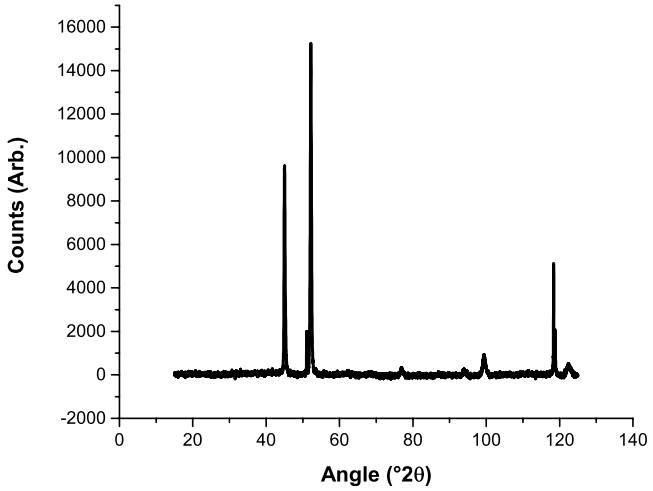


Figure 65. XRD pattern of chromium crystal after immersion in 3 wt. percent NA at 270°C

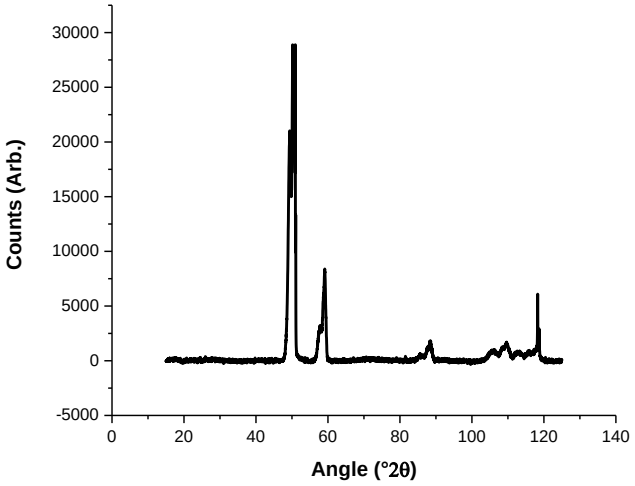


Figure 66. XRD pattern of copper crystal after immersion in 3 wt. percent NA at 270°C

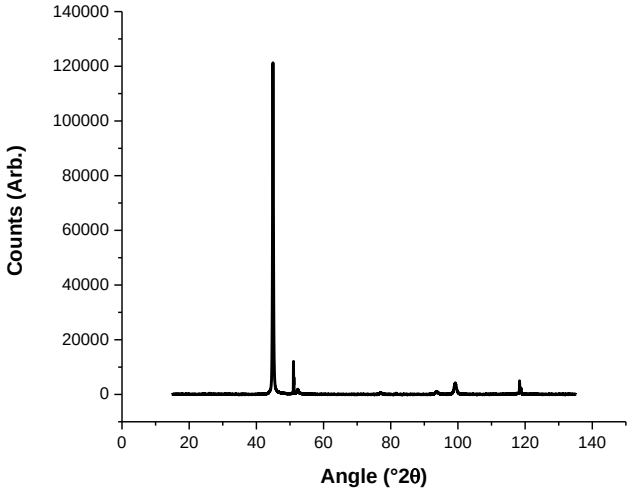


Figure 67. XRD pattern of molybdenum crystal as deposited

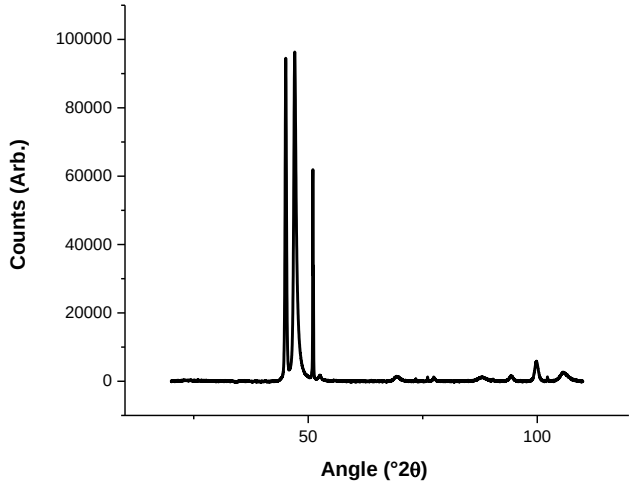


Figure 68. XRD pattern of molybdenum crystal after immersion in 3 wt. percent NA at 270°C

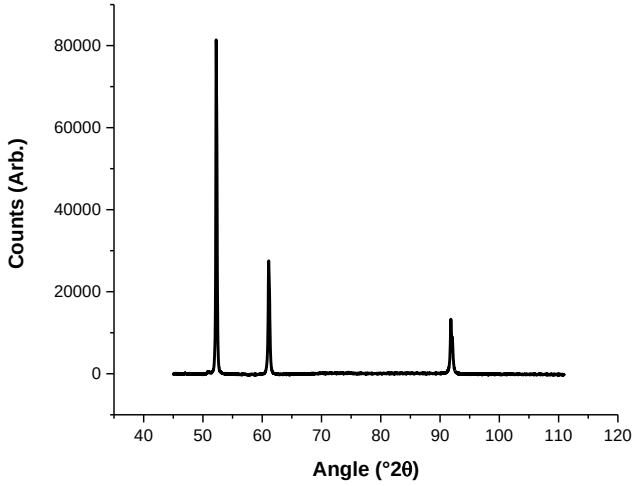


Figure 69. XRD pattern of nickel crystal as deposited

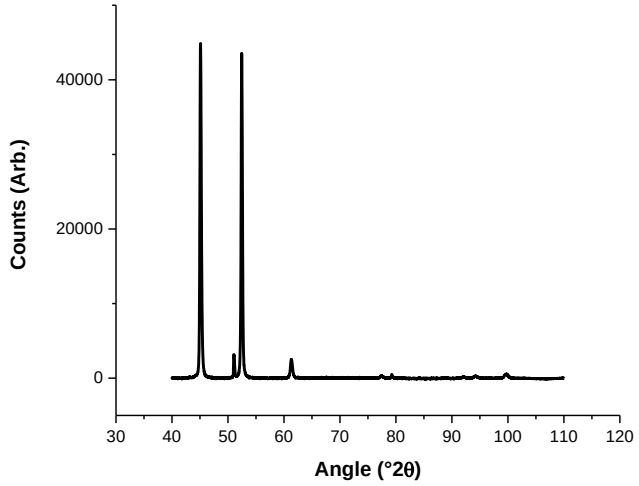


Figure 70. XRD pattern of nickel crystal after immersion in 3 wt. percent NA at 270°C

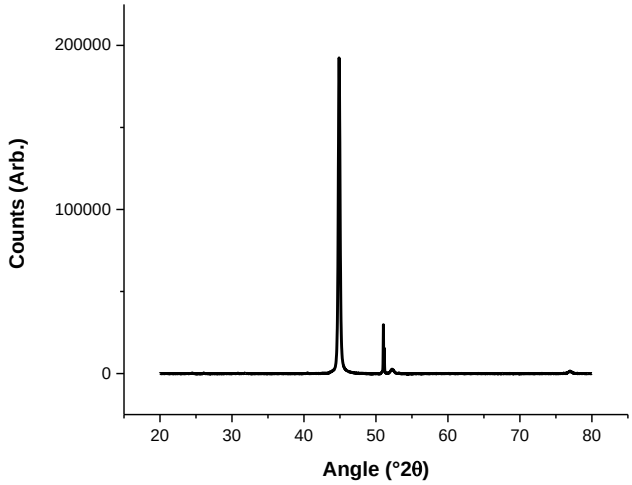


Figure 71. XRD pattern of silicon crystal as deposited

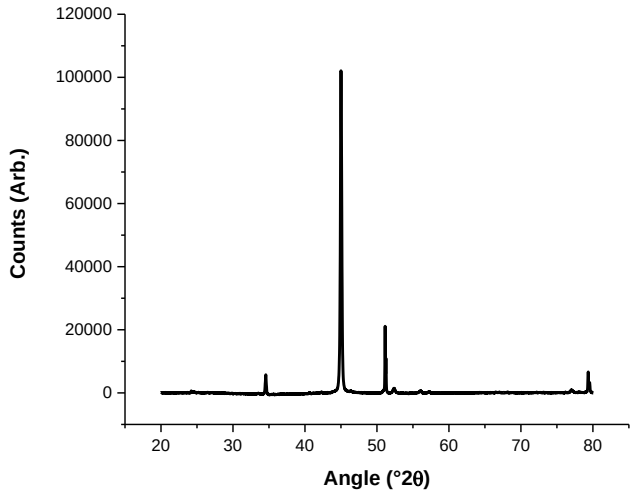


Figure 72. XRD pattern of silicon crystal after immersion in 3 wt. percent NA at 270°C

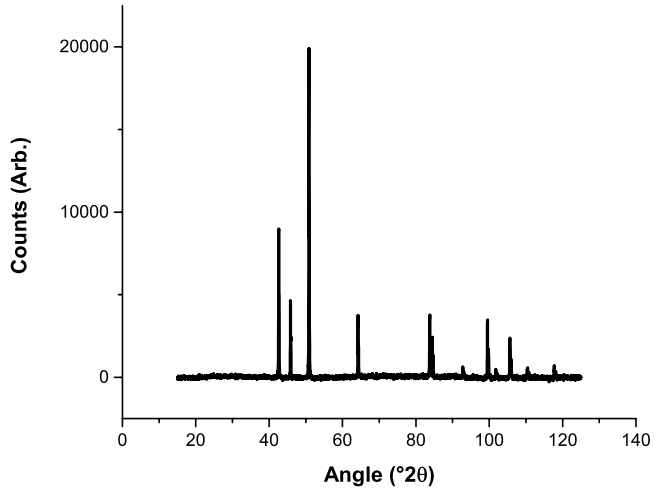


Figure 73. XRD pattern of zinc crystal as deposited

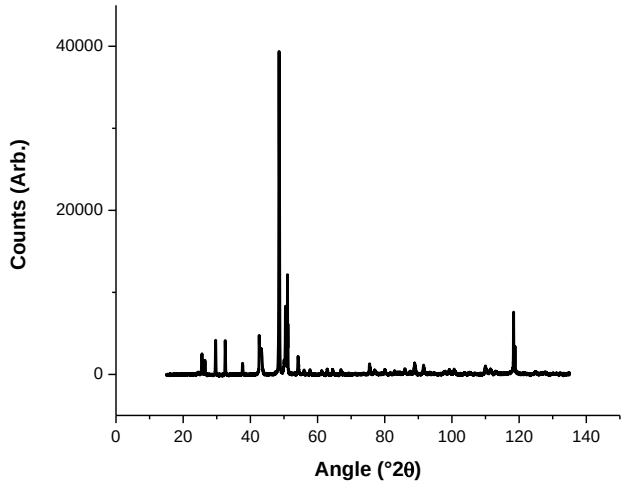


Figure 74. XRD pattern of zinc crystal after immersion in 3 wt. percent NA at 270°C

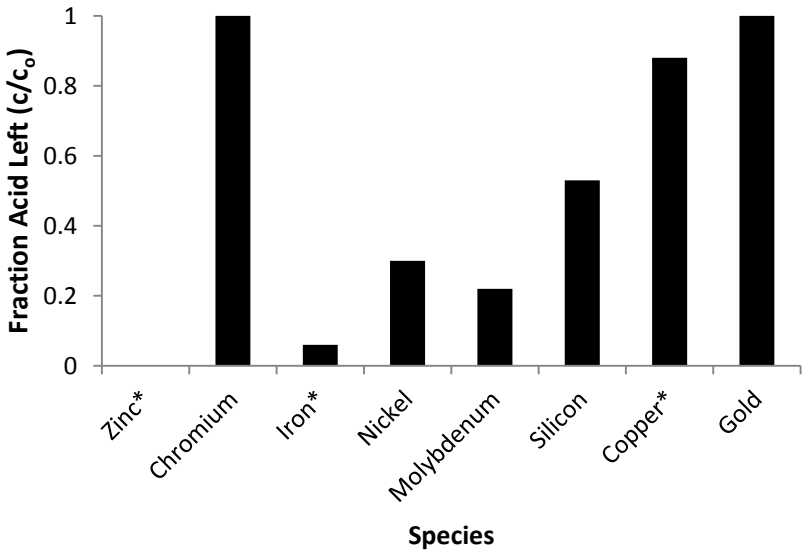


Figure 75. Results from FT-IR spectrometry experiments on powder samples. * signifies active corrosion occurring during test.

In-situ Oxide Stripping

Microbalance experiments on the selected transition metals showed that some elements were resistant to attack by naphthenic acid over the experimental timeframe. The origin of the resistance of the inert transition metals was of immense interest, as it provides information about the mechanism of corrosion inhibition. For the metal not to react with naphthenic acid, there are two possible pathways. First, the acid is not able to physically contact the metal, this pathway could occur if a film were covering the surface such as a passive metal oxide that is resistant to NA. Second, the oxide dissolves by

reacting with the acid, but in this case the metal does not react with the acid, making the metal itself immune to NA attack. In order to distinguish which of the possible scenarios is responsible for each metal's resistance, experiments were performed where the oxide was removed in-situ under an anaerobic condition. The oxide was removed via physical abrasion with a fine Arkansas stone (99.5% silica, 0.3% alumina, 0.2% other). After removing the oxide, the corrosion reaction was allowed to proceed, and then the autoclave was cooled down. Due to the nature of grinding and the short time of testing, corrosion rates could not be calculated, but surface studies were used to look for evidence of corrosion. To determine whether corrosion occurred, samples ground and exposed to naphthenic acid containing solution were compared to samples that were ground in an oil solution not containing any naphthenic acid. The SEM micrographs over a range of magnifications for copper, chromium, iron, molybdenum and nickel are in Figure 76 through Figure 80.

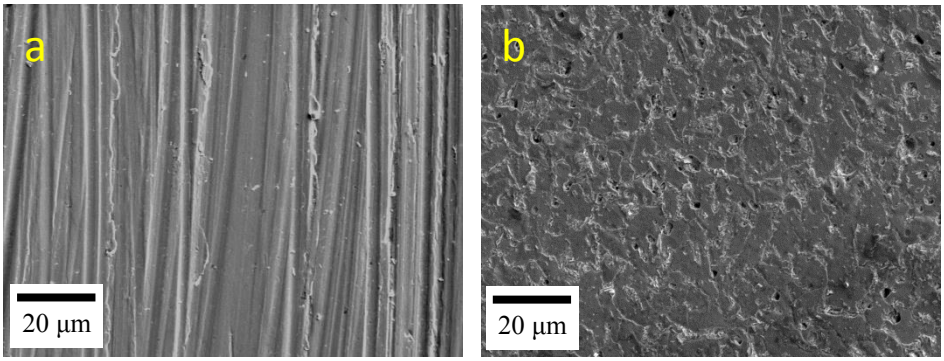


Figure 76. a) Ground uncorroded iron surface after immersion in acid-free oil for 4 h at 270°C. 5kV. b) Ground iron surface after immersion in 3 wt. percent naphthenic acid for 4 hours at 270°C. 5kV

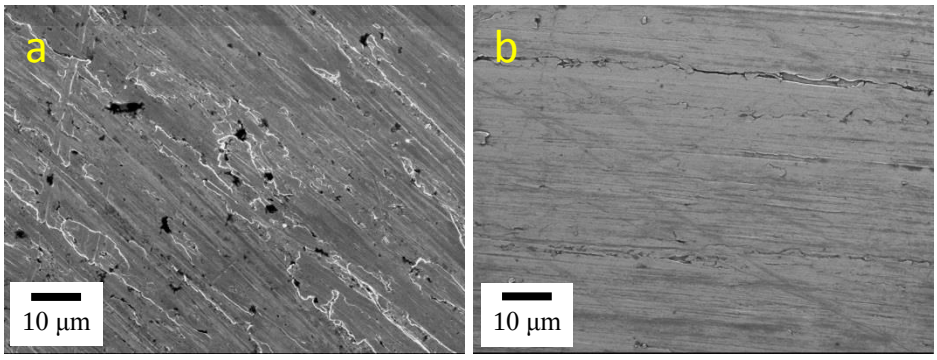


Figure 77. a) Ground uncorroded chromium surface after immersion in acid-free oil for 4 h at 270°C. 5kV. b) Ground chromium surface after immersion in 15 wt. percent naphthenic acid for 4 hours at 270°C 5kV

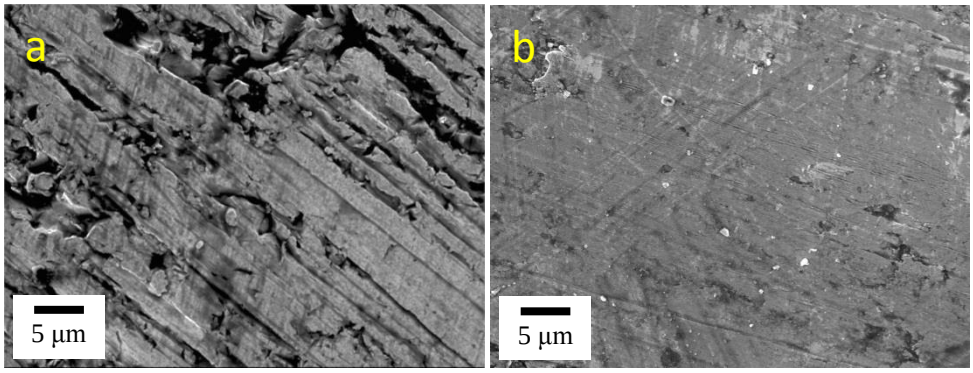


Figure 78. a) Ground uncorroded molybdenum surface after immersion in acid-free oil for 4 h at 270°C. 5kV. b) Ground molybdenum surface after immersion in 15 wt. percent naphthenic acid for 4 hours at 270°C. 5kV

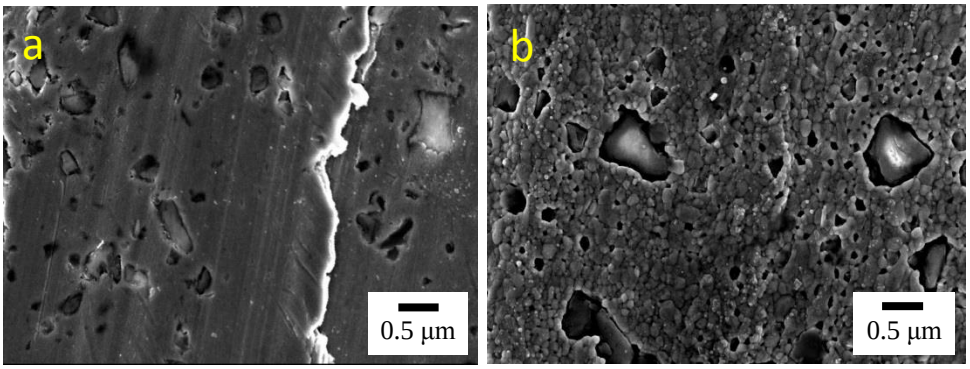


Figure 79. a) Ground uncorroded copper surface after immersion in acid-free oil for 4 h at 270°C. 5kV. b) Ground copper surface after immersion in 3 wt. percent naphthenic acid for 4 hours at 270°C. 5kV

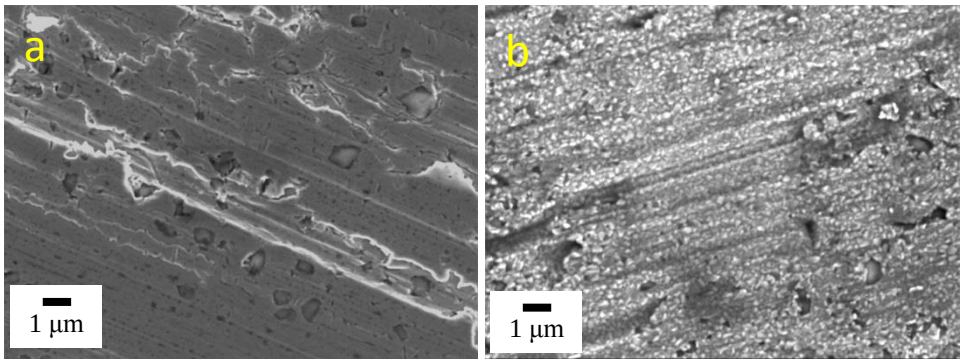


Figure 80. a) Image of ground nickel surface after immersion in acid-free oil for 4 h at 270°C. 5kV. b) Image of ground nickel surface after immersion in 3 wt. percent NA for 4 hours at 270°C. 5kV

Electrochemical Studies of the Solution

The electrochemical approach to characterize unknown crudes was performed in parallel with the chemical corrosion experiments. The objective was to develop a technique that is superior to TAN for determining the corrosivity of a crude.

While TAN does measure the ability of crude to buffer a base, it does not measure the reactivity of the acids in solution. The electrochemical approach aimed at doing exactly that—measuring the corrosivity and approximate concentrations of the naphthenic acids present in crude. However, performing electrochemical testing is an immensely difficult task as little electrochemistry is done in nonpolar solvents. Many of the results included in the following sections are aimed at developing the faculties necessary to perform electrochemical experiments in a crude oil, followed by experimental results of a voltammetric technique used to determine the presence of naphthenic acids in an oil sample.

Supporting Electrolytes and Solution Conductivity

In order to perform electrochemical tests, it is necessary to have a solution with adequate conductivity. To understand the importance of electrical conductivity, it is possible to model the electrochemical cell using an equivalent circuit. If a Randles circuit is used to model the cell (Figure 81), then if the solution resistance (R_s) is too high, then all of the potential is dropped across the resistor, and no other information about the cell can be gained. Consequently for the applied potential to be dropped across the metal-solution interface, the solution must have adequate conductivity. While ideally no additional species would be added to the oil for testing, testing without supporting electrolytes was not possible due to the extremely high resistivity of crude (~10^{10}-10^{15} Ω-cm).

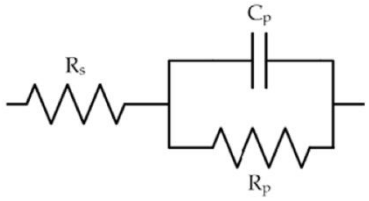


Figure 81. Randles equivalent circuit. R_s=Solution resistance, R_p=Polarization resistance, C_p=Double layer capacitance

To reduce the resistivity of the mock crude oil to a value that allowed electrochemical testing, supporting electrolytes were added. The supporting electrolytes are additional ionic species that are added to increase the conductivity of the solution, while not participating in any electrode reactions. The supporting electrolytes were chosen based upon commercial availability, and were chosen to be as large, bulky, and as non-reactive as possible. Several different ionic liquid classes were initially tested based on the alkyl-imidazolium, alkyl-ammonium, and alkyl-phosphonium cations.

To assess the conductivity a two-point probe was used in high resistivity solutions, and a four-point probe as well as EIS were used in low resistivity solutions. The reasoning for using two experimental configurations will be expounded upon in the discussion section. To ensure the viability of the technique as well as the cell for measuring high resistivity solutions, the two point probe technique was calibrated using several pure solvents with known resistivities.(Washburn n.d.) The experimental data

was then compared with literature data, as shown in Table 8, and are in good agreement with the literature. The deviation for toluene is likely due to a small amount of contaminant in the toluene tested, as the toluene was of reagent grade and was not dried before use. After the viability of the technique was ensured, testing was done on 0.4M solutions of each of the aforementioned ionic liquids. The results from the conductivity tests are presented in

Table 9.

Solution	Measured Resistivity (Ω-cm)	Literature (Ω-cm)
2DI Water	$3.00x10^{7}$	$7.70\ x10^{7}$
Ethanol	$1.25x10^{8}$	$1.20\ x10^{8}$
2-Propanol	$2.00\ x10^{8}$	$8.00\ x10^{7}$
Benzyl Benzoate	$2.75\ x10^{8}$	$1.0\ x10^{8}$
Dichloromethane	$2.27\ x10^{11}$	$1.00\ x10^{11}$
Chloroform	$1.30\ x10^{12}$	Not Reported
Toluene	$4.00x10^{11}$	$4.00\ x10^{12}$
Mineral Oil	$3.50x10^{14}$	$1\ x10^{11}$ - $1\ x10^{15}$

Table 8. Resistivity comparison of pure solvents (Washburn)

Solution	Resistivity (Ω-cm)
Toluene	$1.7x10^{13}$
Sat. TBAP	$3.60x10^{12}$
Sat. [bmim][TFB]	$3.29x10^{11}$
0.4M $P_{6,6,14}$ [BIS]	$2.99x10^{9}$
0.4M $P_{6,6,14}$ [DCN]	$1.16x10^{8}$
0.4M $P_{6,6,14}$ Do[DBS]	$8.48x10^{7}$
0.3M $P_{6,6,14}$ TKIS	$1.7x10^{4**}$ **Due to low resistivity, the four-point probe configuration was used.

Table 9. Electrical resistivity for ionic liquids solutions in toluene

Supporting Electrolyte Voltage Stability

For a supporting electrolyte to function as such, it must not participate in any charge transfer reactions in the voltage region of interest. For each of the ionic liquids tested, it was necessary to ensure a large voltage window for experimentation. In order to confirm whether an ionic liquid was suitable, large polarization cyclic voltammetry was used. The ionic liquid stability tests were performed with a platinum ultramicroelectrode

and a palladium hydride reference electrode in benzyl benzoate. Benzyl benzoate was selected as the solvent due to its low dielectric constant (ε=4.8) compared to dichloromethane, and its increased conductivity compared to toluene ($2x10^9$ Ω-cm vs. $4x10^{11}$ Ω-cm), which allowed for data collection without significant IR drops. (Gibson & Lloyd 1970) In addition, experiments for $P_{6,6,614}$[TKIS] in toluene and benzyl benzoate yielded identical stability limits, indicating the solvent's inertness over the testing region. The region of stability was calculated based upon the potential at which the current began to increase to 1.5 nA from background. It should be noted that a change in current scale by the potentiostat during an experiments induced an artifact with a current response similar to a plot of 1/x. The sharp peaks were repeatable, and are not representative of any species present in the solution. The identification of the artifacts was confirmed on $P_{6,6,614}$[TKIS] with another Gamry PCI-750 potentiostat as well as a Solartron Modulab. The voltammograms from each of the ionic liquid stability experiments are in Figure 82 - Figure 86.

Table 10 summarizes the stability limits for each of the ionic liquids.

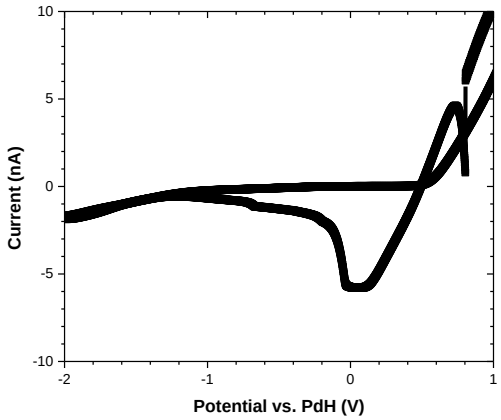


Figure 82. Voltammogram for stability of 0.4M $P_{6,6,14}$ [Cl] in Benzyl Benzoate

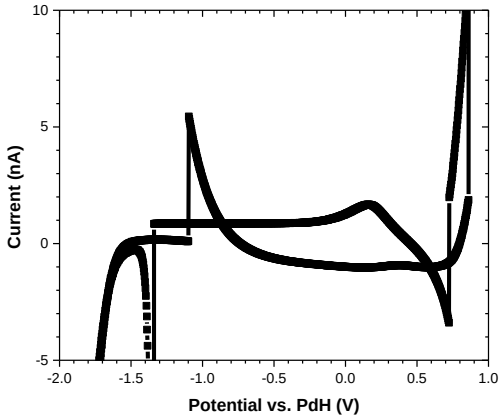


Figure 83. Voltammogram for stability of 0.4M $P_{6,6,14}$ [Br] in Benzyl Benzoate

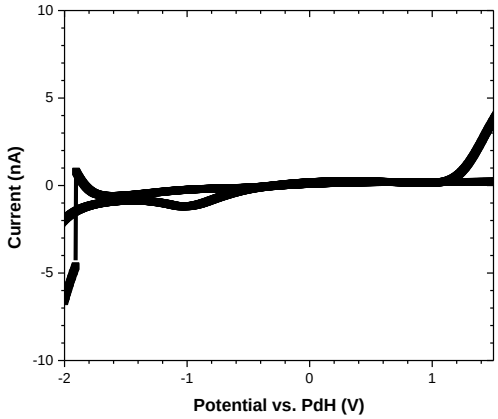


Figure 84. Voltammogram for stability of 0.4M $P_{6,6,14}$ [BIS] in Benzyl Benzoate

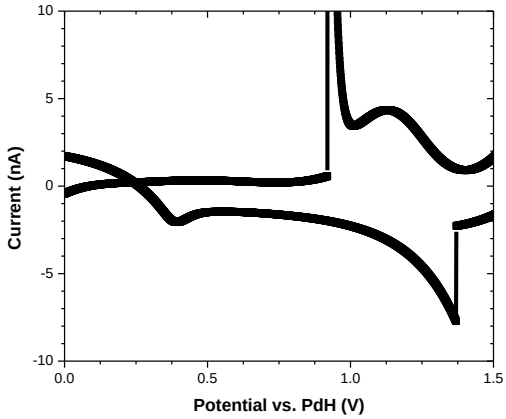


Figure 85. Voltammogram for stability of 0.4M $P_{6,6,14}$ [DCN] in Benzyl Benzoate

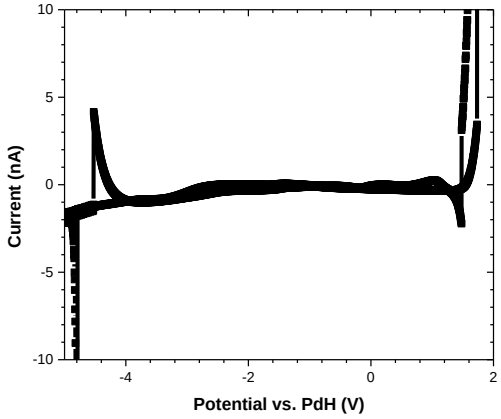


Figure 86. Voltammogram for stability of 0.4M $P_{6,6,14}$ [TKIS] in Benzyl Benzoate

Ionic Liquid	Cathodic Limit	Anodic Limit	Stability Range
$P_{6,6,14}$ [Cl]	-1.55	0.55	2.1
$P_{6,6,14}$ [Br]	-1.6	0.75	2.35
$P_{6,6,14}$ [Phos]	-1.7	1.25	2.95
$P_{6,6,14}$ [DCN]	-0.05	0.95	1
$P_{6,6,14}$ [TKIS]	-4	1.5	5.5

Table 10. Stability limits of phosphonium based ionic liquids

Palladium Hydride Reference Electrode

Quantitative electrochemical experiments that can be compared across a range of solution chemistries need a point of reference. The point of reference comes in the form of a stable potential, which is generally formed by a reference electrode. There are many reference electrodes available for working in aqueous solutions due to the ability of water to solvate many ions, however in nonpolar aprotic solvents none are available. Oils in particular have a very low ability to solvate ions, which makes identification of a reference electrode much more difficult. The results from experiments to verify the use of palladium hydride as a reference electrode are below.

To confirm that the palladium hydride system acts as a reference electrode in aprotic systems, several tests were performed. These tests were performed to ensure that the palladium hydride redox system is stable in aprotic solvents, that the reaction is reversible, and also that the potential of the redox equilibrium can be related back to the hydrogen scale. The tests were performed in dichloromethane due to the availability of literature data for comparison. The dearth of literature reports in less polar solutions precludes testing that can be compared to the results of other researchers. The supporting electrolyte used in these experiments was 1-butyl-3methyl-immadizolium tetrafluoroborate so that results could be directly compared to those in the literature.

Initially, the Nernstian behavior of the PdH electrode was tested. The determination of Nernstian behavior was done using commercial buffers, and the results are in Figure 87. The slope was 62.5 mV/pH in the pH range of 2-9. The stability of a PdH electrode was measured in both protic (water) and aprotic (acetonitrile) solvents. The stability of the PdH electrode was investigated by measurements of its potential as a function of time. Figure 88 presents the potential drift of a PdH electrode vs. an SCE in a pH 4 buffered 0.1M potassium chloride solution over 8 hours. Figure 89 presents the variation of the potential of PdH measured in forming gas saturated 0.2M TBAP acetonitrile, with respect to a modified saturated calomel electrode, which consisted of mercury/calomel immersed in lithium chloride saturated ACN with 0.2M TBAP. Stability measurements were made in ACN rather than DCM in order to avoid the possibly high LJP between ACN and DCM. Experiments were also performed as a function of partial pressure of hydrogen, to ensure Nernstian response. These experiments were performed using two partial pressures of hydrogen, forming gas (0.04 atm H_2) as well at 1atm of hydrogen gas. The open circuit voltage was measured

between a palladium hydride electrode and an aqueous SCE. The solvents selected for studying the effect of the solvent identity were acetonitrile, dichloromethane, dimethylsulfoxide, and dimethylformamide, and the results are summarized in Table 14. The results of experiments conducted in DMF were consistent in direction with the Nernst equation for a hydrogen electrode, however the magnitude of the potential shift was greater than predicted by theory. The reason for the greater potential shift than expected is currently unknown. The experiments in ACN, DCM, and DMSO yielded a potential shift that was consistent in magnitude, but opposite in direction as predicted by the Nernst equation of a typical hydrogen electrode. Possible reasons for the contrary behavior of PdH in these three aprotic solvents, and the implications of these results will be addressed in the discussion section.

After confirming the stability of the PdH electrode, experiments were performed to ascertain whether PdH could act as a reference electrode in aprotic solvents. These studies were done in a two-electrode cell with a Pt UME and combined CE/RE of PdH in DCM with 0.2 [bmim][TFB] and with 0.1mM additions of anthraquinone (AQ), ferrocene (Fc), and decamethylferrocene (dmFc). AQ, Fc and dmFc are organic species with redox potentials that have been measured by other researchers against the hydrogen scale in dichloromethane. A cyclic voltammogram (CV) that is representative of a series of CVs is presented in Figure 93. The IR-corrected voltammogram is presented in Figure 94. IR correction was done post experimentation utilizing resistance measurements. A total of 11 CVs were measured using the same Pt UME and four different PdH electrodes. Each test was performed with fresh solution. The results of the 11 tests are summarized in

Table 11.

To confirm that the PdH electrode was reversible, small amplitude cyclic voltammetry was done. These experiments were performed using a PdH UME and a large PdH CE/RE in a forming gas saturated dichloromethane containing 0.2M [bmim][TFB] . The PdH electrode was subjected to a small polarization (0 to +10 mV to -10mV) and the current (I) – voltage (V) behavior was recorded, as presented in Figure 90.

After confirming that the PdH electrode is stable and reversible, and thus acts as a reference electrode in dichloromethane, additional experiments were focused on determining how PdH functions in an aprotic solution. Three additional sets of experiments are presented: CVs conducted with larger voltage amplitudes in aprotic solutions and in aqueous solutions, and potentiostatic tests conducted in aprotic solutions.

The I-V behavior of a PdH UME subjected to repeated small amplitude polarizations (i.e., ±0.010V) is presented in Figure 91. The results clearly indicate the presence of a hysteresis. To study the reason for the hysteresis, experiments were performed in aqueous solutions. The results presented in Figure 92 show that the I-V behavior of a PdH UME subjected to relatively large polarizations in aqueous 0.1M HCl exhibits a hysteresis that is similar to the hysteresis measured in the aprotic solution and displayed in Figure 91. Additional experiments were performed as a function of sweep

rate to understand the origin of the hysteresis. These experiments were performed over a slightly higher potential range (±50mV), and the results indicate that the hysteresis increase with increasing scan rate. The results of the small amplitude cyclic voltammetry hysteresis experiments are summarized in

Table 15. Assuming that the palladium hydride interface can by modeled by a Randles circuit, then the hysteresis is associated with the parallel capacitance. It is likely that the capacitance is associated with the double layer charging, however other possible causes include capacitance of the UME and mass transfer processes.(Aoki 1993; Macdonald 1978; Orzazem & Tribollet 2008)

Finally, experiments were performed to try to confirm that the surface of the ß-PdH is the source of hydrogen and hydrogen ions available for oxidation/reduction (H and H^+, or H and H^-). To determine that both hydrogen and hydrogen ions are present in the PdH electrode, a set of chronoamperometry experiments was conducted. The potential of ß-PdH UME was switched between ± 0.5V vs. PdH for pulse lengths of 5 s, 50 s, and 500 s and current was measured as a function of time. A total of 12 cycles were conducted for pulse lengths of 5 s and 50 s, and 5 cycles for pulse lengths of 500 s. Selected results are presented in Figure 95 through Figure 100.

Electrode	Trial	$E_{1/2}$ AQ (V)	$E_{1/2}$ dmFc (V)	$E_{1/2}$ Fc (V)
1	1	-0.730	0.102	0.665
1	2	-0.715	0.099	0.665
1	3	-0.725	0.100	0.625
2	1	-0.710	0.105	0.664
2	2	-0.702	0.107	0.669
2	3	-0.705	0.113	0.677
3	1	-0.717	0.097	0.625
3	2	-0.714	0.100	0.623
4	1	-0.717	0.097	0.648
4	2	-0.722	0.095	0.623
4	3	-0.710	0.095	0.623
Average		-0.715	0.100	0.646
Standard Deviation		0.009	0.005	0.023

Table 11. Summary of half wave potentials for 0.1mM of AQ, dmFc, and fc in 0.2M [bmim][TFB] DCM. 10 µm platinum UME working electrode, large palladium hydride CE/RE, scan rate 100 mV/s

Redox Systems	$\Delta E_{1/2}$ Exp. (V)	$\Delta E_{1/2}$ Literature	Deviation (V)
AQ - dmFc	0.815	0.765[10,11]	0.05
AQ - Fc	1.361	1.315[10,11]	0.046
AQ* - dmFc	0.771	0.765 [10,11]	0.006
AQ* - Fc	1.313	1.315 [10,11]	0.002
dmFc-Fc	0.546	0.541[0]	0.006

Table 12. Comparison of redox species potential differences. *DCM was exposed to water

Redox Species	$E_{1/2}$ vs. PdH (V) Exp.	$E_{1/2}$ vs. SHE (V) Literature	Deviation (V)
AQ	0.715 (-0.667*)	-0.635[11]	0.08 (0.032*)
dmFc	0.101	0.13[10]	0.029
Fc	0.646	0.68[10]	0.034

Table 13. Comparison of CV data of known redox species vs. PdH study. *DCM was exposed to water

* The relatively large discrepancy of 0.080V between the measured value of the half-wave potential of AQ and that reported by Ahmed and Khan is attributed to the more thorough dehydration of DCM in this study, as the half-wave potentials of quinones first reduction shifts to more negative values as water is removed from the solvent.(Ahmed et al. 2007; Ahmadjian & Brown 1976; Gupta & Linschitz 1997; Hui et al. 2010)

Solvent	ΔE 0.04 atm H_2 (V)	ΔE 1 atm H_2 (V)	ΔE (V)
Dichloromethane*	-0.117	-0.081	+0.036
Dimethylsulfoxide	-0.435	-0.397	+0.038
Acetonitrile	-0.26	-0.224	+0.036
Dimethylformamide	-0.265	-0.32	-0.055

Table 14. Test for Nernstian behavior in several solvents. All measurements made with reference to aqueous SCE. * Experiment also performed using half wave potential shift of dmFc vs. PdH reference electrode with identical results

Scan Rate (mV/s)	Potential at I=0 (+) (mV)	Potential at I=0 (-) (mV)	Total Hysteresis (mV)
10	4.6	0	4.6
25	12.5	-3	15.5
50	19	-10.5	29.5
100	30.75	-25	55.75

Table 15. Hysteresis results of variable scan rate experiments. Working electrode 0.003" PdH, CE/RE 1 aq. in. PdH foil. Solution 0.2M [bmim][TFB] in DCM saturated with forming gas

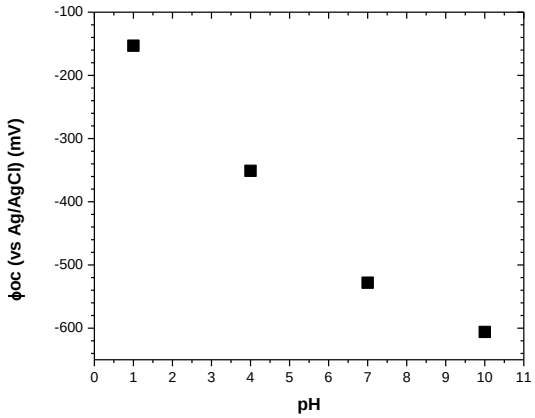


Figure 87. Potential vs. pH diagram of PdH vs. SCE electrode in commercial pH buffers containing 0.1M KCl

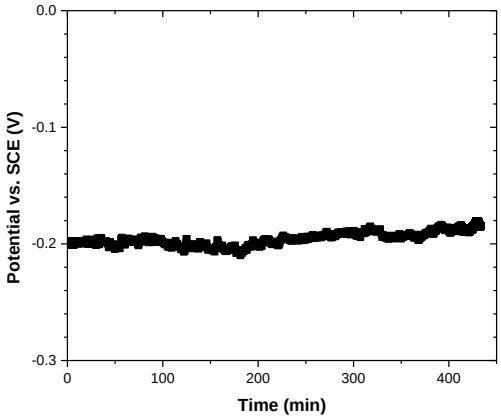


Figure 88. Open circuit potential of PdH vs. SCE in pH 4 buffered 0.1M potassium chloride in water. Potential drift of 10 mV over 8 hours

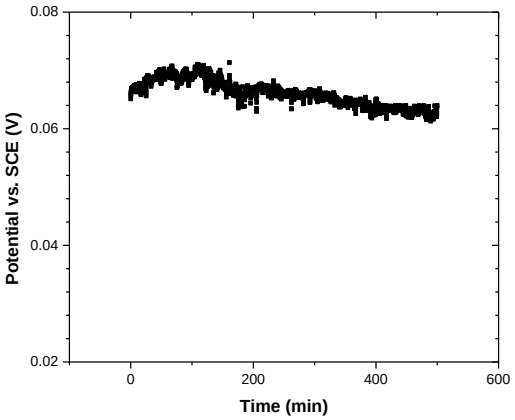


Figure 89. Open circuit potential of PdH electrode vs. modified SCE in 0.2M TBAP in CAN

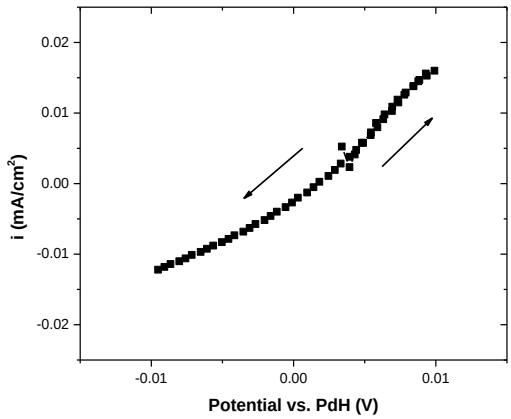


Figure 90. I vs. V plot of β-PdH UME in 0.2M [bmim][TFB] in DCM saturated with Forming Gas during polarization from 0 to +10 mV to -10 mV at a rate of 10 mV/s. The curve obtained by sweeping the potential in the positive direction was identical to the curve obtained by sweeping the potential in the negative direction.

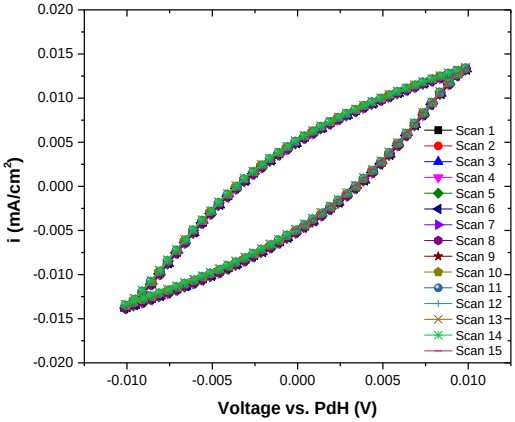


Figure 91. I vs. V plot of ß-PdH UME in 0.2M [bmim][TFB] in DCM saturated with forming gas during 10mV small polarizations from open circuit at a rate of 10 mV/s, cathodic scan first

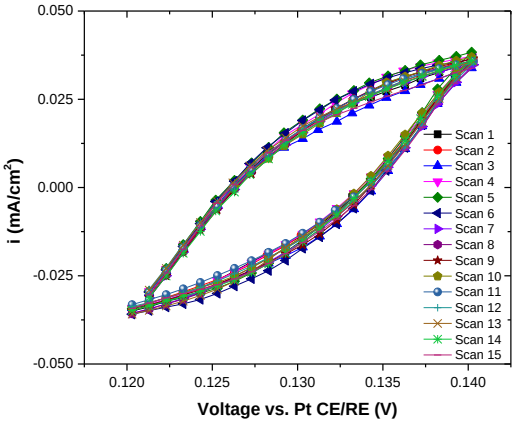


Figure 92. I vs. V plot of ß-PdH UME in 0.1M HCl saturated with forming gas during 10mV small polarizations from open circuit at a rate of 10 mV/s, anodic scan first. Platinum foil counter/reference electrode

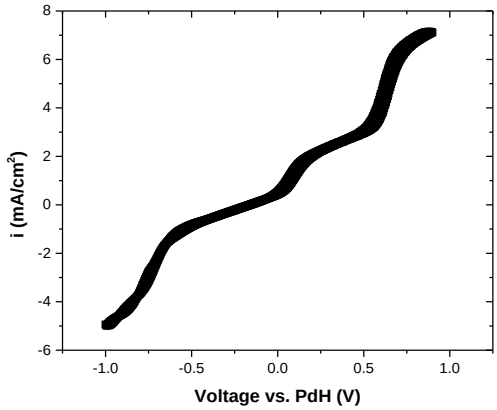


Figure 93. Cyclic voltammogram of Pt UME WE immersed in 0.2M [bmim][TFB] in DCM with 1 mM ferrocene, 1 mM anthraquinone, and 1 mM decamethylferrocene. The cell was a two electrode cell containing a 1 in2 PdH RE/CE

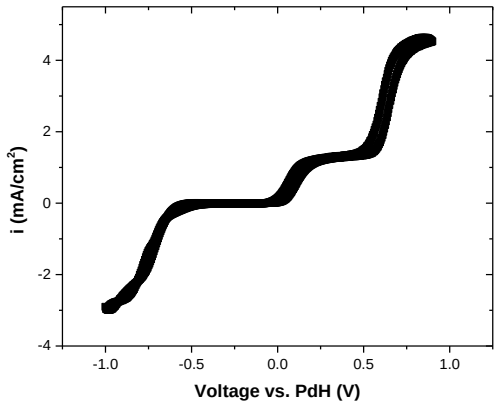


Figure 94. IR-correction of CV presented in Figure 93

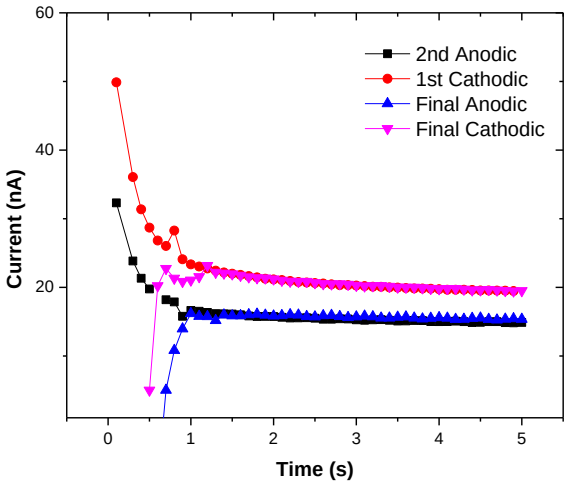


Figure 95. Background subtracted current response of first and last pulses from chromoamperometry experiments on PdH microelectrode. ±500mV pulses for 5 seconds each

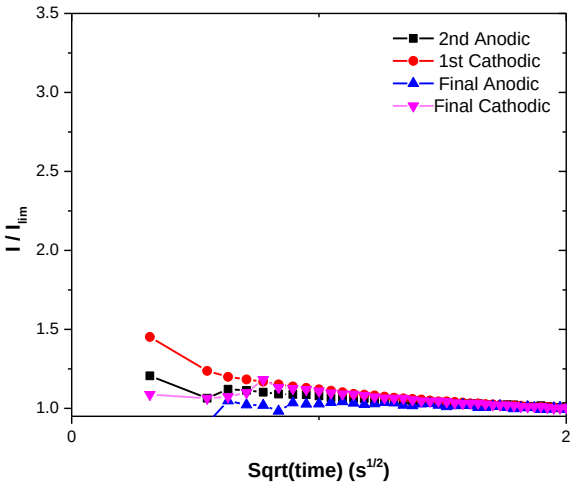


Figure 96. I/I_{limit} vs. $t^{1/2}$ for multistep chronoamperometry of PdH microelectrode to 10 ±500mV pulses for 5 seconds each. Only first and last pulses are shown*. I_{limit} was taken as current at $t=t_{max}$

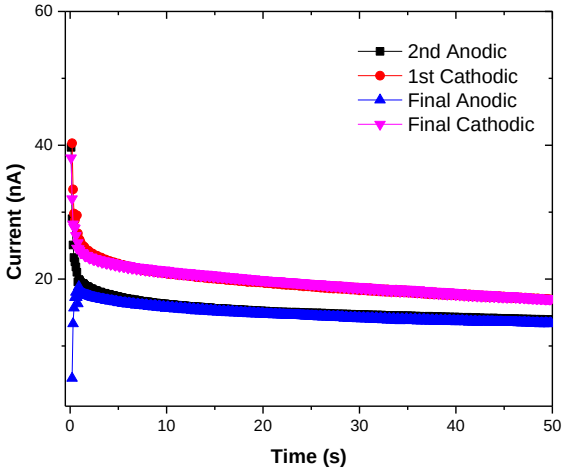


Figure 97. Background subtracted current response of first and last pulses from chromoamperometry experiments on PdH microelectrode. ±500mV pulses for 50 seconds each

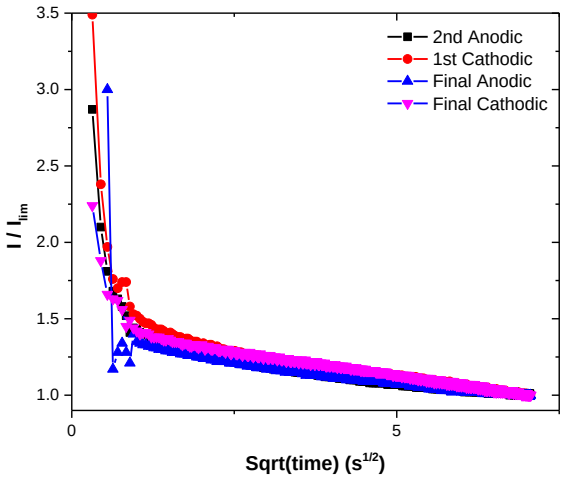


Figure 98. I/I_{limit} vs. $t^{1/2}$ for multistep chronoamperometry of PdH microelectrode to 10 ±500mV pulses for 50 seconds each. Only first and last pulses are shown*. I_{limit} was taken as current at $t=t_{max}$

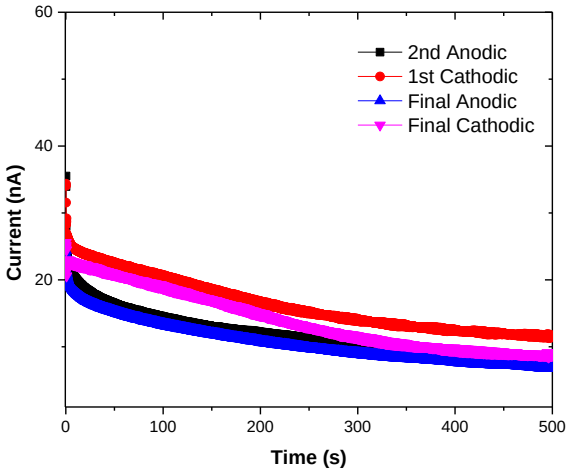


Figure 99. Background subtracted current response of first and last pulses from chromoamperometry experiments on PdH microelectrode. ±500mV pulses for 500 seconds each

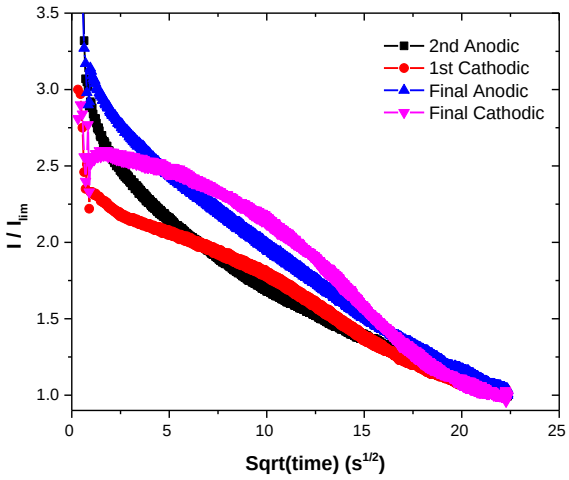


Figure 100. I/I_{limit} vs. $t^{1/2}$ for multistep chronoamperometry of PdH microelectrode to 10 ±500mV pulses for 500 seconds each. Only first and last pulses are shown*. I_{limit} was taken as current at $t=t_{max}$

Voltammetric Identification of Single Carboxylic Acid

After reducing the electrical resistivity of the nonpolar solutions and identifying a suitable reference electrode that operates in aprotic solvents such as crude, testing for identification of naphthenic acids can begin. The technique selected for identification of naphthenic acids was cyclic voltammetry. Cyclic voltammetry was selected due to its ability to scan a large voltage window and to identify the relative reactivity of the species in solution. In addition, if the identity of the species is known prior to experimentation, then the results can confirm or deny the presence of the species. In these experiments several carboxylic acids with structures representative of two classes of naphthenic acids were selected. The acids selected were benzoic acid, cyclohexane butyric, dodecanoic acid, and stearic acid.

The voltammetry experiments were performed to look for the reduction of hydrogen ions that area furnished to the surface from the acid molecules. Thus, the experiments started at a relatively oxidizing potential of 0V vs. PdH and then were scanned cathodically to -2V vs. PdH. The -2V end point was selected to avoid breakdown of the solvent and/or ionic liquid. Each experiment consisted of three scans, and the third scan was used for analysis. During the analysis, the background was subtracted using a linear fit in the region of -0.3Vto-0.5V vs. PdH, where no electrochemical reactions occur. The half wave potential was calculated using the potential at the arithmetic mean of the two plateau potentials. The resultant voltammograms for single acids can be found in Figure 101 -Figure 105.

Table 16 contains the compiled results from the experiments. Benzoic acid was the most difficult to reduce followed by stearic, dodecanoic, cyclohexane acetic, and finally cyclohexane butyric. Although the electrochemical reduction of each of these acids displays gross irreversibility, the half wave potential was still extracted using the standard convention. It should be noted that since these voltammetry experiments utilize

UMEs, the current response appears as a step, rather than two distinct peaks. The reason for the single sigmoidal shaped peak is due to the rapid radial diffusion of the UME, which rapidly transports products away from the surface.(Aoki 1993) Thus, in the voltammograms below, the current response is associated with the reduction of the hydrogen ion on the electrode surface.

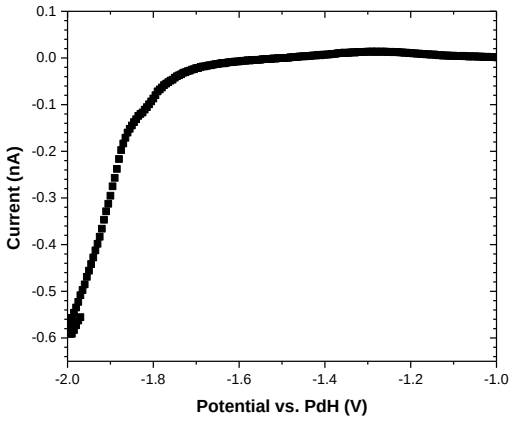


Figure 101. Voltammogram of 0.5 mM benzoic acid in 0.3M $P_{6,6,14}$[TKIS] in toluene after background subtraction

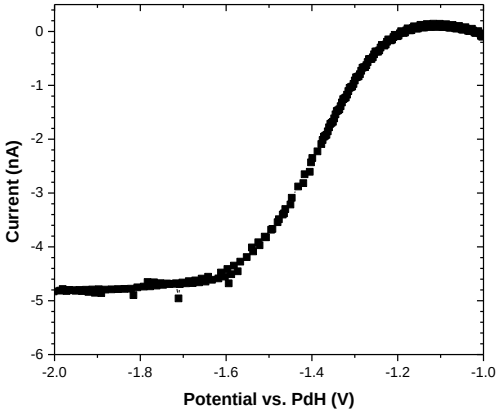


Figure 102. Voltammogram of 0.5mM cyclohexaneacetic acid in 0.3M $P_{6,6,14}$[TKIS] in toluene after background subtraction

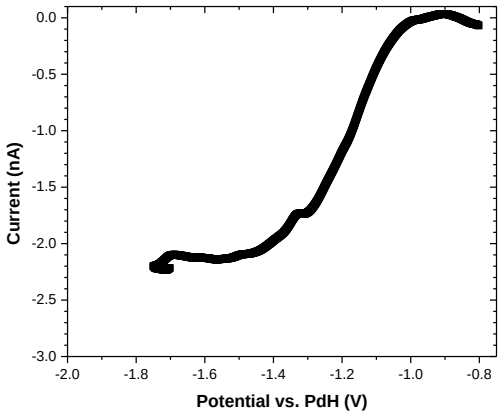


Figure 103. Voltammogram of 0.5mM cyclohexanebutyric acid in 0.3M $P_{6,6,14}$[TKIS] in toluene after background subtraction

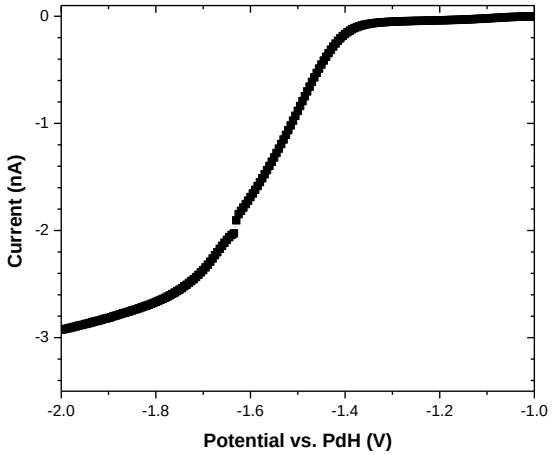


Figure 104. Voltammogram of 0.5mM dodecanoic acid in 0.3M $P_{6,6,14}$[TKIS] in toluene

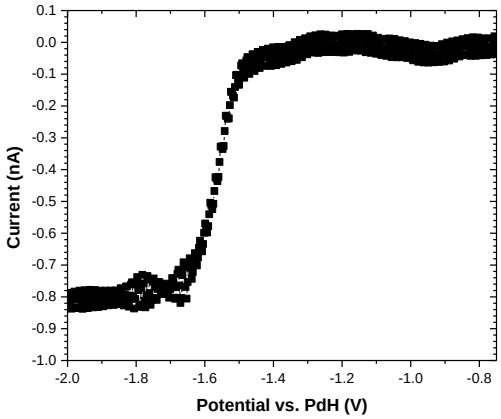


Figure 105. Voltammogram of 0.1mM stearic acid in 0.3M $P_{6,6,14}$[TKIS] in toluene

Acid	E1/2 (V)	Molecular Weight (g/mol)	BP (°C)	Carbon #
Cyclohexanebutyric	-1.18	170	270	10
Cyclohexaneacetic	-1.38	142	244	8
Dodecanoic	-1.55	200	300	12
Stearic	-1.56	284	383	18
Benzoic	-2.00	122	249	7

Table 16. Summarized Results of Voltammetry of Single Acids. Pt UME Working Electrode. PdH CE/RE. Solution 0.3M $P_{6,6,14}$[TKIS] in toluene, 0.5mM acid concentration

Discussion

Raman and FT-IR Study of Structure of Acids in Solution

Introduction

Raman spectroscopy is a powerful tool for investigating bonding interactions between molecules via the observation of molecular vibrations. The sensitivity of the technique stems from the fact that each functional group is recognized by its well-defined range of vibration wavelengths. Additionally, Raman spectroscopy does not require any dipole changes in the molecule; simply a change in the polarizability of a bond can result in a Raman scattering peak that provides valuable bonding information. This is an especially attractive feature for analyzing petroleum compounds as the components of interest in crudes viz. the naphthenic acids, are inherently of low polarity.(Tooke et al. n.d.) By resolving a few drawbacks such as interference from fluorescence and weak signal intensity, Raman spectroscopy has become a very attractive technique for studying bonding interactions in petroleum based compounds.(Ahmadjian & Brown 1976) For these reasons, Raman spectroscopy has been utilized to observe various carboxylic acids as well as studying oil spills.(Ahmadjian & Brown 1976; Sunder et al. 1976; Gelder et al. 2007; Nakabayashi & Nishi 2002) But, to the best of my knowledge, it has not been used to systematically study the mechanism of corrosion in crudes at elevated temperatures.

Here, Raman spectroscopic is used to study of the breakup of naphthenic acid dimers to its monomers as the temperature is increased. The shift with temperature to the monomer configuration may account for the high temperature needed to initiate naphthenic acid corrosion. These studies also show that the concentration of acid monomers increases as a function of dilution, in agreement with the observations reported by Rodgers, Marshall and co-workers.(Smith et al. 2007) Additional experiments were performed to investigate the role of the metal in the multimer to monomer breakdown process and the subsequent corrosion reaction that forms metal naphthenate complexes. Following the temperature dependent multimer breakdown with both micro Raman and FT-IR spectroscopies has helped in proposing a plausible mechanism of corrosion in the refineries.

The investigations into the mechanism of naphthenic acid attack on iron were initiated assuming that the dimers or multimers of acids that normally exist at ambient temperatures will break apart into their corresponding monomers as the temperature is increased (

Figure 106). These monomer units now have a free acid group readily available to react with the iron in carbon steel, forming soluble corrosion products. Systematic studies performed over a range of carboxylic acids belonging to the naphthenic acid group, both neat and as mixtures in mineral oil, form the basis for depicting the mechanism of corrosion in crudes.

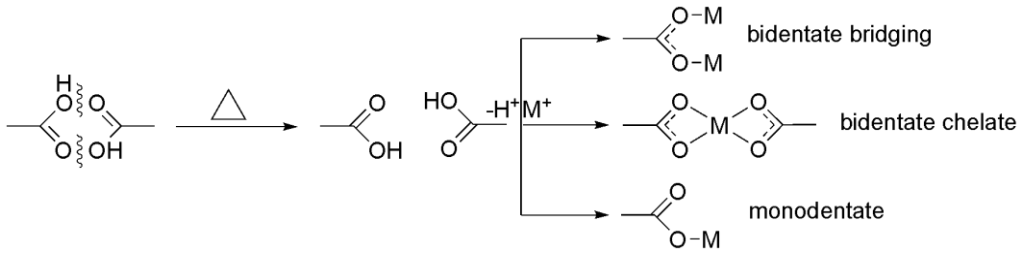


Figure 106. Schematic representation of the probable mechanistic pathways, forming different soluble corrosion products. . (Chakravarti et al. 2013) Reprinted with permission from Energy and Fuels. Copyright 2013 American Chemical Society

High Temperature MicroRaman study of individual carboxylic acids in their neat form.

As a starting point of the naphthenic acid study, the spectral behavior of the very simple carboxylic acid, *n*-propionic acid, was observed. In addition to the simplicity, the availability of literature reports on the vibrational spectral studies of this molecule also made this an obvious choice to form an appropriate baseline to start this study.(Holowenko et al. 2001) The various molecular species that constitute a neat acid at any given temperature are shown in

Figure 107.(Bohle et al. 2002)

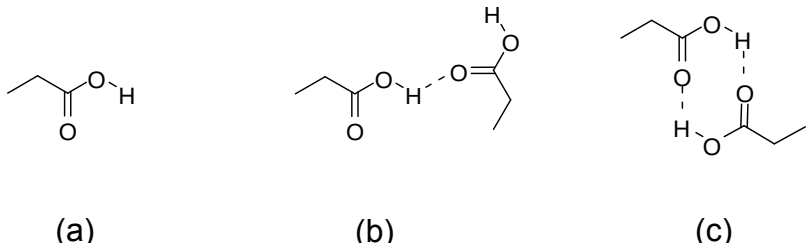


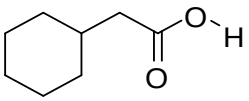
Figure 107. Schematic of the (a) monomer, (b) linear dimer/multimer, and (c) cyclic dimer configurations. . (Chakravarti et al. 2013) Reprinted with permission from Energy and Fuels. Copyright 2013 American Chemical Society

From the earlier literature reports, it is known that in the Raman spectra of the aliphatic carboxylic acids, the symmetric C=O stretching band occurs between 1640-1685 cm^{-1} for dimers which shifts to about 1705-1710 cm^{-1} for monomers.(Socrates 2004) According to Ise and co-workers, there are two different associated species present i.e. cyclic dimers which have the lowest Raman shift values (1640-1660 cm^{-1}) and linear dimer/polymer which has higher Raman shift values (1675-1690 cm^{-1}) compared to the cyclic dimers and the monomers have the highest stretching frequency (1705-1720 cm^{-1}) among the three.(Tanaka et al. 1991) Carboxylic acids exist as stable dimers in neat form at ambient temperature. The carboxylic acid dimers tend to break up into monomers when either heated to higher temperatures or diluted by a non-polar solvent or both. But unlike the observations reported by Koteswaram these experiments show a steady breakdown to monomers with dilution by a non-polar solvent, this again is supported by

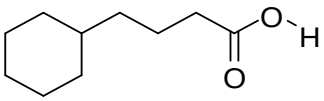
the observation reported by Socrates.(Socrates 2004; Koteswaram 1939) Raman spectra of propionic acid at various temperatures in the spectral region of interest have been furnished in the supporting information. Peak positions of the observed Raman bands compared with earlier literature reports show a close agreement.(Czarnecki 2003; Ng & Shurvell 1987) The estimated error margin for well-developed peaks is ± 1 cm^{-1}, while for shoulders and diffuse bands it is approximately ± 5 cm^{-1}. The peak positions of the spectrum at 80°C showed no detectable shift of any bands, though a small reduction in intensity was observed and thought to be a result of rapid vaporization of the sample nearing its boiling point. Shown in previous reports (add references), Raman bands for C=O stretching modes are inherently weaker than their IR counterparts. The smaller Raman cross-section arises from the fact that Raman scattering depends on polarizability of the bond, while IR absorption depends on the dipole moment of the bond. On the other hand, in spite of its inherently weaker response, Raman intensity is directly related to the concentration of a species, providing unique information.(Pham et al. 2013) Relative concentrations of each molecular species at each step and the progressive growth of the monomer with temperature at the expense of the multimers are given in the supporting information. In addition to the propionic acid, the concentration shift from multimer to monomer was studied in a few other simple carboxylic acids that fall under the generic formula of $C_n H_{2n+Z} O_2$ and are suspected to be present in the more complex naphthenic acid mixtures as suggested by the studies of Hsu et al. in their ^{13}C NMR experiments.(Hsu et al. 2000; Fu et al. 2006) The acids chosen contained an alicyclic ring attached to either the carbonyl group or to an aliphatic chain containing the carboxylic group (Figure 108). The microRaman spectra of these acids consistently showed the presence of peaks for the C=O stretch region between 1655-1710 cm^{-1}, in line with the earlier reported values.(Ng & Shurvell 1987) According to the previous researchers, even though the cyclic dimers are the most stable association of the monomers, a linear dimer or polymer species consisting of a chain formed by linear association of the monomers can also exist. Because the C=O peaks corresponding to the dimer, multimer, and monomer species have very similar Raman shift values, bands overlap and only one, multicomponent peak is seen in the raw data displayed in Figure 19. The three individual peaks must be properly resolved to see how each varies with temperature and to find out their relative concentrations (e.g., Figure 20). Peak deconvolution has been done with help of commercial software and all the fittings have been found to converge. The reduced chi-square values are found to be within the acceptable range, being aware of the fact that it can only be used for non-linear systems with caution. Moreover, the random noise in the data creeping in by the faintest exposure to visible light, change in molecular motion at high temperature and slow depletion of sample quantity with the rise of temperatures have introduced a small degree of uncertainty. But despite this, the trends of the changes of molecular dissociation as a function of temperature are clear from the experiments. The C=O peak appears as a series of broad peaks between 1665-1710 cm^{-1} wavenumbers. Resolution of the overlapping bands for various species (Figure 20) provides the relative concentrations (

Table 3), which show a continuous and considerable increase of the monomeric species at the cost of the multimers as temperature increases. This increase in concentration may be attributed to the breakup of long-range non-covalent hydrogen bonding between the molecules expected at higher temperatures, especially in a non-polar

solvent.(Seifert & Teeter 1970) It may be mentioned here that there are other factor such as velocity, turbulence, etc. known to affect corrosion in the refineries and these are not studied in this current work, as the aim was to study the changes taking place at the molecular level in the bulk of the naphthenic crudes.



Cyclohexane acetic acid



Cyclohexane butyric acid

Figure 108. Structures of typical NAs studied, where z= -2. . (Chakravarti et al. 2013) Reprinted with permission from Energy and Fuels. Copyright 2013 American Chemical Society

In these experiments, it appears that the usual phenomenon of increasing corrosion as a function of temperature is observed, as increase of temperature eventually provides enough thermal energy to dissociate many of the dimers into the corresponding monomers of the acid, thereby increasing the population of the reactive monomer species, which are eligible to bind with the metal owing to their free acid group. It is a well-known fact that the components in naphthenic acids have a vast distribution of molecular weight and size, which again is critical to adsorption, the starting process of the formation of metal naphthenates. Temperature also affects adsorption, which may be another factor along with the dimer breakdown in governing the corrosion process. Studies on the fate of the acid molecules on the surface are being pursued in the Devine lab currently by surface enhanced Raman techniques.

While the decrease in cyclic dimers and increase in monomers occurs monotonically,

Table 3 and

Figure 21 demonstrate the proportion of linear dimers initially increases before decreasing. The ratios of the molecular configurations forming in each step are compared to the cyclic dimer, which forms the bulk of the population of the molecular species at room temperature. This trend is consistent with the linear dimer being an intermediate species in the stepwise breakdown of the cyclic dimer to monomer. In this way, the initial increase consists of the cyclic configuration converting to linear, while the subsequent decrease reflects the linear dimer splitting to monomer. Thus, by looking at the slope of the line denoting monomer/cyclic in

Figure 21 it is suggested that the number of dimers breaking down into monomers is much higher at higher temperatures. It therefore appears that the progression follows a stepwise pattern of the non-covalent hydrogen bonds breaking at high temperature, resulting in a high concentration of monomeric species available for the onset of corrosion reaction that forms oil soluble metal-ligand complexes. Similar behaviors were observed in case of the other acids studied. In order to relate the structural change of an acid to its acidity, the behavior of stearic acid (data not shown here), a long chain acid was observed in the same way. It can be mentioned here that a similar behavior was

noticed in this case even though at a little higher temperature. Therefore it can be concluded that the basic mechanistic pathway is similar in all the carboxylic acids.

High Temperature MicroRaman study of naphthenic acid mixtures in neat form.

Similar to the observations reported above for the individual acids, the activated carbon treated naphthenic acid mixture showed C=O stretching bands of medium intensity in the same characteristic spectral region, as shown in Figure 22.
To deconvolute the spectra to give the relative concentrations of the various molecular species, it was assumed that all the C=O moieties present in the mixture belong to the same carboxylic acid group and each molecule of acid contains only a single carboxylic group. At higher temperatures, the neat acid mixture became intensely colored, giving rise to a huge background from fluorescence in the visible region. However, with careful baseline correction followed by band resolution, the relative concentrations of the various species were properly revealed, again showing a gradual increase in monomeric species (Figure 23). Changes of the relative concentration of monomer and multimer are only apparent after deconvoluting this peak (See Figure 23).

It is evident from Figure 23 that the relative concentration of the monomer increases with temperature in a similar manner to the other acids studied. It should be noted here that commercial naphthenic acid, being a mixture of several lower and higher molecular weight acids has a comparatively bigger temperature range of breakdown into linear dimers and subsequently into monomers. The temperature ranges that the experiments were conducted over could only see the sequential breakdown of the lower molecular weight acids. The higher molecular weight acids, having higher boiling points most probably breakdown to an extent, making the concentration of the linear dimer go up at some temperatures. This may explain the sudden rise of the concentration of the linear dimer at higher temperatures during the course of the experiment. Combining this result with the observation of Dettman and co-workers that carboxylic groups begin to decompose above 400^0C, a hypothesis for the temperature range of naphthenic acid corrosion can be outlined.(Dettman et al. 2009) At lower temperatures, acids are in the multimeric configuration and less available for the corrosion reaction, which has a high activation energy. At some critical temperature, thermal energy is sufficient to overcome the activation barrier of corrosion at the same time the monomer concentration increases sufficiently to initiate corrosion. The rate of the corrosion reaction increases until the point where the acid decomposition reaction dominates, creating a range of approximately 220°C – 400°C where corrosion is most active.

Table 4 and Figure 24 depict the relative change of the various molecular species in neat naphthenic acid mixtures as a function of temperature. The same trend of gradual increase of the monomer with the rise of temperature is clearly seen here. From above, it can be seen that an approximate gradual increase of the monomer is taking place at the cost of the self-associated species, and it can reasonably said that the process takes place in a stepwise fashion finally resulting in high concentration of monomers.

High temperature MicroRaman study of naphthenic acid mixtures dissolved in mineral oil.

The main objective of this study is to investigate the molecular association/dissociation of the naphthenic acid molecules and to consider its effect on corrosion of iron at high temperatures. It thus becomes relevant to extend the scope of the study from behavior of naphthenic acid in the neat liquid to the behavior of acids in solution with mineral oil, as this model system would be appropriate to render an idea of the actual process in the crudes. Rodgers, Marshall, and co-workers have shown the molecular association and the presence of various molecular species in solution are remarkably different from those in the neat acid, where there exists a critical concentration only above which molecular self-association initiates.(Smith et al. 2009) Similar observations were also reported by Nishi and coworkers in case of acetic acid in solution.(Nakabayashi & Nishi 2002) This indicates that the chemical nature of the other participating components are the deciding factor for the behavior of the acid moieties.

In order to study the differences in the molecular association of acids and their hydrogen bond co-operativity in solutions with mineral oil compared to those in the neat acid microRaman experiments were performed on acid mixtures in mineral oil with varied amounts of naphthenic acid. Stepping down in concentration from the 100% neat acid solutions, the solutions cover a range from 80% to 20% naphthenic acid. Decreasing the concentration past 20% approaches the detection limit of the microRaman system, so more dilute concentrations were not studied. Band resolved room temperature spectra from three concentrations are shown in

Figure 25.

Figure 25 shows that the behavior of a highly concentrated 80% naphthenic acid mixture of mineral oil exhibits similar behavior to that of the neat acid, showing high concentration of cyclic dimers and low concentration of monomers at low temperature. As concentration decreases, a different behavior emerges. Owing to the non-polar nature of mineral oil, self-association of naphthenic acid molecules is disrupted at higher dilution to maintain an identical concentration gradient of the components of the mixture throughout the solution. Forces of diffusion are active until equal distribution of all components is achieved, creating a homogeneous mixture. The observation that concentration affects the molecular association-dissociation is well supported by various literature reports.(Smith et al. 2009; Nakabayashi & Nishi 2002) A very similar trend as result of dilution is observed in these experiments in case of

Figure 25 spectra (2) and (3).

Molecular association in petroleum crudes has been of interest to many research groups and has been well documented in the recent years.(Fu et al. 2006) Hydrogen bonding interactions have been found to be the key forces associating the molecules of carboxylic acid in a mixture, with the molecular association-dissociation processes taking place in stepwise manner rather than the miceller aggregation pathway.(Ng & Shurvell 1987) As with the neat acids, the phenomenon of stepwise breakdown is seen in these microRaman spectra of acid mixtures at high temperature. Table 5 and Figure 26 show the distribution of the molecular species of the acid at various temperatures for the 20% concentration.

Again, as has been stated before, a temperature of 180°C is not high enough to disassociate all the acids dimers present in the commercial naphthenic acid mixture. Therefore some acid species present in the mixture are in the first step of their breakdown by forming the linear dimers, which have a higher concentration at this temperature. The above examples and the overall trend shown by the single acids indicate that the plausible mechanism of breakdown is stepwise as the concentration of the linear dimer increases at the cost of the cyclic dimer at 180°C and the concentration of the monomer increases progressively from room temperature to higher temperatures. It may also be stated here that naphthenic acids in binary solutions had been found to have a relatively higher concentration of monomer than in its neat state. This may be attributed to the fact that mineral oil being non-polar cannot support hydrogen bond formation between oil and naphthenic acid molecules and at high dilutions the distance between monomers being generally greater than the threshold distance for hydrogen bond formation, acid monomers are present in larger numbers. But the stability of the cyclic dimer makes it possible for it to be present at a considerable concentration even though the proportion is much lower than that in the neat.(Nakabayashi & Nishi 2002) It has been observed that even then the dimer breakdown process as a function of temperature is prevalent in the binary mixtures studied. Thus, it was observed that the cyclic dimers break down into monomers in a stepwise manner with increasing temperatures. It may be noted that the naphthenic acid concentration studied here is much higher than typically present in crudes, but dimer dissociation with increasing temperature is expected to occur in crudes having much lower concentration of acids than the lab simulated crudes.

MicroRaman and FT-IR spectroscopic study of a binary mixture of 20% naphthenic acid in mineral oil in the presence of metals

Iron powder test has been employed by Hau, Yepez, Specht and Loranzo for the measurement of corrosion by estimation of dissolved iron in the reaction mixture.(Hau et al. 1999) In the present work iron powder has been used to understand the dissociation behavior of the acid dimers in the presence of metal surfaces. The formation of metal naphthenate salt was investigated using the 20% naphthenic acid mixture. The 20% solution was heated to 200°C, under stirring, in presence of a series of finely divided metal powders, including iron, copper, and zinc, for 2 and 3 hours. This is a much longer duration than the previous studies done without metal (10 minutes) in order to give time for the acids to react with the powders. After 3 hours, the relative concentration of the monomer reached 60% in the presence of iron, a much larger fraction than that seen in the absence of iron.

Figure 27(curve fitted C=O region) and

Table 6 give the corresponding concentrations of the respective molecular species for samples taken at 2 and 3 hours. This notable increase in the concentration of the monomers in presence of iron can be attributed to the fact that the above-mentioned metals have high affinity to form carboxyl complexes with acidic ligands and thus the reactive monomers are converted into complexes after they are formed in the solution.(Mehrota & Bohra 1983) This, coupled with the fact that the elevated temperatures facilitate the complexation process, helps in the formation of more and more monomers in the presence of metals, which then goes into reaction with the metal

centers, forming naphthenate complexes. It may be mentioned here that the iron naphthenate formed here is dark brown in color, which gradually makes the solution very dark, rendering it unfit to be analyzed by 632.8 nm line of a He-Ne laser, which was utilized in this work.

To complement the high temperature microRaman studies, the above mentioned reaction forming soluble metal naphthenate salts of iron, zinc, and copper has been followed by FT-IR spectroscopy(Figure 28). The heterogeneity of the carboxyl metal bond makes it highly sensitive to infrared absorption, making FT-IR a powerful tool for studying metal ligand binding.(Ng & Shurvell 1987) FT-IR spectral measurements have been carried out on the reaction mixture simultaneously with the Raman experiments, but iron carboxylate peak in FT-IR spectra became visible only after the reaction was conducted for a considerable amount of time, when the color deepened visibly. Figure 109 depicts the time dependence of the decrease of acid, which is associated with the formation of Fe-naphthenate. The samples collected after times ≥ 4h showed considerable darkening of color and an intense band of the carboxylate moiety at 1585 cm^{-1}.

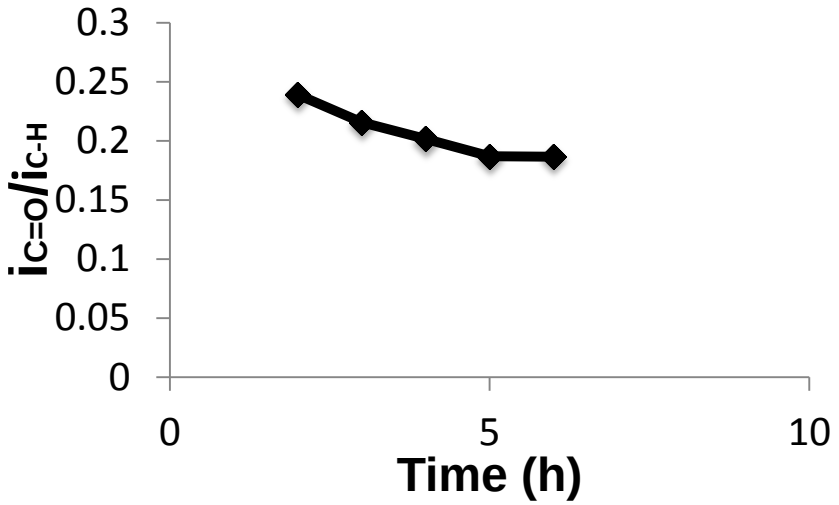


Figure 109. Time dependence of Fe-naphthenate formation[a]. (Chakravarti et al. 2013) Reprinted with permission from Energy and Fuels. Copyright 2013 American Chemical Society

[a]iC=O/ iC-H denotes the ratios between the intensity of the peak resulting due to the stretching vibration of the carboxylic acid (iC=O) to the intensity of stretching of the C-H bond(iC-H). The reason for considering the ratio is that the concentration of C-H moiety is already very high in the solution and therefore can be considered almost constant and is a very strong peak appearing in the IR spectrum similar to the C=O stretch peak.

Earlier reports on metal carboxylate binding shows four distinct patterns of behavior for the carboxylate ligand, which is well supported by crystallographic studies, *viz*. ionic, bidentate chelating, bidentate bridging and unidentate.(Marshall & Rodgers 2004) The first three structures show certain resemblance to each other in their IR spectra; however, all three differ markedly from those of the unidentate carboxylates. The characteristic bands of metal carboxylates include a strong asymmetric CO_2 stretching vibration (i.e. δCO_{asym}) and a somewhat weaker symmetric CO_2 stretching vibration (i.e. δCO_{sym}); the bands corresponding to the coordinated modes (

Figure 106) are situated at different frequencies relative to values for the free carboxylate ion (

Figure 106) that are usually measured for sodium or potassium salts of the corresponding carboxylic acid.(Mehrota & Bohra 1983) The frequencies of the bands are highly sensitive to the structure of the carboxylate group, the nature of the solvent, the nature of the ligand and the identity of the metal ion, therefore, the separation of the bands (i.e. $\Delta=CO_{asym}-CO_{sym}$) is also indicative of the structure of a given carboxylate.(Dresseyn 1992)

Ionic carboxylates exhibit two bands (δCO_{asym} and δCO_{sym}) in their IR spectra; the first band appears as a very strong but generally broad band while the second band is less intense.(Mehrota & Bohra 1983; Colthup et al. 1990) Palacios et al. have shown that in case of versatate anion, the free carboxylate has stretching vibrations for νCO_{2asym} at 1530 cm^{-1} and νCO_{2sym} at 1470 cm^{-1} , with values of the separation between the νCO_{2asym} and νCO_{2sym} , following the general trend of: uncoordinated acid > unidentate coordination > bi-dentate coordination (bridging>chelating) > free carboxylate ion.(Palacios et al. 2004) Aliquots of the binary mixture after 5h of stirring at 200°C contained dissolved metal naphthenates (brown in color in case of Fe-naphthenate), which were then subjected to FT-IR studies. The FT-IR spectra are presented in Figure 28. A close observation of the spectra taken after 5h at 200°C reveals the disappearance and the growth of some characteristic peaks and indicates the formation of soluble metal naphthenates (Figure 28).

Consider first the changes in the IR spectrum of the binary 20% naphthenic acid solution exposed to iron powder. IR spectra were measured following exposures to iron powder for times of 2h, 3h, 4h, and 5h. The spectrum obtained after 5h is presented in Figure 28. The peak at 1700 cm^{-1} belonging to C=O of naphthenic acid was found to slowly decrease in intensity over the 5h time period indicating consumption of acid molecules in forming the Fe-naphthenate complex. The appearance and subsequent growth of the peaks at 1585cm^{-1} and 1409 cm^{-1}, which can be attributed to νCO_{2asym} and νCO_{2sym}, respectively definitively proves the formation of some type of naphthenate complex. Owing to the inherently low polarity of naphthenic acid molecules, the formation of an ionic carboxylate complex is ruled out.(Palacios et al. 2004) Therefore, only a unidentate or a bidentate (chelate/bridging) mode of binding is possible. The difference of 176 cm^{-1} between the above mentioned peaks suggest the formation of a bidentate complex.

A progressive decrease in intensity over the 5h time span was observed for the C-O stretch at 1260 cm^{-1}. The O-H…O deformation peak at 1298 cm^{-1}, which is a characteristic vibrational feature of dimeric acid, steadily decreased in intensity over the 5h reaction time indicating dimer breakdown in the acids. Another notable peak, which exhibited a steady increase over the reaction time, is the O-H deformation band of acid monomer, at 1376 cm^{-1}, which has indicated the formation of acid monomers from the dimers during the course of the reaction. Figure 109 shows the time dependent decrease of carboxylic acid concentration.

Collectively the IR spectra obtained as a function of time of exposure to iron powder at 200°C indicates that the acid dimers in the 20% naphthenic acid binary mixture are broken down into their corresponding monomers, which react with iron to form the soluble corrosion product, which is a bidentate Fe naphthenate.
In order to ensure and establish the mechanism of reaction taking place during the formation of Fe naphthenate, the above results have been compared with results of similar tests conducted with Zn, which is found to have reacted in a similar fashion in forming carboxylate complexes in literature reports.(Palacios et al. 2004; Ryde 1999) The same reaction procedure has been conducted and the IR spectra were measured as a function of time of exposure to finely divided Zn powder (Figure 28). A similar set of peaks appeared and developed over the 5h given time period was seen in case of Fe. The spectrum measured after 5h exposure to Zn is presented in Figure 28. A peak at 1626 cm^{-1}, which was not seen in Fe naphthenate, was observed in the case of Zn naphthenate at 1626 cm^{-1}. This peak is comparatively closer to the C=O stretching vibration in an acid and might be attributed to extensive solvation of the monomers, which would cause a downshift of the bands. However, the low polarity of mineral oil rules out any possibilities of a solvation effect. Therefore the peak at 1626 cm^{-1} is best attributed to a unidentate metal ligand-binding mode. This peak assignment is supported by an earlier study, which reported zinc undergoing unidentate binding.(Dresseyn 1992) Thus, the results suggest that the unidentate zinc ligand is the result of a side reaction occurring parallel to the bidentate zinc ligand. It has also been shown by DFT studies of Zn carboxylate complex that both the unidentate and the bidentate mode of binding is almost the same energetically and the energy barrier for inter-conversion between the two binding modes is very small. This can be explained by the fact that the ‘d’ and ‘s’ orbitals in Zn have the same energies, with the filled ‘d’ shell in Zn encouraging an unidentate binding mode for some complexes. Figure 28 also shows the FT-IR spectrum of the 20% naphthenic acid binary solution following 5h of exposure to Cu powder at 200°C. The spectrum shows all of the peaks stated above for the Fe-naphthenate and Zn naphthenate complexes, but the locations of νCO_{2asym} and νCO_{2sym} for the Cu naphthenate complex are different and are located at 1608cm^{-1} and 1409 cm^{-1} respectively.

This peak pattern of the copper carboxylate moiety can be assigned to a bridging, binuclear binding mode common in case of copper carboxylate complexes.(Abuhijleh 1994) The greater value of $\Delta\nu$ of Cu compared to Fe or Zn naphthenate makes the bridging binuclear binding more likely. Because of the polarity of naphthenic acid, there is no possibility of any ionic bond formation. The metal ligand reaction thus proceeds to form unidentate, bidentate chelate, or a bidentate bridging complex. Such a spread of complexes can be formed only when the non-reactive acid dimers at elevated temperatures are broken down into their monomers, which in turn react with the metal to form soluble metal naphthenate complexes.

Microgravimetry

To perform in-situ corrosion experiments with time resolution, a technique capable of measuring small mass changes was needed. As naphthenic acid corrosion rates are often on the order of 1-5 mm/yr, a back of the envelope calculation gives the required resolution of the technique. For a 1 mm/yr corrosion rate on a sample of 1 cm^2

area, only 0.08 mg of material is lost over the period of an hour. Thus, to perform experiments that could measure corrosion kinetics at the start of the corrosion process in a timely manner, a technique with a mass resolution better than 10^{-5} g/cm^2 was needed. The technique selected to accomplish the task of measuring time resolved corrosion rates was crystal microbalance. The crystal microbalance technique utilizes changes in the resonant frequency of a piezoelectric crystal to calculate changes in mass loading on the surface of the crystal. The resolution of a microbalance is approximately 10^{-9} g / cm^2 which greatly exceeds the requirements.(Stienhem & Janshoff 2006) In addition, as the crystal and sample holder are made out of corrosion resistant materials, there is no extraneous corrosion caused by exposing the holder to the test solution.

Introduction to Theory

The crystal microbalance technique utilizes piezoelectric resonators to measure very small mass changes. Piezoelectric materials have a unique property due to the lack of centro-symmetry present in the crystal structure. Upon the application of a strain to the lattice, an electric field is generated. The piezoelectric phenomenon can most easily be understood by looking at a 2d set of ions in a hexagonal arrangement (

Figure 110). The hexangonal 2d lattice structure has a center of charge located at the center of the hexagon when unstrained. However, upon compression of the hexagon from the top and bottom (

Figure 110 right), the symmetry is broken, and the center of charge for the cations and anions are no longer in the same position. The separation of charge creates an electric dipole, which in-turn produces an electric field. The converse of piezoelectric phenomenon also occurs, meaning that upon application of an electric field or voltage across the crystal, the lattice will strain.

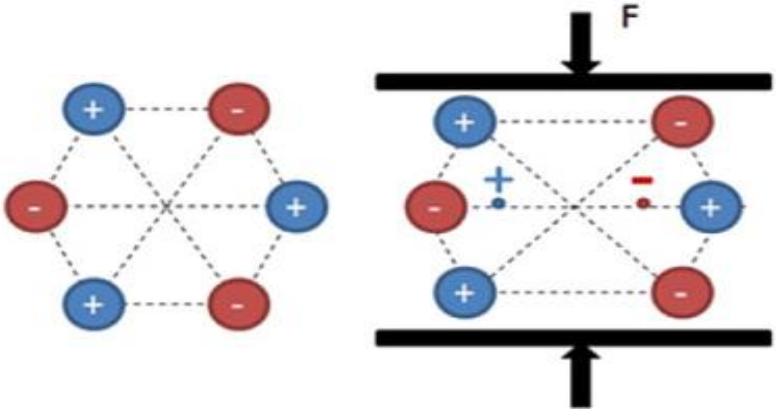


Figure 110. 2d representation showing dipole production from piezoelectric effect.(Ramadan et al. 2014)

The requirement for piezoelectric behavior is that the lattice is non-centrosymmetric. The symmetry governing piezoelectricity is the point group of the crystal, and out of the 32 lattice point groups, 20 have the possibility of being piezoelectric.(Morris n.d.) For crystals that are piezoelectric, the structures are high anisotropic, and certain crystallographic directions display more strain or higher electric

fields.(Stienhem & Janshoff 2006) The anisotropic behavior of a piezoelectric can be controlled using thin flat crystals with conducting electrodes on both sides of the crystal. If a voltage difference is applied between the two electrodes, an electric field is generated, and the piezoelectric material is strained. By judicious choice of the crystal orientation, the direction of the strain can be controlled.(Stienhem & Janshoff 2006) Now, if the electric field is applied sinusoidally such as in an AC waveform, then the strain becomes a vibration, and resonance can be established in the crystal. The application high frequency square waveform AC voltage is in essence how a microbalance functions. A simplified diagram showing how a microbalance functions in practice is shown in
Figure 111.

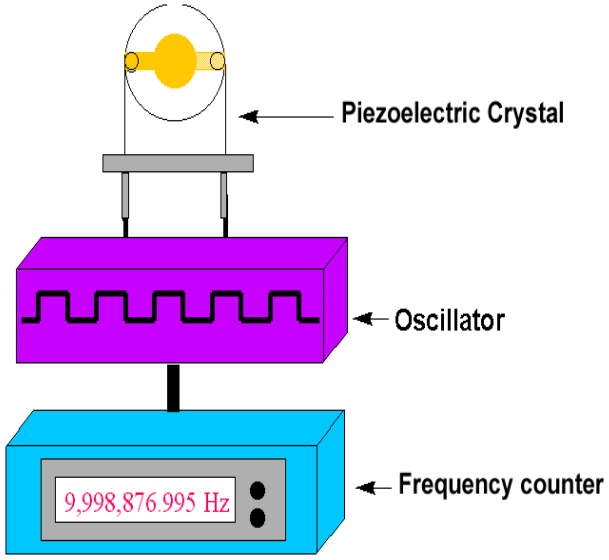


Figure 111. Simplified schematic of crystal microbalance experimental setup(Kumar 2000)

While the vibrations induced in the piezoelectric create a mechanical resonance, the resonant frequency is not governed purely by the moment of inertia, as the crystal must be supported by the sample holder, and there is internal friction within the crystal.(Stienhem & Janshoff 2006) Once resonance is established, if a mass is added or subtracted from the surface uniformly, then the change in resonant frequency can be used to calculate the change in mass areal loading. The effect of mass loading on the frequency of a piezoelectric crystal is shown in Figure 112, where the frequency of a loaded crystal decreases compared to an unloaded crystal.

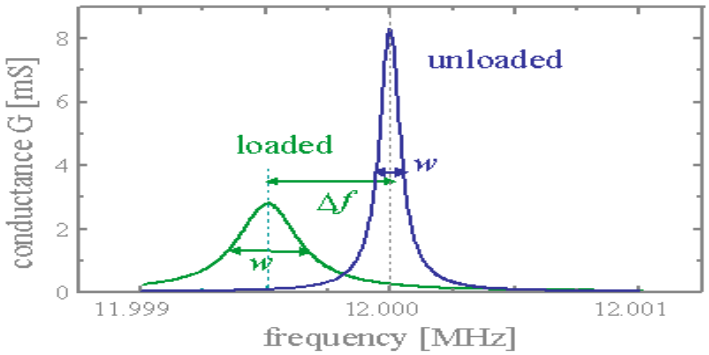


Figure 112. Conductance vs. frequency for crystal microbalance upon loading. (A. Langhoff)

The relationship to relate frequency shift and mass loading was first realized by Sauerbrey, who developed the Sauerbrey equation (Sauerbrey 1959). The Sauerbrey equation is shown in *equation 3*.

$$\Delta f = \frac{\Delta m f_0^2}{A\sqrt{\rho_P G_P}} \qquad \{3\}$$

Δf is the frequency shift (Hz), Δm is the mass loading on the crystal for the given frequency shift (kg), f_0 is the fundamental frequency of the crystal (Hz), A is the piezoelectrically active area (m^2), ρ_P is the density of the piezoelectric (kg/m^3), and G_P is the shear modulus of the piezoelectric material (Pa). The Sauerbrey equation holds at relatively small mass loading, below approximately 1-2% of the fundamental resonant frequency of the crystal.(Sauerbrey 1959) Later work done by Lu and Lewis allowed for accurate measurements with thicker films, which have mass loadings beyond the small mass loading region (Lu & Lewis 1972). Lu and Lewis's modification of the Sauerbrey equation addresses deviations for thick and/or lossy films, which have nonmatching acoustic impedances, and thus do not behave ideally.

Typically silica, SiO_2, is used as the piezoelectric material of choice in microbalances. SiO_2 is a trigonal crystal (point group 32), has a high mass sensitivity and is readily available in large high quality single crystals. In addition, the piezoelectric properties of an α-cut SiO_2 crystal remain relatively constant over the temperature range of 0-100°C.(Bechmann 1956) The change in frequency with a change in temperature arises from thermal expansion. As the temperature rises, the dimensions of the crystal, density, shear modulus, and atomic positions all change slightly. The combination of all of these contributions simultaneously causes the resonant frequency of the crystal to change. Above 100°C small changes in temperature cause large changes in frequency of a quartz resonator. The high sensitivity of frequency to temperature is important because during an experiment small temperature fluctuations are unavoidable and can induce large amounts of noise in the data. In addition to the effect of temperature on the resonant frequency, SiO_2 crystals twin at 300-350°C, which prevents its use as a resonator above 300°C.(Zhang & Yu 2011) To avoid the challenges that quartz presents, the microbalance experiments utilize gallium orthophosphate crystals.(Krempl 1997) GAPO is isomorphic of quartz, and shares many physiochemical properties.

The primary reasons that GAPO is superior to quartz are that at high temperatures GAPO does not twin until approximately 1000°C, and also the crystals are relatively insensitive to temperature over large temperature ranges (>100C°).(Thanner et al. 2002) The thermal behavior of gallium orthophosphate with a y-12.5° cut can be seen in Figure 29. The GAPO crystals have a broad temperature range where there is only a small frequency change with temperature, which is centered at approximately 300°C. The low sensitivity of the resonant frequency to temperature where naphthenic acid corrosion is active makes gallium orthophosphate optimum for in-situ corrosion measurements in a refinery environment.

Gallium orthophosphate crystal microbalance (GPCM) mass loading was calculated using the method of Lu and Lewis, which accounts for viscoelasticity differences between the thin film sample and the piezoelectric crystal.(Lu & Lewis 1972; Stienhem & Janshoff 2006) In order to obtain the mass loading on the crystal, the following relationship presented in *equation 4* was applied.

$$\Delta m = -\tan^{-1}\left(\tan\left(\frac{\Delta f \pi}{f_o}\right)\frac{z_{GAPO}}{z_{Fe}}\right)\frac{z_{Fe}}{2\pi f} \qquad \{4\}$$

f_o is the fundamental frequency (Hz), Δf is the change in frequency (Hz), z_{GAPO} is the acoustic impedance of gallium orthophosphate (kg/(m^2-s), z_{Fe} is the acoustic impedance of iron (kg/(m^2-s), f is the frequency at time t (Hz), and Δm is the mass areal density at time t (kg/m^2). When applying the crystal microbalance in a liquid, there is also a shift in frequency due to viscous loading of the crystal by the liquid. The viscosity effect is related the frequency of the crystal via the expression in *equation 5*.(Kanazawa & Gordon II 1985)

$$\Delta f = -f_0^{3/2}\left(\eta_L \rho_L / \pi \mu_{GAPO} \rho_{GAPO}\right)^{1/2} \qquad \{5\}$$

$\boldsymbol{\eta}_L$ is the viscosity of the liquid (Pa-s), and ρ_L is the density of the liquid (kg/m^3), μ_{GAPO} is the shear modulus of GAPO (Pa), and ρ_{GAPO} is the density of GAPO (kg/m^3). However, it has been shown in the literature that that *equation 4* is still applicable as long as the density and viscosity of the liquid remain constant during the test as temperatures are kept constant.(Martin et al. 1991) The constant viscosity of the oil used in the corrosion experiments was confirmed by calculating the viscosity over a large temperature range (Figure 30). My objective was to measure near-instantaneous corrosion rates rather than rates that are averaged over relatively long periods of time. Near-instantaneous corrosion rates are important sources of information about the course of the reaction and the corrosion intensity at any instant.

To calculate corrosion rate, the change in mass is divided by the change in time, shown below in *equation 6*. This method of calculating corrosion rate is the general practice in the field, however by looking at short time periods, additional information about the corrosion reaction can be gained.

$$CR = \frac{\Delta m}{\Delta t} \quad \{6\}$$

To determine the near-instantaneous corrosion rate, the change in mass of the sample was measured over intervals of five minutes. The five minute time period was the shortest time period that provided a high signal to noise ratio. The five-minute period for calculating corrosion rate was determined by minimizing sinusoidal noise on a gold coated crystal in a pure mineral oil caused by the band heaters.

Microgravimetry of Iron

Iron is the major component of carbon steel, which is the material of construction of most pipelines in the refinery. It is well known that naphthenic acids present in the crudes attack steels and the refinery materials are destroyed by the formation of soluble corrosion products, which are then released into the oil stream. As previously mentioned, the corrosion process amounts to a metal-ligand reaction between iron and naphthenic acid molecules in non-polar, non-aqueous oil media. The corrosion product $Fe(RCOO)_2$ is highly soluble in oil, and readily goes into solution after formation. The high solubility of the corrosion product results in a steady depletion of Fe from the surface until the reaction virtually stops when either iron or the acid in the solution is consumed below the threshold of the reaction.

The lowest temperature that resulted in a measurable corrosion rate was 220°C. In the test conducted at 220°C there was an initial period of 15 hours in which the corrosion rate was lower than 0.01 mm/yr (average value 0.003 mm/yr), however the corrosion rate increased over the next 8 hours at which time the experiment was terminated and the corrosion rate reached its maximum value of 0.135 mm/yr. The time dependent behavior is attributed to (1) the slow rate of penetration of the sample's surface oxide during the first 15 h of the test, followed by (2) the direct naphthenic acid attack of bare iron, during which time the corrosion rate progressively increased as the surface area of iron undergoing corrosion increased.

The values of the maximum corrosion rates as a function of temperature in mineral oil with 3% naphthenic acid are within the range of what has been reported in the literature for pure naphthenic acid corrosion of steel.(Qu et al. 2006; Gutzeit 1977; Turnbull et al. 1998) In this study, the maximum corrosion rate of iron increased with temperature, with the highest rate taking place at the maximum testing temperature of 320°C (

Table 7). Commercial naphthenic acids are a mixture of aliphatic acids with a range of boiling points.(Hsu et al. 2000; Fan 1991) Thus, the more reactive, lower molecular weight species slowly decrease in concentration as the temperature is raised over the range of the testing temperatures. I believe the large range in acid boiling points of the commercial naphthenic acid mixture to be the reason for the time to achieve a 300 μg weight loss remaining constant between 260°C and 280°C. A similar result was reported by Turnbull et al., who found the corrosion rate depended on the number of carbon atoms in the naphthenic acid molecule. The corrosion was a maximum for

naphthenic acids with around 10 carbon atoms. The corrosion rate slowly decreased with increasing carbon numbers greater than 10 and then resumed increasing at a higher rate with higher carbon numbers. (Turnbull et al. 1998) Dettmann et al. also found a similar result with acid between acid structure and corrosivity, with increasing molecular weight decreasing corrosion in a homologue.(Dettman et al. 2009) It is important to mention that the maximum corrosion rate of a crude of naphthenic acid blend will depend on the structure of the acids present as well as the concentration, and while this work found commercial blend is most corrosive at the high temperature limit of 320°C on iron, a crude may have its highest corrosivity in a lower or higher temperature range, depending on the boiling points of the constituting acids.(Babaian-Kibala 1993; Dettman et al. 2009; Behar & Albrecht 1984)

The use of GPCM not only allows for fast measurement of corrosion rates, but also allows for interrupting the corrosion process at precise times and observing the corroded surface closely under an electron microscope. Observing the surface at various stages of the corrosion process has provided insight into the evolution of the corrosion attack, and has provided an explanation for the time dependency of the corrosion rate, such as the increasing corrosion during the beginning of the experiment in Figure 34.

A set of experiments was performed in which the corrosion process was interrupted, and the sample was removed and inspected with a scanning electron microscope. After the SEM examination, the crystal was placed back into the cell, and the experiment resumed until the next predetermined time for interrupting the reaction. The test was first interrupted when a small positive rate of corrosion was first observed. The second interruption coincided further into the region of increasing corrosion rate, near to the steady state corrosion rate. The third test was uninterrupted and shows the microstructure 2.5 hours after corrosion reached a steady state value. The corrosion rate vs. time plots for the interrupted tests are below in Figure 39.

The scanning electron micrographs obtained during the course of the interrupted corrosion experiment are shown in

Figure 40.

Figure 40a shows the as sputter deposited surface. After a small positive corrosion rate was detected, the microstructure shows the beginning of the corrosion process and the initiation of pits in the oxide (

Figure 40b). However, after a larger increasing corrosion rate was detected, the sample exhibited a significant number of shallow pits as shown in

Figure 40c. The steady state corrosion microstructure is exhibited by the image presented in

Figure 40d.

Figure 41 shows a region of the sample from

Figure 40c that displayed pits under high magnification. The image in

Figure 41 reveals the presence of small, crystallographic etch pits in the air-formed oxide that covers the iron's surface. Presumably the small hole, approximately 20 nm in diameter, at the bottom of many of the crystallographic oxide pits is where the corrosion propagated into the iron itself.

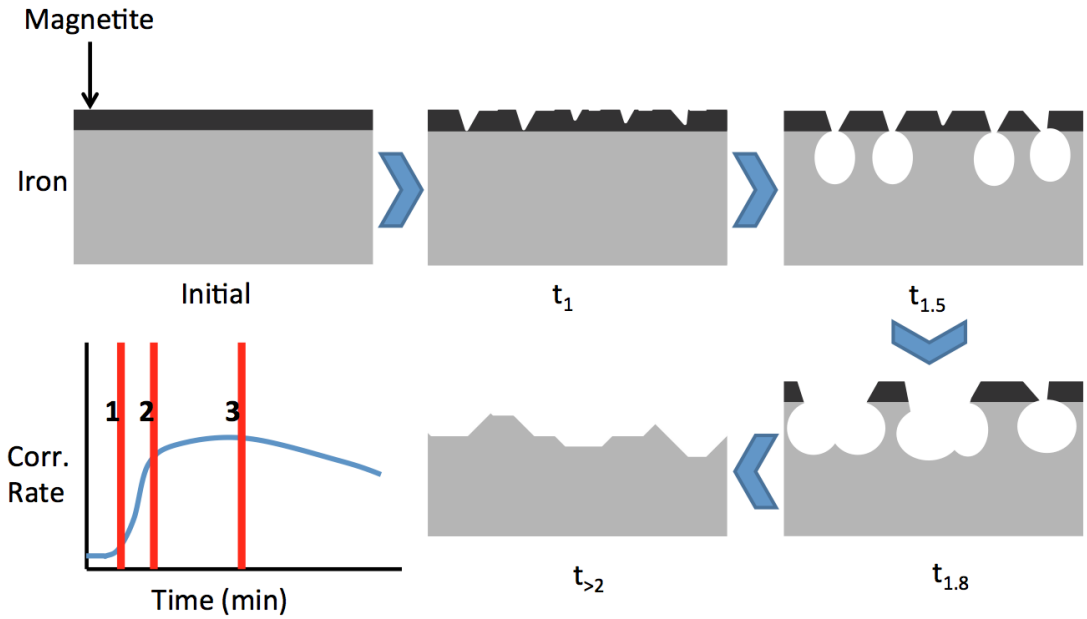


Figure 113. Schematic diagram of plausible mechanism of the corrosion at the interface of iron and naphthenic acid

As shown in the bottom right of
Figure 40, when the corrosion rate reaches a steady state value, the pits have largely vanished and the entire surface is corroded. The evolution of the corrosion, as described by the scanning electron micrographs presented in
Figure 40, combined with the time dependency of the corrosion rate, as indicated by the results presented in Figure 39, suggests the following scenario. Corrosion initiates by etch pitting of the air-formed oxide.(Brantley 2008; Spink & Ives 1971) During the etch-pitting stage of the corrosion process the crystal microbalance is able to detect a small loss of mass. Once the oxide is locally penetrated and iron is exposed at the base of etch pits the underlying iron is rapidly corroded. When the corrosion rate has reached its steady state value, the corrosion attack of iron has entirely undercut the etch-pitted, air-formed surface oxide. The steadily increasing corrosion rate, which began at the time of etch pitting of the surface oxide and concluded when the steady-state corrosion rate was reached, is a consequence of the progressive increase in the surface area of iron undergoing corrosion. A graphic representation of the proposed mechanism of naphthenic acid corrosion is shown in Figure 113.

Effect of Acid Structure and Activation Energy

To determine the effect of chain length, as well as the effect of the presence of cycloalkane rings on the corrosivity of naphthenic acids, experiments were conducted on saturated fatty acids and simple cycloalkane acids. The goal of the naphthenic acid structure experiments was to determine a correlation between the length of the alkane chain, as well as the presence of rings to how aggressive an acid is towards iron. The single naphthenic acids selected for this study were octanoic, dodecanoic, stearic,

cyclohexanecarboxylic, cyclohexaneacetic, and cyclohexanebutyric acids. The aforementioned acids were selected to represent the most corrosive acids saturated fatty and single ringed acids, as reported by Dettman. (Dettman et al. 2009)

The results of the naphthenic acid structure experiments were analyzed with respect to number of cycloalkane rings present in the acid. For the saturated fatty acids, there was a maximum steady state corrosion rate associated with dodecanoic acid. The higher corrosion rate for dodecanoic acid is consistent with the results of Turnbull, which reported a maximum corrosivity for a carbon number of 9.(Slavcheva et al. 1999) Interestingly, the shorter alkane chains were associated with longer periods to achieve the steady state corrosion rate. These results suggest that the longer chain assists with dissolution of the native iron oxide. The corrosion rate results for the saturated fatty acids are consistent with adsorption studies done on carboxylic acids onto carbon in heptane, which showed higher a enthalpy of displacement associated with longer alkane chains.(Liphard et al. 1980) The converse trend was found for the single ringed structures, where a longer alkane chain was associated with a longer time to achieve a steady state corrosion rate. These results might be attributed to the interactions between cycloalkane rings in adjacent acids, however, additional acids are required in order to confirm the trend.

In addition to studying the effect of structure, the activation energy of the reaction was desired. The activation energy is an important piece of information, as it can be used to understand the rate-limiting step of the reaction. In the literature, there have been attempts to calculate the activation energy of naphthenic acid corrosion of steel. However, these studies were performed on steel with acid mixtures over long periods of time. There is a large variation in the literature values reported, from ~30 kJ/mol-70 kJ/mol, which is not surprising as it is impossible to calculate a single activation energy for a mixture of acids. (Gutzeit 1977; Slavcheva et al. 1999) To further compound problems, use of industrial steel coupons, and a time dependence of the corrosion rate convolute the results.

To address the activation energy of a naphthenic acid systematically, experiments were performed on samples pure iron, with a single naphthenic acid structure—cyclohexanebutyric acid. The reason for using cyclohexanebutyric acid is the presence of a cycloalkane ring, and its' position as a highly corrosive naphthenic acid.(Dettman et al. 2009) By using a single acid, and controlling the metallurgy, I was able to apply the first order kinetics approximations. The rate of the reaction was taken after a steady state corrosion rate had been obtained from the GPCM experiments. By using the corrosion rate after a steady state value is established, I was able to exclude the effect of the oxide dissolution on the corrosion of iron, which has its own activation energy. The activation energy experiments were conducted between 240-320°C and the Arrhenius Plot for the aforementioned experiments are shown in Figure 114. The activation energy of cyclohexanebutyric acid using the first order kinetics approximations is 55.4 kJ/mol, close to the results of Gutzeit.(Gutzeit 1977) The value of activation energy (~55kJ/mol) suggests that the rate-limiting step is either adsorption/desorption or a charge transfer step.

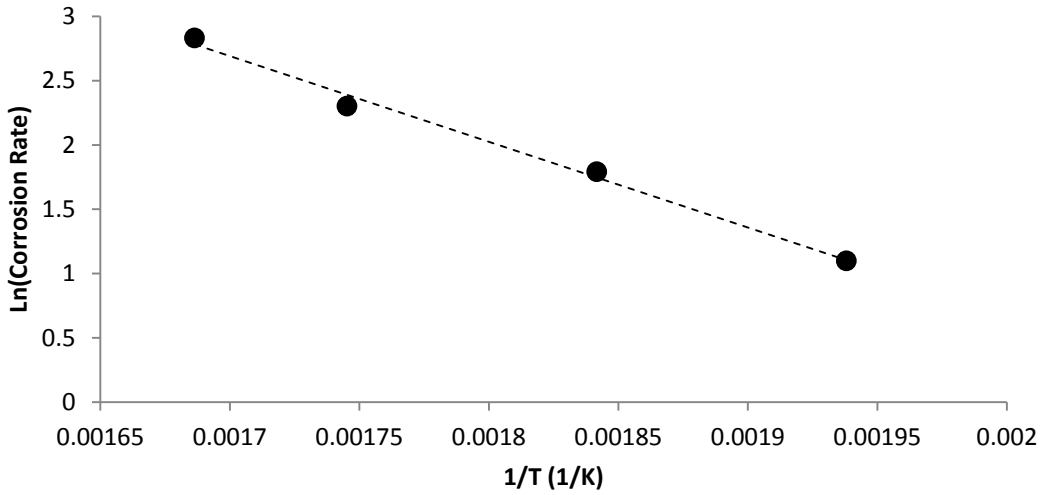


Figure 114. Arrhenius plot of corrosion rate of cyclohexanebutyric acid on iron

Microgravimetry of Transition Metals

To gain additional insight into the kinetics prevalent and the mechanistic pathway being taken during the course of the corrosion reaction of steel and alloys, the scope of the microgravimetry study was expanded to study the effect of naphthenic acid on various other important constituent metals present in the alloys widely used in crude refineries. Using the microbalance technique allows for understanding the progression of the corrosion reaction, as well as rapid assessment of corrosion resistance. However, to understand the origin of the resistance of some of the alloying elements, oxide removal testing provides the ability to deconvolute the corrosion resistance of a protective oxide and the innate resistance of a base metal to naphthenic acid attack. This two-pronged approach gives much more information about the processes taking place when compared to conventional testing.

Chromium

Chromium serves as an alloying element in many low alloy steels and is the dominant alloying element in all stainless steels. Both 304 and 316 stainless steels are used in applications where naphthenic acid attack might occur.(Breen 1974) While 316 stainless steel exhibits superior naphthenic acid resistance, the protective air-formed oxide as well as the passive films formed on both 304 and 316 in most aqueous solutions is a chromium oxide. While 304 and 316 nominally contain 18 wt. percent and 16 wt. percent chromium respectively, smaller concentrations of chromium dramatically improve the naphthenic acid corrosion resistance of ferrous alloys.(Gutzeit 1977) For example, the NAC resistance of 410 stainless steel, which contains nominally 12 wt. percent chromium, is markedly superior to that of carbon steel.(Hau 2009)

Figure 52 presents the corrosion rate of chromium measured via GPCM as a function of time of immersion in 3 wt. percent NA at 270°C. The results indicate

chromium displayed no appreciable corrosion over the two-hour testing period. FT-IR spectra (not shown) of the test solution before and after testing indicated no change in acid concentration, which supports the absence of corrosion.

The corrosion resistance of chromium is further confirmed by comparing the SEM micrographs of the as-sputtered surface of chromium before and after the GPCM experiment. There is no evidence of corrosion due to exposure to naphthenic acid (

Figure 58). Collectively, the results of the corrosion rate measurements, SEM studies, and IR spectroscopy indicate that either chromium metal is nonreactive with naphthenic acid or that chromium's native oxide is resistant to naphthenic acid attack.

To assess whether the absence of corrosion in the GPCM tests is due to the protection provided by the air-formed chromium oxide, or is the result of chromium metal's intrinsic corrosion resistance, additional experiments were performed on bulk samples in which the chromium oxide was removed in-situ in de-oxygenated 3 wt. percent NA. By removing the oxide in-situ, bare metal is exposed to the corrosive solution, which allows for determination of the inherent resistance of elemental chromium to naphthenic acid. The change in the appearance of the ground surfaces was used to estimate the extent of corrosion. The surface of a sample that was immersed in 3 wt. percent NA, then ground in situ to remove its surface oxide, followed by continued exposure to 3 wt. percent naphthenic acid for 4 hrs. was compared to an identical sample that was immersed in acid-free oil, then ground in situ, followed by 4 hrs. of exposure to acid-free oil. The sample tested in 3 wt. percent naphthenic acid showed evidence of corrosion. However, to provide more compelling evidence of the susceptibility of bare chromium to NAC, identical experiments were performed with a higher acid concentration of 15 wt. percent naphthenic acid (TAN 45-50). The scanning electron micrographs presented in

Figure 77 indicate the attack on chromium results primarily in uniform corrosion, as is evident by near complete removal of grinding marks in the corroded sample (compare

Figure 77 a & b). The results indicate oxide-free chromium is uniformly corroded in NA although not as severely as is iron. An XRD and EMPA comparison of the ground and ground and corroded samples showed the presence of a small amount of chromium carbide in both samples, as well as the presence of a chromium oxide. Since the same species were detected whether NA was present in the oil or not, it was assumed that the oxide present is the native air formed oxide resulting from exposure to air upon removal from the autoclave.

Molybdenum

Empirical evidence indicates that a small amount of molybdenum is responsible for 316 stainless steel's superior resistance to naphthenic acid corrosion compared to that of 304 stainless steel. (Breen 1974; X. Q. Wu et al. 2004) The GPCM experiments of molybdenum were conducted to further understand the disparate behavior of these two corrosion resistant alloys. The results from the in-situ GPCM corrosion tests of molybdenum are presented in Figure 53.

XRD and EMPA measurements of the sample exposed to naphthenic acid indicated the presence of molybdenum carbide and molybdenum oxide on the sample. However, as will be discussed in the oxide removal test data below, only the molybdenum oxide concentration is correlated with NA exposure. In addition, inspection by SEM of the sample's surface after the corrosion experiment (

Figure 59) is also consistent with the growth of a product on the surface. Thus, the initial negative corrosion rate is attributed to the formation of a molybdenum oxide layer. If the negative corrosion rate was solely due to an increase in surface roughness without product formation, this would require active corrosion, and a positive corrosion rate would have been sustained during the experiment.

FT-IR spectroscopy of the test solution signified a significant decrease in the amount of naphthenic acid (~80% reduction). These results suggest that the naphthenic acid is consumed or degraded by exposure to molybdenum. A back of the envelope calculation shows that the reaction cannot be solely due to corrosion product formation, as the relatively small mass change of molybdenum (~$5x10^{-7}$ mol) is not consistent with the relatively large fraction of acid lost from solution(~10^{-2} mol).

The high corrosion resistance of molybdenum is not unexpected, as 316 stainless steel displays improved corrosion resistance in naphthenic acid versus 304 stainless steel due to the addition of 2.3 wt. percent Mo, and research has shown that additional molybdenum content further decreases corrosion.(X. Wu et al. 2004) In addition, in concentrated fatty acids (~85%) at high temperatures found in tall oil service (~275°C), small increases in molybdenum content have a marked effect at decreasing corrosion and pitting of alloys.(Templeton 1970) In aqueous systems, the small amount of molybdenum acts to prevent pit growth in 316, and the same mechanism may be operative in preventing naphthenic acid attack.(Alvisi & Lins 2011) As already mentioned, naphthenic acid corrosion of iron initiates by pitting of iron's air-formed oxide film. The same mechanism might be active for naphthenic acid corrosion of stainless steel, where dilute concentrations of molybdenum in the alloy are able to stifle pit growth and thereby provide improved resistance to naphthenic acid corrosion.(Alvisi & Lins 2011)

To ascertain whether air formed molybdenum oxide is responsible in whole or in part for molybdenum's resistance to naphthenic acid corrosion, the surface oxide was removed in situ from a sample of molybdenum. When the air-formed oxide was mechanically ground away in 3 wt. percent NA a small amount of uniform corrosion took place. The corrosion was more pronounced when the experiment was conducted in 15 wt. percent NA for 4 hrs. Uniform corrosion occurred over the metal surface, as is evident by the reduction of grinding marks after exposure to NA. The extent of corrosion is similar to that of chromium (compare
Figure 78 to
Figure 77) and significantly less than that of iron. An XRD and EMPA analysis was also performed on the samples. The EMPA analysis displayed a high concentration of carbon on both types of samples (likely a carbide), along with an increased signal for oxygen for the samples exposed to naphthenic acids. The XRD analysis was not able to definitely confirm the presence of a carbide due to peak overlap between the molybdenum and the

carbide. These results suggest that molybdenum oxide is responsible for the corrosion resistance of molybdenum in naphthenic acid media. Given the acid reducing behavior of molybdenum, it is likely that the active corrosion only occurs until the naphthenic acids are removed from the solution via a decarboxylation process. It is not currently known whether the molybdenum metal or the molybdenum oxide is the active species for decarboxylation.

Zinc

Zinc is a highly active metal with a standard reduction potential of -0.76V vs. SHE. Zinc is commonly used for cathodic protection in aqueous systems, and forms many organometallic complexes.(Rappoport & Marek 2006) In addition, brasses exposed to organic acids tend to dealloy.(Garverick 1994) However, in order to improve the understanding of naphthenic acid attack on other active metals, experiments on zinc were performed. Initial experimentation at 270°C was unsuccessful. As zinc possesses a low melting point, the electrode softened significantly at 270°C, which made data acquisition impossible. In order to facilitate experimentation, the testing temperature was reduced to 200°C. At 200°C zinc was found to be highly reactive in naphthenic acid media, as shown in Figure 54.

The maximum corrosion rate for zinc was 29 mm/yr, but this rate was sustained only over a short time period. In addition, for the experiments on zinc, the experimental data was averaged over a one-minute period, in order to discern the corrosion taking place. The rapid decrease in corrosion rate is due to depletion acid from the solution, which was confirmed via FT-IR measurements of the test solution after experimentation. In addition to the very rapid corrosion, the zinc microstructure, shown in

Figure 60, shows evidence of uniform corrosion. Due to the active nature of the corrosion, oxide removal experiments were not performed for zinc.

Copper

Copper, while not employed in refining applications due to its low resistance to sulfidation, is more corrosion resistant than iron in most aqueous systems due in part to its higher standard reduction potential.(Graedel et al. 1983) In addition, Gutzeit showed that Monel (64.7 Ni- 30.9 Cu) possessed a high naphthenic acid corrosion resistance.(Gutzeit 1977) To assess whether a correlation exists between aqueous corrosion resistance and NA corrosion resistance, as well as to determine the NAC kinetics of another non-passive metal experiments on copper were performed. The microbalance corrosion data for copper is shown in Figure 55.

Copper initially corroded at a rate slightly lower than that of iron in the same test solution (~3 mm/yr). However, mass loss only occurred over the first 20 minutes of the experiment, and then there was no subsequent mass loss from the surface for the remaining hour of the experiment. FT-IR measurements of the test solution showed that only ~20% of the acid was consumed during the test. Active corrosion of copper by naphthenic acid was expected, as high corrosion rates have been reported for copper in individual saturated fatty acids.(Sarı & Kaygusuz 2003) It is worth noting the different

behavior of copper in (most) air-free aqueous solutions, where copper is thermodynamically stable, and in air-free naphthenic-acid-containing oil of the present study where copper appears to exhibit a small susceptibility to corrosion. SEM studies (

Figure 61) also showed faceting in the microstructures. The faceting is associated with the as sputtered microstructure, and is not believed to be associated with NAC. As the corrosion rate dropped to zero 20 minutes after immersion, it was postulated that the copper oxide may be susceptible to NAC, while the copper metal is resistant. The amount of metal lost during the first 20 minutes is equivalent to a thickness reduction of approximately 40 nm. The small amount of metal loss is consistent with the suggestion that the corrosion is caused by the dissolution of the air-formed surface oxide of copper.

Oxide removal experiments were performed on copper, which displayed no corrosion below 7500x magnification (

Figure 79). When the as ground and NA exposed samples' surfaces are compared at high magnification, a loose packing of sub-micron (~100nm) sized particles is found. To further understand the corrosion process, metallographically polished samples of bulk copper were exposed to three wt. percent NA. Comparison of an as polished and NA exposed sample via SEM showed that approximately 80% of the surface displayed no indication of corrosion. Over the remaining 20% of the surface, there was no evidence of active corrosion, however approximately half of the area (overall 10% of area) was covered with one micron sized islands comprised of sub-micron sized particles. An XRD analysis of the sample indicated that the particles were crystalline, however were unable to be indexed. EDS analysis of the islands indicated high concentrations of carbon and oxygen relative to the rest of the sample, indicating a possible corrosion product. As a final effort to confirm the corrosion resistance of copper's native oxide, cuprous oxide powder, and thermally oxidized copper samples were exposed to three wt. percent NA at 270°C. In both cases, the result was complete dissolution of the oxide. Based upon all of these experiments, it was concluded that copper itself is not susceptible to NAC in the test solution, however the air formed copper oxide readily dissolves.

Nickel

Nickel is used throughout petroleum refining for purposes ranging from catalysis to corrosion resistance.(Reynolds 2007) Nickel is a major ingredient in most corrosion resistant alloys used in refineries. Stainless steels, as well as highly corrosion resistant alloys such as Alloy 600 and Hastelloy C276 contain significant amounts of nickel.(Anon 1977) Because of the prevalence of nickel in corrosion resistant alloys, the inherent corrosion behavior of nickel was of interest. The microbalance corrosion experiments (Figure 56) indicated that nickel is resistant to corrosion in naphthenic acid media at 270°C. In addition, ATR FT-IR spectroscopic studies of the test solution confirmed the absence of nickel naphthenate (~2% detection limit), and a significant loss of naphthenic acid (>70%). Nickel has also been reported to be resistant to corrosion in high temperature saturated fatty acids, which corroborates these findings.(Anon 1979)

In addition to the lack of mass change of nickel during the GPCM experiment, SEM studies of the surface post experimentation (

Figure 62) show two distinct regions with different surface morphologies. Roughly two thirds of the surface was unchanged by exposure to 3 wt. percent NA, however a high number density of particles formed on the remaining surface (

Figure 62c). Thus, although there was very little change in the resonance frequency of the GPCM sample throughout the test, a thin, particulate deposit covered nearly one-third of the surface. The results of EDS, EMPA, and XRD were in agreement, and identified the particles as an NiO type nickel oxide. Apparently, nickel reacts with naphthenic acid and forms a solid corrosion product of NiO. The amount of NiO that was formed was far too small for the corrosion of nickel to explain the decrease in concentration of NA. Currently, the mechanism of the reaction between nickel and naphthenic acid is unknown, however, this phenomena is currently being studied further.

Air formed oxide removal experiments were performed on a macroscopic size sample of nickel to further elucidate the corrosion resistance of nickel. The scanning electron micrographs presented in Figure 80 show the surfaces of nickel samples that were ground in situ at 270°C in (a) oil without NA, and (b) oil with 3 wt. percent NA. Comparing the two photographs indicates that a particulate deposit forms on the surface of nickel that was stripped in situ of its air-formed oxide and exposed to 3 wt. percent NA at 270°C. XRD and EMPA measurements identified the particles as NiO. FT-IR spectroscopy of the 3 wt. percent NA solution at the conclusion of the test indicated most the NA had been decomposed. Thus, exposing bare nickel to 3 wt. percent NA results in the formation of NiO particles and the near complete decomposition of NA.

Silicon

Silicon is added to most steels to deoxidize the molten alloy before it is solidified. Small amounts of silicon (0.15-0.3 wt. %) are used in many refinery alloys to improve corrosion resistance.(Setterlund 2007) The primary purpose is to increase sulfidation resistance; however silicon may also have an effect on naphthenic acid corrosion. In a refinery, as well as in other applications, high silicon cast iron is successfully used in high temperature organic acids due to a passive layer of SiO_2.(Farraro & Stellina Jr. 1996; Davis 1996) The NAC behavior of silicon relative to that of the metals considered in this study was of fundamental interest because of silicon's covalent bonding (rather than the metallic bonding exhibited by the other alloying elements investigated in the present study) and silicon's place in the periodic table (i.e., outside the region occupied by the transition elements that were also investigated). Silicon is a semiconductor/insulator and possesses the noteworthy chemical property of catenation to more Si atoms.(Okada 1998) The results of the GPCM corrosion test of pure Si exposed to 3 wt. percent naphthenic acid at 270°C is presented in Figure 57.

Silicon's corrosion rate was a negative value throughout the entire experiment, which indicates deposition occurred onto the surface of the sample. SEM micrograph of the GPCM sample after completion of the corrosion test is presented in Figure 63b along with a micrograph in Figure 63a of the sample's surface before corrosion testing. The results indicate a change in the surface as a result of exposure to NA. Additionally, XRD and EMPA analysis showed an increase in the concentration of oxygen after exposure,

the presence of SiO_2, as well as other peaks in XRD that could not be identified. The nature of the reaction between Si and NA in oil is not yet known. There are no known reports of corrosion resulting in the formation of silicon naphthenate, which may be attributed to the very low adsorption of carboxylic acids on Si/SiO_2 surfaces in non-polar solvents.(Kelesoglu et al. 2012) A plausible mechanism behind the observed behavior may be based on its catenation property, a characteristic feature present strongly in Carbon (Characteristic feature of Gr IV of the periodic table).(Hartley 1987) As suggested by Buriak, at higher temperatures these unstable Si-Si bonds break up to form free radicals. These reactive free radicals then influence a cascade of free radicle generation in the mixture and finally form more stable hetero atomic bonds resulting in organo-silicon compounds.(Buriak 2002; Walch 2008) The free radicals generated then react with other organic molecules in the vicinity and form various oil insoluble organo-silicon compounds. As Si-C bonds can sometimes be stronger than C-C bonds, the reaction of silicon with hydrocarbons is not surprising, and this is in line with the observations of Guo and co-workers.(Anon 1977; Guo et al. 2005)

While there are no other reports of silicon's resistance to naphthenic acid attack, high silicon steels have been employed in refineries for their improved corrosion resistance. Silicon has been shown to increase the corrosion resistance of copper in concentrated organic acids significantly, especially as temperature increases.(Elder 1975) Because silicon oxide was formed throughout the entire experiment, oxide removal testing was not performed.

Electrochemical Study of Solutions

Nature of the Corrosion Reaction

Fundamentally, corrosion reactions can either proceed chemically or electrochemically. The reaction constants, concentrations of the species involved, and the temperature of the system completely describe the kinetics of a chemical reaction. An electrochemical reaction adds in an additional term, the electrostatic potential, which alters the Fermi level of the electrons in the metal. Changes in the potential alter the driving force of the reaction, which can act to either accelerate or stop processes from occurring.

For an electrochemical mechanism to be active, there must be at least one electron transfer involved in the overall reaction. In addition, every electrochemical reaction requires charge neutrality; there must be an oxidation and reduction site. In conventional electrochemical testing, the oxidation and reduction sites come in the form of a working and counter electrode in electrical contact. However, in the case of crude oil, the resistivity is in the range of 10^{10} to 10^{15} Ω-cm, and that extremely high resistivity impedes electrical contact. Quantitatively, the electrochemical potential difference between anodes and cathodes in an electrochemical experiment can be represented by *equation 7*.

$$E_a = E_{app} - IR \qquad \{7\}$$

E_a is the actual electrochemical potential difference (V), E_{app} is the applied electrochemical potential between the anodes and cathodes (V), I is the total cell current (A), and R is the cell resistance (Ω). To give insight into whether an electrochemical mechanism is active in crude oil, a back of the envelope calculation was performed. Assuming a 10 nm spacing between 1 cm^2 plate electrodes with a 1 mm/yr corrosion rate (80 $\mu A/cm^2$) and a resistivity of 10^{10} Ω-cm, a large potential (0.8V) is required to overcome the IR drop. For comparison, the electric field associated with 0.8V potential difference dropping over a 10nm spacing is 80 MV/m, which is greater than the dielectric strength of the oil. Using the calculated value of electric field, along with literature reports, a chemical mechanism of corrosion is strongly suggested. (Slavcheva et al. 1999)

Applicability of Electrochemistry

Electrochemistry provides powerful tools for determining reaction mechanisms at interfaces, and the identity of active species dissolved in solution. Even though it is believed that the corrosion reaction between iron and naphthenic acid in crude is chemical in nature, electrochemical techniques can be applied to gain information about the naphthenic acids themselves. The reason for using electrochemistry is that naphthenic acids are carboxylic acids, which are themselves redox active.(Canhoto et al. 2004)

To understand the reason for using electrochemical techniques, it is helpful to understand the basics of electrochemistry. Ionic redox systems have particular energy levels associated with each of the ions. These energy levels are associated with the charge of the ion, as well as ion-solvent interactions. For any electrochemical system to be at equilibrium, the electrochemical potential of the two redox species must be equal. The potential corresponding to the equilibrium condition is given by the Nernst equation in *equation 8*.

$$\phi = \phi^o - \frac{RT}{nF}\ln\left(\frac{a_P}{a_R}\right) \qquad \{8\}$$

In the above equation ϕ is the equilibrium potential of the redox species (units of volts, V), ϕ^o is the standard reduction potential of the redox species in the solution of interest (V), R is the gas constant (J/mol-K), T is the temperature of the system (K), n is the number of electrons involved in the reaction, F is the Faraday constant (C/mol), a_P is the activity of the products (i.e., the reduced species), and a_R is the activity of the reactants (i.e., the oxidized species). The Nernst equation specifies the thermodynamic equilibrium potential for the reaction. However, when performing electrochemical experiments in a finite timeframe, kinetics information is also necessary. There are three regimes for kinetics in electrochemical reactions. At low overpotentials, also known as the linear region, the current density varies approximately directly with overpotential. At higher overpotentials is Tafel region, in which the current density increases exponentially with overpotential. Finally, at high overpotentials is the diffusion-limited regime, in which the rate of supply of reactant to or product away from the interface is slower than the rate of electron transfer. In the diffusion limited regime the current density is

approximately independent of overpotential. Using techniques that look at each of these regions provides information about fundamental kinetic parameters such as the exchange current density of the reaction, the rate constants, electrochemical reversibility, and diffusivities of each of the species.

Acids are redox active in many liquid solutions. In water, many acids dissociate completely, but even weak acids, such as the carboxylic acids dissociate to some extent. For carboxylic acids, such as naphthenic acids, the acid molecule dissociates to a proton and a carboxylate anion. The activity of these ions can then be probed using electrochemical techniques. Commonly the potential at which the proton is reduced to hydrogen gas is used to give information about the strength of the acid.(Canhoto et al. 2004) Applying the Nernst equation to the hydrogen redox system, the expression for equilibrium potential (with respect to the standard hydrogen electrode) is given by *equation 9*.

$$\phi = -\frac{RT}{2F}\ln\left(\frac{P_{H_2}}{(a_{H^+})^2}\right) \qquad \{9\}$$

If the partial pressure of hydrogen is controlled, then the equilibrium potential will vary only with the hydrogen ion activity. The hydrogen ion activity in-turn gives information about the strength of the acids. In non-aqueous solutions, analysis using the hydrogen ion activity is less straightforward, but the argument has been used with success (Barrette et al. 1984; Davis & Hetzer 1958; Kvaratskheliya & Kvaratskheliya 2000; Kim et al. 2001). Even in aprotic solvents, which poorly solvate protons, a small amount of acid molecules will dissociate, especially on the metal surface. In the case of the metal surface, the proton can be stabilized by an image charge in the metal. In this work, even though the pKa of most naphthenic acids are >20, they are assumed to dissociate to some extent on the surface of the metal. Assuming that the large and bulky carboxylate anion ($RCOO^-$) can be stabilized in the solution, the reduction of the acid will give information about the concentration and reactivity of the acid species.

IR Drop

Many electrochemical techniques have been developed and applied to studying corrosion.(Bard & Faulkner n.d.) Almost all of these techniques were developed for use in aqueous solutions though. The high conductivity of aqueous solutions makes electrochemical testing relatively straightforward. However, the resistivities of crude oils are commonly in the range of 10^{10} to 10^{15} Ω-cm, in stark comparison with the 25 Ω-cm resistivity of seawater.(Kaye & Laby 1995) As such, the IR drops associated with crudes prevent any useful data from being obtained. In order to perform electrochemical experiments, the resistance of the oil has to be reduced to a value in which the electrode potentials could be controlled. Creating a conductive oil is not a trivial task, as the alkanes that make up most of the crude have very low dielectric constants and cannot efficiently solvate ions such as those commonly used for supporting electrolytes. To reduce the resistance of the test solutions to a value that supported experimentation, two approaches were used in the current investigation. The first approach is the use of an

ultramicroelectrode (UME). The second approach is adding a supporting electrolyte to the solution that can be solvated by the oil, as well as does not react with the solution.

A UME is an electrode that has at least 1 dimension less than 100 µm. The small electrode area greatly reduces the current passed, which minimizes the IR drop.(Aoki 1993) In addition, research done by Newman, showed that the resistance of current flow to a disk is only felt within a short distance within the solution that is related to the electrode size.(Newman 1966) Thus, the cell resistance for a UME can be expressed by *equation 10*.

$$R = \frac{\rho}{4r} \qquad \{10\}$$

R is the cell resistance (Ω), ρ is the electrical resistivity of the solution (Ω-m), and r is the electrode radius (m). Using the fact that solution resistance scales inversely with radius, and that faradaic current scales with the electro active area (which scales with r^2 for a disc). Thus, the IR drop is directly related to the electrode radius. In particular, smaller electrodes will reduce the IR drop. The advantage of small cell resistance provided by a UME holds until the micro scale is achieved. In the UME regime, the faradaic current is directly dependent on the smallest electrode dimension, r.(Aoki 1993) The influence of the electrode's dimension comes from diffusion to the UME surface, which controls the current response of the system. Calculations based upon a 1 mM concentration of electro active specie with diffusivity equivalent to that of naphthenic acids show that the solution resistivity must be less than 10^6 Ω-m in order to reduce the IR drop to below 10mV. However, as the resistivity of the oil is approximately 10^{12} Ω-m, the use of an UME alone will not lower the cell resistance sufficiently. In order to reduce the cell resistance, the solution's resistivity much be lowered, which requires the use of supporting electrolytes.

The term supporting electrolyte is used here to describe an ionic species that can travel independently in the test solution, is stable over a large range of voltage, and does not react with any other species in the system. Examples of supporting electrolytes in aqueous solutions are stable inorganic salts such as potassium chloride or mineral acids for testing in acidic conditions. In nonaqueous electrochemistry commonly used supporting electrolytes include tetrabutylammonium perchlorate, and imidazolium based supporting electrolytes, but these are not soluble in oil. In addition, in nonpolar solvents, ions of many supporting electrolytes self-associate due to electrostatic interactions.(Fraser et al. 2007a) In order to overcome ionic self-association, larger and bulkier ions that could be solvated by the alkanes present in the oil were required. Room temperature ionic liquids (RTILs) were the ideal candidates for increasing the conductivity of an oil solution.

Cyclic Voltammetry

Voltammetry is a term used to describe a number of controlled potential electrochemical techniques.(Bard & Faulkner n.d.) Cyclic voltammetry is one type of voltammetry in which the potential is swept linearly between two values, resulting in a

triangular potential vs. time plot that appears as a saw tooth. Cyclic voltammetry is a powerful tool for investigating the identity of species dissolved in an electrolyte, as well as the properties of that species.(Bard & Faulkner n.d.) Every electrochemically active species has a potential at which the oxidation and reduction reactions are in equilibrium at the interface of interest, which is called the equilibrium potential. The equilibrium potential is governed by the Nernst equation. When performing a cyclic voltammetry experiment, the potential is swept from an initial value, and when the potential approaches the equilibrium potential for a redox reaction, the current will increase exponentially as the driving force for the reaction is increased. For an oxidation reaction, the current will be positive, as electrons are being removed from the reactant, forming a more positively charged product (most often a cation). On a macroelectrode, the current response appears as a peak in a plot of current vs. voltage, as all of the reactant adjacent to the electrode surface is depleted. In order to support further reaction, additional reactant must diffuse to the surface via diffusion. As the applied potential continues to increase, the current decreases due to the transport limitation, creating a peak, and a reverse peak (reduction) is found upon reversing the direction of potential scan. An example of a voltammogram for a macroelectrode is seen in

Figure 115. The half wave potential can then be calculated as the halfway point between the potential at the anodic peak, and the potential at the cathodic peak. The half wave potential is then taken to be an approximation of the equilibrium potential.

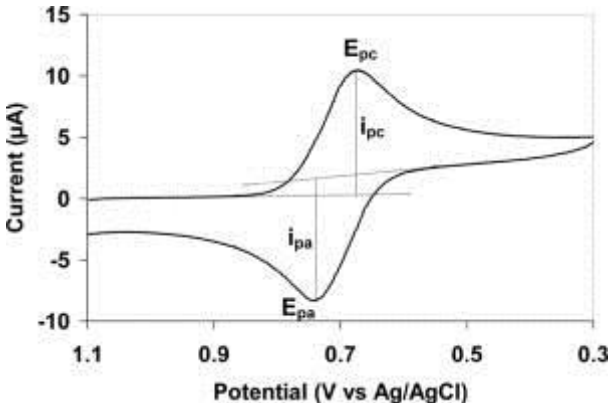


Figure 115. Example I-V curve from cyclic voltammetry experiment at macroelectrode "Cyclovoltammogram" by Lifer21 - WP:EN. Licensed under Public Domain via Wikimedia Commons - http://commons.wikimedia.org/wiki/File: Cyclovoltammogram.jpg#/media/File:Cyclovoltammogram.jpg

As mentioned earlier, UMEs can be used to minimize the IR drop. By employing UMEs in cyclic voltammetry experiments, the potential of the working electrode can be controlled in more resistive solutions.(Aoki 1993) The current response of a UME in a cyclic voltammetry experiment is slightly different than that of its macro counterpart. The small dimensions characteristic of a UME, have the effect of increasing the rate of diffusion to and from the surface. In the case of a disc electrode, the diffusion profile changes from that of a linear profile (1D), to a cylindrical or spherical profile (3D). The change in diffusion profile increases the mass flux to and away from the surface by several orders of magnitude, which in turn changes the current peaks to a single sigmoid.(Compton & Banks 2007) By increasing the rates of diffusion, once the reactant adjacent to the electrode is consumed, it continues to be replenished and there is a steady

state relationship between the overall kinetics and diffusion. The steady state relationship causes the peaks to appear as sigmoidal steps, with steady state plateaus of current instead of peaks, such as the response seen in

Figure 116. It is important to note that as the rate of diffusion to and from an UME is orders of magnitude higher than that of a macro electrode, reaction products are removed from the solution adjacent to the electrode rapidly preventing accumulation. The result of the rapid diffusion of reaction products away from the electrode (i.e., oxidized species) is that unless both the oxidized species and reduced species are present in significant quantities in the bulk of the solution, a reverse peak will not be present such as seen with a macro electrode. The microelectrode voltammogram also includes more discernible information than the macroelectrode counterpart. Macroelectrodes have a complex relationship between transport and kinetics, which makes data analysis to obtain bulk concentration very difficult. As microelectrodes have rapid radial diffusion, there is neither reactant depletion nor product accumulation, and this greatly simplifies the transport relationships.(Aoki 1993) For UMEs, the half wave potential is taken as the half current potential, defined as the plateau current minus the background current below the peak. The plateau current also provides additional information. If the diffusivity of the electro-active species is known, then its concentration can be extracted from the plateau current, using the Cottrell equation for UMEs. (Aoki 1993).

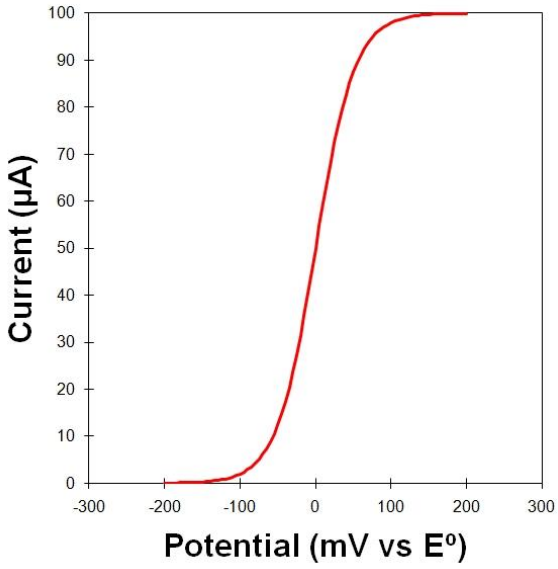


Figure 116. Example I-V curve from cyclic voltammetry experiment at UME "pine:rotating_electrode:theory" by voltammetry.net contributor - WP:EN. Licensed under Public Domain via Wikimedia Commons - http://wiki.voltammetry.net/doku.php?id=pine:rotating_electrode:theory&rev=1330315778

Supporting Electrolytes

The conductivity of a liquid is commonly tested using electrochemical techniques, such as electrochemical impedance spectroscopy (EIS). A small ac potential is applied with varying frequency to an electrochemical cell, and the current response is measured. By fitting the measured electrochemical impedance spectrum to that of a Randles circuit

shown in Figure 81, which represents a simple electrical circuit analog of the electrode/electrolyte interface, information about the solution can be extracted, such as its electrical resistivity.

In the Randles circuit, R_s is the solution resistance that is in series with the parallel configuration of C_{dl}, which is the double layer capacitance, and R_p, which is the polarization or charge transfer resistance. By applying a high frequency potential, the capacitor is shorted out, which leaves the solution resistance as the sole contributor to the current response. By performing the experiment in a confined geometry, the electrical solution's resistivity can be extracted. However, initial experimentation found that in extremely high resistance solutions with resistivities above 10^7 Ω-cm, the preferred current path was through the air between the electrodes, which is represented as a capacitor in parallel with the entire Randle's circuit.

In order to overcome the inability to EIS measure extremely high resistivities, the two-point probe resistivity measurement technique was applied. The two point probe is commonly applied to high resistance semiconductors.(Smits 1958) A two-point probe resistivity measurement is made by driving a current across two small electrodes placed in contact with the substrate, and measuring the corresponding voltage drop. The resistivity of the substrate is then calculated using *equation 11*.(Nishi & Doering 2007)

$$\rho = 2\pi s \frac{V}{I} \qquad \{11\}$$

ρ is the electrical resistivity of the substrate (Ω-cm), s is the electrode spacing (cm), V is the potential drop (V), and I is the current passed (A). Testing with high purity solvents and comparison with literature values confirmed that the two-point probe accurately measures resistivity in the high resistivity regime of crude oil, i.e. $>10^{10}$ Ω-cm (Table 8). However, when the resistivity is below approximately 10^8 Ω-cm, sources of resistance other than the resistance through the bulk become nontrivial. When the resistivity was lower than ~10^8 Ω-cm, a four-point probe resistivity configuration was applied. The four-point probe configuration utilizes four small equally spaced electrodes in contact with the substrate. The electrode configuration for four point probe measurements is shown in Figure 117. A DC current is driven across the outer electrodes, and the potential drop between the two inner electrodes is measured. The experiment is performed using four electrodes in order to avoid two additional sources of resistance. The first is a contact resistance associated with poor contact between the electrode and substrate, and the second is a spreading resistance associated with non-linear current flow into the substrate, i.e. current flowing from a point through a larger area.(Nishi & Doering 2007) To avoid the additional sources of resistances, the potential drop across the inner electrodes is used, which passes very little current.

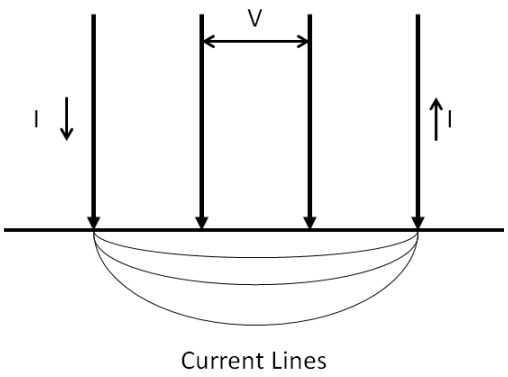


Figure 117. Schematic of four point probe measurement. Current is driven across the outer electrodes and potential drop is measured across the inner electrodes

RTILs are liquids at room temperature composed completely of partially associated ions. RTILs come in a variety of structures, and some are soluble in low dielectric constant solvents. The vast majority are classified as weak Lewis acidic cations, partially coordinated to weak Lewis basic anions, which more fully dissociate after being weakly solvated.(Tokuda et al. 2006) The amount of association that occurs is dependent on the types, magnitude, and balance of intra/intermolecular forces.

Several different classes of ionic liquids were selected for testing based upon the alkylammonium, [bmim] and $P_{6,6,14}$ classes of ionic liquids. These ionic liquids were chosen given their usage in earlier electrochemical research, commercial availability, and reported properties.(Tokuda et al. 2004; Fraser & MacFarlane 2009; Hunger et al. 2008) As shown by the conductivity experiments using 0.4M solutions of various ionic liquids in toluene in

Table 9, the RTILs with the greatest conductivity were based upon the $P_{6,6,14}$ structure. The high solubility of the phosphonium based RTILs is largely due to the greater solubility of the long alkane portions of the phosphonium based ionic liquids, which also act to shield the cation from the solution and anion. The phosphonium cation was selected because it was the largest cation commercially available and was readily soluble in low polarity media.(Fraser & MacFarlane 2009) However, there were several anions that were available with different structures. To determine the optimal structure several were tested that possessed different sizes, functional groups, and diffusivity. The anions tested were decanoate, Do[DBS], [BIS]. The results from conductivity experiments indicated that the solution's conductivity increased with increasing anion size, and increasing shielding of its charge. The influence of anion size and shielding is due to the influence of charge association within the ionic liquid.(Fraser & MacFarlane 2009) As the solvent is not able to stabilize the charged species individually, ion pairing occurs. The more shielded the charge, the more effective stearic effects are against ion association.(Fraser et al. 2007b)

As none of the commercially available ionic liquids were able to adequately reduce the electrical resistivity of the oil based solution, I designed and synthesized the ionic liquid $P_{6,6,14}$[TKIS]. The anion is extremely bulky, and the negative charge is located on the borate, which is shielded by the fluorinated phenyl rings. Application of

$P_{6,6,14}$[TKIS] ionic liquid reduced the resistivity of the toluene to a value of $1.7x10^4$ Ω-cm at a concentration of 0.3M. The anion [TKIS] reduced the electrical resistivity of toluene solutions by nearly four orders of magnitude when compared to other anions with the phosphonium cation. The disparate behavior of [TKIS] is attributed to a lack of ion association because of the large size of the [TKIS] anion stearicly hindering ion-ion coordination by stearic effects. The stearic effect is seen by the position of the charge on each of the anions. The resistivity of the ionic liquids tested decreased as the charge on the ion was located away further away from the end of the molecule. The conductivity of the solution is dependent on the free ion carriers, and thus a self-associated ion pair reacts like a dipole, rather than free charges.(Bockris et al. 2000) In nonpolar solvents the solvent molecules are not able to lower the free energy of the solution by coordinating with the ion, and the only species present for the ions to coordinate with are the cations.(Fraser et al. 2007a) While ionic liquids are generally considered to be self-dissociable ionic salts, the solvent is needed to reduce the tendency to self-associate. (Tokuda et al. 2006; Tokuda et al. 2004) Thus, the application of an ionic liquid that is solvated by the alkane solvent, and is stearicly hindered from self-associating is ideal for use as a supporting electrolyte.

The final property of the ionic liquid that needed to be considered was the voltage stability. As the ionic liquids are made of charged species, they can be electrochemically oxidized and reduced. In order to employ these ionic liquids as supporting electrolytes, the RTIL needs to be stable in the voltage region of interest. For the case of acid identification, the largest stability window was desired. Cyclic voltammetry experiments were performed on each of the ionic liquids in benzyl benzoate in order to determine the voltage stability of each of the supporting electrolytes. The results summarized in Table 10, show that the $P_{6,6,14}$[TKIS] has the largest stability window in addition to the highest conductivity. Due to the clear advantages of the $P_{6,6,14}$[TKIS] RTIL as a supporting electrolyte, it was selected for use in acid identification testing.

Palladium Hydride Reference Electrode

The experiments described in the cyclic voltammetry section above can only be performed quantitatively with direct comparison between tests if there is a potential that can be used to relate the experimental data to each other. To directly compare voltammetry data from different solution chemistries, a reference electrode must be used. Over the years, there has been a significant amount research conducted to identify reference electrodes that function in a range of solution chemistries.(Gritzner & Kuta, 1984;Gagne et al., 1980; Wynd, 193AD) In any given electrochemical experiment, the interface of interest is the interface between the working electrode and the solution. The solution/electrode interface at the working electrode is controlled by application of either a potential or current.(Bard & Faulkner n.d.) However, to compare the potential drop across the electrode/electrolyte interface of an electrode immersed in an aqueous solution against the potential drop of an electrode immersed in a nonaqueous solution is currently nontrivial. Traditionally, a reference electrode is used to relate the values of potential from one set of conditions to another. Since the inception of electrochemistry, many reference electrode systems have emerged that allow for the use of different ionic

systems. The most common reference electrodes in use today are the saturated calomel electrode (SCE, Hg/Hg_2Cl_2) and the silver/silver chloride (Ag/AgCl).(Ives & Janz 1961; Szab'o & Bkos 2010) Other reference systems in use today are employed in niche applications that utilize other redox active species.(Ives & Janz 1961) The selection of reference electrode is application dependent, with the most important factors being solvent, temperature, pressure, liquid junctions, and side reactions with ions. For example, the SHE has a very high exchange current density and a well-defined potential, but it requires a high concentration of both hydrogen ions as well as a hydrogen gas atmosphere. Implementation of the SHE is nontrivial, and the very presence of excess hydrogen ions can alter many electrochemical reactions such as corrosion.

Despite the fact that there has been much work done to find reference systems that have a high exchange current density; the vast majority of the work has been restricted to aqueous systems. Currently in the literature, there have not been any reports of a universal nonaqueous reference electrode.(Pons & Khoo 1981) Normally, pseudoreference electrodes are used for experiments in nonaqueous solutions.(Connelly & Geiger 1996) A pseudoreference electrode provides a constant potential but the potential does not correspond to the equilibrium potential of a particular red-ox system. Consequently, potentials measured with respect to a pseudoreference electrode have no thermodynamic significance. The open circuit potential of an inert electrode such as platinum is often used as the pseudoreference potential. Since an open-circuit potential is a mixed potential, the open circuit potential has no thermodynamic significance. Thus, when performing every experiment using a pseudo-reference electrode, a re-dox species of known half-wave potential is added to relate the potential of the pseudoreference electrode to the standard hydrogen scale.

The absence of a reference electrode that can serve in a variety of solvents has created a great challenge in performing electrochemical experiments, particularly in nonpolar aprotic solvents where most re-dox systems that might be used to provide a thermodynamic reference potential have very low exchange current densities due to the low solubility of ionic species. Red-ox systems with low exchange current densities are generally unsuitable for reference electrodes because their potential is very sensitive to fluctuations in flow/convection and to contaminants that collect on the electrode's surface. In protic nonaqueous media, the high dielectric constant allows for conventional reference electrodes to be modified for use because the ionic redox species (ex. Cl^-) are soluble in the aprotic media. While the performance degrades over time, the SCE can be immersed in potassium chloride saturated acetonitrile to provide a low exchange current density reference. The low exchange current density is due to the low solubility of potassium chloride in acetonitrile. In addition, the iridium/iridium oxide system can be used as a high exchange current density reference in any protic system.(Wang & Yao 2002) In aprotic systems, however, a true reference electrode has proven to be elusive. In this work, I will discuss whether the palladium/palladium hydride electrode (PdH) can act as a reference electrode in nonaqueous, aprotic media.

The palladium/palladium hydride system has been extensively studied, and is one of the most characterized metal hydride systems. Examples of applications for palladium

hydride have ranged from "cold fusion" and superconductivity to hydrogen diffusion membranes for gas purification and energy storage.(Harper 1996; Sakintuna et al. 2007; Schultz et al. 1989) The PdH electrode is already a well-established pH electrode in aqueous systems, and has been applied as a pH electrode in nonaqueous titrimetry.(Stock & Purdy 1957) A major advantage of palladium hydride over a conventional SHE is that the hydrogen is soluble within the palladium lattice. In any hydrogen-based reference, the equilibrium reaction is $2H^{+}+2e^{-}\leftrightarrow H_2$. A major difference between a conventional hydrogen based reference electrode (e.g. SHE) and the palladium hydride reference electrode, is that the hydrogen gas free solutions the hydrogen gas activity on the electrode surface is controlled by a phase equilibrium between the low hydrogen concentration α palladium hydride phase, and the high hydrogen concentration β palladium hydride phase. Thus, in the palladium hydride reference system, the α+β phase equilibrium controls the activity of the hydrogen gas as long as the two phase equilibrium is maintained.(Schuldiner et al. 1958) The alpha phase is palladium (with a face centered cubic structure) with dissolved hydrogen and a lattice constant of 3.886Å.On the other hand, the beta phase is the high hydrogen concentration phase, with an approximate stoichiometry of $PdH_{0.68}$ and a face centered cubic structure with a lattice parameter of 4.02Å.(Nace & Aston 1957) The overall reaction for incorporation of hydrogen into palladium hydride lattice is given by H (abs) + PdH_{α} (s)→ PdH_{β} (s), where PdH_{α} is the low concentration solid solution phase, and PdH_{β} is the high hydrogen phase.(Flanagan & Oates 1991b) As the palladium hydride system has been extensively studied, the precise partial pressure of hydrogen required to establish a two phase equilibrium has been established over a range of temperatures.(Dobson & Brims 1987; F. A. Lewis 1982; Dobson et al. 1972)

In most instances in the literature, the hydride phase is generated either via electrochemical charging, i.e., by reduction of H^{+} in water or by electrolysis of water, or via exposure to a hydrogen rich gas atmosphere prior to experimentation.(Oliveira 2006) To establish the palladium hydride phase equilibrium via exposure to hydrogen gas, approximately 0.1 atm is required at 70°C, while 1atm is required at 160°C.(B. F. A. Lewis 1982) The influence of temperature on the partial pressure of hydrogen required to establish phase equilibrium means that at high temperatures, large pressures of hydrogen are required to establish the two phase equilibrium at high temperatures. (Dobson et al. 1972) However, large hydrogen pressures are only necessary to form the PdH phase equilibrium at high temperatures and only 1.6% H_2 is required for phase equilibrium at 278K.(Lewis 1960) Consequently, low concentrations of hydrogen can establish a palladium hydride phase equilibrium at ambient conditions. In addition, after formation of the hydride, hydrogen does not need to be present in the aqueous solution for the PdH electrode to function, as hydrogen is present within the metal hydride.(Vasile & Enke 1965) However, despite the attractive features of a palladium-palladium hydride reference, to my knowledge there has been no attempt to employ it for use as a nonaqueous reference electrode.

In order to determine the suitability of a red-ox system to serve as a reference electrode, three criteria must be met. Namely, the reference electrode must be stable, reversible, and exhibit Nernstian behavior of the red-ox system. In order to verify the

reference behavior of the palladium hydride electrode, experiments were performed to determine if each of the criteria were satisfied.

The first experiments performed were aimed at addressing the stability of the PdH electrode in aprotic solvents. As there are no available reference electrodes that function in low dielectric constant aprotic solvents, organic species with a known, constant re-dox potential were used. In these experiments the tests were conducted with a Pt UME in a cell that contains a PdH CE/RE and a solution of 0.2 [bmim][TFB] in DCM with 0.1mM anthraquinone (AQ), ferrocene (Fc), and decamethylferrocene (dmFc). A cyclic voltammogram (CV) that is representative of a series of CVs is presented in Figure 93. An IR-corrected voltammogram of an experiment with all of the re-dox species present is shown in Figure 94. A total of 11 CVs were measured using the same Pt UME and four different PdH electrodes. Each test was performed with fresh solution. The results of the 11 tests are summarized in

Table 11. The values of the half-wave potentials that have been reported in the literature are presented in Column 3 of

Table 11.(Aranzaes et al. 2006; Ahmed et al. 2007) It is important to note that the values taken from the literature were converted to the hydrogen scale using published conversion factors.(Pavlishchuk & Addison 2002; Connelly & Geiger 1996) The difference between the values measured with respect to the PdH electrode and the values measured in the literature are listed in column 4 of

Table 11. The magnitude of the difference is approximately 0.030 V. Two 0.030 V discrepancies are attributed to two factors: (1) the unknown LJP between SCE and the test solution in the studies of Aranzaes et al and Ahmed and Khan, and (2) the value of potential with respect to SHE of the PdH electrode in the dichloromethane based test solution. (Aranzaes et al. 2006; Ahmed et al. 2007)

Table 12 compares the difference in half-wave potentials of AQ and dmFc, AQ and Fc, and dmFc and Fc measured in the present study (column 2) with the differences reported in the studies by Aranzaes et al. and Ahmed and Khan (column 3).(Aranzaes et al. 2006; Ahmed et al. 2007) In the first two rows of

Table 12, the discrepancies between values obtained by this study and those presented in the literature are relatively large (approximately 0.050V), which is attributed to my use of thoroughly dried DCM and to the use of DCM that was exposed to moisture by Aranzaes et al and Ahmed and Khan.(Aranzaes et al. 2006; Ahmed et al. 2007) When comparing results obtained in this study using wet DCM to those in the literature, the discrepancies (column 4) are small: approximately 0.006 V.

The small values of the discrepancies listed in column 4 of

Table 12 and

Table 13 suggest that PdH serves as a thermodynamic reference electrode in aprotic solutions. The small discrepancies can be accounted for. Assuming that the potential of PdH with respect to SHE in the test solution plus the LJP between SCE and DCM solutions is 0.030V, then the values of the half-wave potentials I measured with respect to PdH of AQ, dmFc and fc are within 0.004 V of the literature values measured

with respect to SCE and converted to SHE. The nearly identical values strongly suggest that PdH serves as a reference electrode in aprotic solutions such as 0.2M [bmim][TFB] in DCM.

The stability of the PdH electrode was investigated by measurements of its potential as a function of time. Figure 89 presents the variation of the potential of PdH measured with respect to a modified saturated calomel electrode in 0.2 M TBAP in ACN saturated with forming gas. The results suggest that the potential of PdH is constant at +0.064 V vs. saturated calomel within ± 0.002 V over a period of 100 minutes. Stability measurements were made in ACN rather than DCM because of the LJP between ACN and DCM.

Reversibility of the PdH electrode was investigated by a small amplitude anodic and cathodic polarization measurements from equilibrium. The small polarization (0 to +10 mV to -10mV) current (I) – voltage (V) behavior of a PdH UME in a two-electrode cell with a PdH CE/RE is presented in Figure 90. The curve obtained by polarization from 0 V to + 0.01 V was identical to the curve obtained when the direction of polarization was reversed and the potential was decreased from +0.01 V to 0 V. In addition, the slope, $\partial i_{net}/\partial \eta|\ \eta->+0$, $\partial i_{net}/\partial \eta|$ measured as $\eta->-0$, as should be the case for a reference electrode. These results indicate that the PdH UME is reversible. So far, the experimental results demonstrate that the PdH UME meets two of the criteria of a reference electrode, namely stability and reversibility.

The polarization data can be used to estimate the value of the exchange current density, i_o, which is used further on in this paper to determine the amount of polarization of PdH CE/RE: $\partial i_{net}/\partial \eta|_{\eta=0} = i_o F/RT = i_o/0.0254V$. From Figure 90, $\partial I_{net}/\partial \eta|_{\eta=0} = 0.0689$ nA/mV. $\therefore$, $i_o = (0.0254V)(0.0689\ nA/mV)/4.56x10^{-5}\ cm^2 = 39.5\ \mu A/cm^2$. Further in the discussion it is demonstrated that the exchange current density of 39.5 $\mu A/cm^2$ is sufficiently large that the PdH CE/RE is polarized only a negligible amount during the cyclic voltammetry tests conducted with a Pt (UME) serving as the working electrode.

To assess the Nernstian behavior of the PdH electrode, experiments were performed that studied the effect of changing the partial pressure of hydrogen on the potential of the PdH electrode. As the Nernst in *equation 9* defines the equilibrium potential of a hydrogen reference, varying hydrogen ion concentration or hydrogen partial pressure should change the potential of the PdH electrode in a predictable manner. However, as the activity of hydrogen ions in aprotic solvents cannot be accurately controlled, only the effect of changing the partial pressure of hydrogen was studied. The experiments were performed using several aprotic solvents: dichloromethane, dimethylsulfoxide, dimethylformamide, and acetonitrile, and the open circuit potential between a PdH electrode and SCE was measured at a partial pressure of hydrogen of 0.04atm and 1atm. The results of the Nernstian experiments in several aprotic solvents are summarized in Table 14. First, the results of the experiments in DMF will be discussed. The experiments with the solvent dimethylformamide displayed Nernstian type behavior. While the magnitude of the potential shift as a result of changing the hydrogen partial pressure is larger than the expected -0.041V (actual value -0.055V), the

direction of the potential shift is consistent with the Nernst equation. Currently, the reason for the larger potential shift than predicted is currently unknown, however the direction of the shift is consistent with a hydrogen based reference electrode.

The equilibrium potentials of palladium hydride measured in the other three solvents (dichloromethane, dimethylsulfoxide, and acetonitrile) also deserve discussion. The equilibrium potential for each of these three solvents changed by approximately +0.037V as the partial pressure of hydrogen was increased from 0.04atm to 1atm. An increase of potential with increasing hydrogen pressure is particularly interesting, as the Nernst equation for a hydrogen electrode predicts a potential change in the opposite direction. The magnitude of the potential shift is consistent with the Nernst equation, but the sign of the potential shift is opposite, which suggests that the PdH electrode may in fact act as an anionic hydride in certain aprotic solvents. If the nature of hydrogen ions on the surface of palladium hydride is anionic, then the potential determining reaction is given by $H_2+2e^-\leftrightarrow 2H^-$, and the potential of the PdH electrode should change by +0.041V in the described experiment. As the palladium hydride system has not been subject to studies in aprotic solvents, there is no evidence in the literature to support the anionic PdH hypothesis. However, there have been reports of homoleptic palladium hydrometalates such as PdH_4^{2-} and PdH_2^{2-}, which does support the possibility of an anionic palladium hydride reference.(King 2000) The nature of hydrogen within palladium hydride will be discussed further later in the discussion, however due to the consistent magnitude of the potential shift, it is tentatively concluded that the palladium hydride system acts in a Nernstian manner in dichloromethane, dimethylsulfoxide, and acetonitrile. However, additional work is required to confirm the existence of hydrogen anions on the surface of PdH immersed in these three solvents before PdH can be used with confidence as a true thermodynamic reference electrode.

Collectively, the aforementioned results presented in Figure 89, Figure 90, Figure 94, and Table 14 provide strong evidence that PdH behaves as a reference electrode in 0.2 [bmim][TFB] in DCM saturated with forming gas.

The remainder of this section is focused on determining how it is that PdH can serve as a reference electrode in an aprotic solution. The results of three additional sets of experiments are presented: CVs conducted with larger voltage amplitudes in aprotic and in aqueous solutions, and potentiostatic tests conducted in aprotic solutions.

The I-V behavior of a PdH UME subjected to cyclic polarizations (i.e., ±0.010V) is presented in Figure 91. The results clearly indicate the presence of a hysteresis. Although the I-V behavior is reproducible in cycle after cycle, the hysteresis indicates the polarization behavior is not reversible, unlike the case for a single polarization. The reason for the hysteresis is likely due to capacitance, and is characteristic of small amplitude cyclic voltammetry in some systems.(Macdonald 1978)

Before considering additional CVs, it is worth confirming that the use of PdH as a combined CE/RE is warranted and that the PdH CE/RE provides an accurate measurement of the WE's potential. The CVs of Pt UME presented in Figure 91 were

measured in a two electrode cell in which ß-PdH served as a RE/CE, and the area ratio of the Pt UME to ß-PdH was $\pi(0.003in./2)^2/1in^2$, which equals $7.07x10^{-6}$. Currents at the Pt UME ran as high as 6 nA. Consequently, the maximum current density that crossed the ß-PdH surface was 6 $nA/1in^2$ = 0.93 nA/cm^2. Based on an exchange current density of 39.5 $\mu A/cm^2$, the maximum polarization of the ß-PdH electrode is only 0.6 µV, which indicates that the ß-PdH served very well as a combination reference electrode/counter electrode in the cell.

The results presented in Figure 92 show that the I-V behavior of a PdH UME subjected to relatively large polarizations in aqueous 0.1M HCl exhibits a hysteresis, just as the voltammogram measured in DCM containing 0.2M [bmim][TFB] did (Figure 91**)**. Collectively, the results in Figure 91 and Figure 92 suggest that the hysteresis in the voltammograms is due to the presence of a capacitive current. To further confirm the origin of the hysteresis, small amplitude cyclic voltammetry experiments were performed with varying scan rates over a slightly larger voltage window (±50mV). The hysteresis data from these experiments are summarized in

Table 15, and the results are consistent with studies of small amplitude cyclic voltammetry done by Macdonald.(Macdonald 1978)

The results indicate that the species oxidized during anodic polarization is hydrogen from ß-PdH or hydrogen anions from ß-PdH. What is especially interesting is the cathodic polarization behavior of ß-PdH in aprotic 0.2M [bmim][TFB] in DCM. The results in 0.2M [bmim][TFB] in DCM indicate that H^+ are available for electrochemical reduction despite the absence of H^+ in the liquid phase, or that H^- is stable as a product of the reduction of hydrogen on the ß-PdH electrode. To rule out the possibility that contaminants such as water might be responsible for the reducible species, similar tests were conducted in which the PdH UME was replaced by a Pt UME. The polarization behavior of Pt was erratic and highly nonreproducible, indicating that PdH was the source of hydrogen ions (H^+ or H^-) in the CVs of UME of PdH.

To confirm that ß-PdH is the source of both oxidation states of hydrogen (H and H^+, or H and H^-), a set of chronoamperometric experiments was conducted. The potential of ß-PdH UME was switched between ± 0.5V vs. PdH for pulse lengths of 5 s, 50 s, and 500 s and current was measured as a function of time. A total of 12 cycles were conducted for pulse lengths of 5 s and 50 s, and 5 cycles for pulse lengths of 500 s. Selected results are presented in Figure 95 - Figure 100. The results of both anodic and cathodic polarizations are similar, namely the current density decreases as the square root of time, although the magnitude of the current density during oxidation is greater than the current density during reduction and the difference in magnitude increased with increasing cycles. Overall, the results are consistent with the hypothesis that the rate-determining step in the oxidation and reduction of hydrogen species in a ß-PdH electrode in 0.2M BMIB TFB in DCM saturated with forming gas is the transport of H from within the ß-PdH to its surface. That is, H dissolved in ß-PdH is the source of both ionization states of hydrogen (H^0 and H^+, or H^0 and H^-).

The final matter for discussion is the nature of the equilibrium at the surface of the ß-PdH immersed in aprotic solutions such as 0.2M [bmim][TFB] in DCM. Essentially, the potential of the ß-PdH consists of the potential difference between the interior of the electrode and hydrogen ions adsorbed on the electrode's surface. The nature of hydrogen ions on the surface of ß-PdH immersed in an aprotic solution deserves some discussion.

The nature of H in palladium has long been considered. Prior to the 1970's it was thought that H existed as protons in palladium. According to the "rigid-energy band" model H simply donated an electron to the empty d-states in palladium but left the palladium's band structure unchanged. However, in the 1970's calculations by Switendick indicated that H fundamentally altered the band structure of palladium.(Switendick 1970; Switendick 1971; Switendick 1972) XPS measurements indicated that H effectively removed states near the Fermi level and added states well below the Fermi level of palladium.(Zbasnik & Mahnig 1976) In the 1980's Chang and Louis calculated that the electrons of palladium effectively screen the proton.(Chan & Louie 1984; Chan & Louie 1983) The proton was in very close proximity to an electron. Effectively, hydrogen was present in palladium in the form of a hydrogen atom. Nevertheless, there is experimental evidence of hydrogen in palladium in the form of protons. For example, a Hall effect associated with the diffusion of hydrogen in palladium indicated the diffusing hydrogen was positively charged.(Verbruggen et al. 1984) Density functional calculations by Luo and Miley suggest the positive charge measured for hydrogen ions during transport in Pd is a consequence of different electron accumulations at various positions occupied by hydrogen when hopping in the Pd lattice.(Luo & Miley 2003) Based upon the calculations of Luo and Miley, the tetrahedral sites have a slightly different hydrogen charge.(Luo & Miley 2003) Simulations suggest that in the octahedral site 82% of the hydrogen 1s electron is shared, while in the tetrahedral sites, 78% of the electrons are shared.(Koroteev et al. 2011) If near the surface, equilibrium can be established between the hydrogen in the octahedral sites and the tetrahedral sites, positive charge of the oxidation of hydrogen to hydrogen ions can then be reincorporated to the lattice by changing the relative concentrations of octahedral and tetrahedral site occupancy. The addition of palladium vacancies near the surface of the hydride can also be used to account for the storage of additional charge. The increased strain due to the vacancies will also assist in stabilizing additional hydrogen atoms in the tetrahedral sites. While the stabilization of hydrogen in tetrahedral sites is known to be active at higher temperatures in the region near the surface additional surface energy and strain due to loading can be used to explain the higher concentration of vacancies than in bulk palladium.(Zaginaichenko et al. 2011; Supryadkina et al. 2014)

It is possible that the different views of the electrical charge on hydrogen in Pd are due to the fact that predictions of electrically neutral hydrogen are based on stationary hydrogen while experimental results and models that indicate the hydrogen is electrically charged are based on moving hydrogen.

While there is a lack of consensus on whether or not hydrogen is electrically charged in bulk PdH, there is very little information on the nature of the charge of H in

the surface of PdH. It is the conjoint presence of H and hydrogen ions in the surface of ß-PdH that allows ß-PdH to serve as a reference electrode in aqueous solutions that are free of H_2 and in nonaqueous, aprotic solutions, such as those investigated in the present study. It is worth noting that the results of Dus' et al. indicate that hydrogen adsorbed on palladium exists, at least in part, as positive and negative ions. Measurements of changes in the surface potential of palladium as a consequence of hydrogen adsorption at 78 K indicated dilute surface concentrations of hydrogen had a negative charge that was changed to a positive charge as the amount of hydrogen adsorption increased.(Dus et al. 1989)

The results suggest that on the surface of β-PdH immersed in an aprotic solution hydrogen is present as both H and hydrogen ions (H^+ or H^-). While additional experiments are required to determine the nature of the hydrogen ions in ß-PdH, the cyclic voltammetry experiments provide evidence that the surface of the PdH electrode contains H and an ionized form of hydrogen. The presence of both hydrogen and hydrogen ions on the surface of PdH are required for PdH to act as a reference electrode. Thus, the electrochemical potential difference between the surface and the interior of PdH provides the potential difference that serves as a hydrogen reference even in aprotic solutions.

Naphthenic Acid Identification by Cyclic Voltammetry

Identification of a suitable ionic liquid and reference electrode allowed for electrochemical testing to be performed in an effort to detect the presence of naphthenic acids in oil. In order to assess whether the acids were in fact redox active in oil solutions, cyclic voltammetry was employed. Previous work has shown that the presence and reactivity of carboxylic acids can be studied in aprotic solvents. (Barrette et al. 1984) The acids selected for this study were single naphthenic acids that were commercially available, and of high corrosivity. (Dettman et al. 2009) The acids selected were cyclohexaneacetic, cyclohexanebutyric, dodecanoic, and stearic acid. These acids represent two saturated fatty acids and two single ringed cycloalkane acids. It should be noted that the current study only looked at a small number of acids that are known to be highly corrosive. Only a small number of acids were investigated due to the commercial unavailability of naphthenic acid structures with more than one ring, and longer alkane chains. The experiments were performed in 0.3M $[P_{6,6,14}][TKIS]$ in toluene with a 0.5mM concentration. The voltammograms presented in Figure 101-Figure 105 show the I-V response of each of the acids, and the analyzed data is presented in Table 16. With the exception of benzoic acid, each of the voltammograms displayed a single wave. The behavior of benzoic acid was surprising where the half wave potential was at the edge of the -2V scan limit. The disparate behavior of benzoic acid is likely due to electroreduction of benzoic acid to benzaldehyde, following a mechanism similar to that described by Atobe and Wagenknecht.(Atobe et al. 1996; Wagenknecht 1972)

To aide in relating the half wave potential to the acid's corrosivity, the effective acidity of each of the acids was calculated. The pKa of the acid was calculated from the half wave potential using the method of Barrrette. (Barrette et al. 1984) The calculated

pKa values were then compared to corrosion rate data to identify whether the effective acidity is a valid metric for determining corrosivity, as shown in Table 17.

Previous work has shown that for weak acids, the half-wave potential shifts based upon the pKa of the acid.(Barrette et al. 1984) The dissociation of the acid releases a proton, which is then available for reduction. The proton is then reduced according to the hydrogen reduction reaction, $2H^+ + 2e^- \rightarrow H_2$. If the hydrogen gas partial pressure is fixed, then the equilibrium potential for the hydrogen reaction will be controlled exclusively by the hydrogen ion activity. In the case of an aprotic solvent, which has a low propensity for solvating hydrogen ions, dissociation of the acid does not easily occur in the bulk. However, the acids will dissociate to a small extent on the surface of the electrode.(Wieckowski 1999) In addition, as long as the large bulky anions generated are stable in the solution, then the anion can diffuse away after the proton has been reduced allowing for continued reduction to occur. The half wave potential of the proton can then be correlated with the reactivity of the acid.

If the reduction of naphthenic acids follows a chemical/electrochemical (CE) mechanism, which is seen in analogous aprotic systems, then the voltammetric response can be used to determine the effective acidity of the structure.(Compton & Banks 2007) The CE mechanism has been applied by other researchers to study the dissociation of acids in aqueous and non-aqueous systems (Kim et al. 2001; Barrette et al. 1984; Kvaratskheliya & Kvaratskheliya 2000; Compton et al. 2012). The first step is chemical, namely the dissociation of the acid, which presumably occurs on the surface of the electrode. The next step is electrochemical, which is the electrochemical reduction of the hydrogen ion to the hydrogen atom, which might then combine with another hydrogen atom to form hydrogen gas on the electrode surface. As the activity of the hydrogen ion is controlled by the dissociation constant of the acid, the hydrogen ion activity in the Nernst Equation can be replaced by the concentration of the acid multiplied by the acid ionization constant (K_a) and divided by the anion activity. The equilibrium potential of the reaction can then be expressed by *equation 12*.

$$\emptyset_{eq} = \emptyset^0 - \frac{RT}{zF} ln\left(\frac{P_{H2}}{(K_a[HA])^2}\right) \quad \{12\}$$

In *equation 12*, K_a is the acid dissociation constant, [HA] is the bulk concentration of the acid, and P_{H2} is the partial pressure of hydrogen, and the other variables are the same as previously mentioned. For calculation of the pKa values, the partial pressure of hydrogen is taken to be 0.04, as the solution is saturated with forming gas. The standard reduction potential of the hydrogen reaction is 0V, and the number of electrons involved in the process is 2. As the partial pressure of the hydrogen gas is a constant, the equilibrium potential, and thus half wave potentials solely change with hydrogen ion activity. The hydrogen ion activity is then controlled by the concentration and dissociation constant of the acid. After obtaining the half wave potentials for all of the acids, the acid dissociation constant was calculated by back solving for K_a. The current of the reduction peak provides information about the concentration of the acid present. While rate constants for each of the acids have not been tabulated, the plateau current

gives information about the concentration and reactivity of the acids. When an UME serves as a working electrode, the steady state reduction current scales proportionately with the concentration of the acid. The values of the pKa calculated for each of the selected acids, along with the corrosion rates measured in this study, as well as the study by Dettman are presented in

Table 17. The disparate corrosion rates of this study and of the Dettman study are likely associated with the differences in TAN, temperature, as well as autoclave configuration.(Dettman et al. 2009)

Acid Structure	$E_{1/2}$ (V)	pKa (Calc)	Corrosion Rate (This Study) mm/yr	Corrosion Rate (Dettman) mm/yr
Stearic	-1.56	24	5.75	1
Benzoic	-2	31.5*	5.5	4.5
Cyclohexaneacetic	-1.4	21.3	8	3
Dodecanoic	-1.55	23.8	7	
Cyclohexanebutyric	-1.18	17.6	6	2.5

Table 17. Relationship between acid structure, pKa, and corrosivity
*Reduction peak of benzoic acid is likely due to reduction of aromatic ring and not carboxylic acid.

The pKa results suggest that cyclohexanebutyric acid is the strongest and most corrosive acid, while benzoic acid is the least corrosive. Another important note is that the voltammetric data is unable to distinguish between dodecanoic and stearic acids. The similar half-wave potentials may be due to the similarity in the structures, as the only difference is the slightly longer alkane chain. The very negative half-wave potential of benzoic acid, which results in an extremely calculated value of its pKa was surprising, as benzoic acid is the strongest acid that was tested. The discrepancy between the high calculated value of benzoic acid's pKa and the acid's high corrosivity, might be due to the low solubility of the carboxylate.(Kim et al. 2001; Maran et al. 1991; Sarmini & Kenndler 1999) As previously mentioned, an inability to solvate the carboxylate would likely result in the reduction of benzoic acid to benzaldehyde. (Sternberg et al. 1963; Atobe et al. 1996; Wagenknecht 1972) The reduction of benzoic acid to benzaldehyde is further supported by a slope analysis of the UME sigmoid, which is consistent with a two-electron process.

To further evaluate whether pKa is an appropriate metric for measuring the corrosivity, the calculated pKa was compared to microbalance corrosion rate measurements and reported corrosion rate measurements from the literature. Figure 118 compares the pKa values calculated using the above method to corrosion rate data from this work, as well as the study by Dettman.(Dettman et al. 2009) A comparison of the results shows little to no correlation between the pKa and the corrosion rate. A possible reason for the lack of correlation is the small number of acids tested, and the absence of larger structures with multiple rings. The data may suggest a maximum corrosivity

associated with a pKa between 18-23, but this cannot be concluded without testing additional acids.

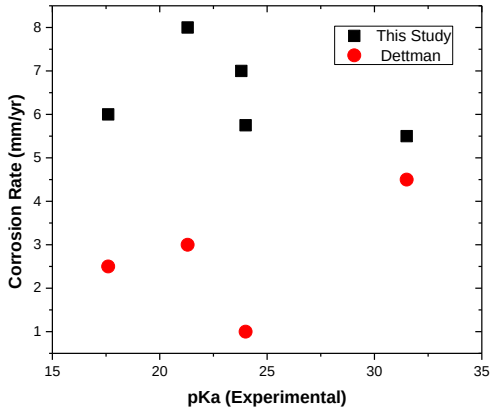


Figure 118. Relationship between calculated pKa and corrosion rate

Another effect that needed to be considered is the solubility of the carboxylate anion in the nonpolar solvent. In aqueous systems, smaller acids have a higher strength, however, in the case of naphthenic acid corrosion, the large acid structures that produce weak acids are corrosive because the iron complex that is formed is solvated by the oil.(Yépez 2007) The studies that have been done thus far indicate a maximum corrosivity for an acid with a carbon number of 9-10, which is presumed to be associated with the maximum solubility of the corrosion product. (Slavcheva et al. 1999; Yépez 2007) The lack of solubility for small naphthenic acids again may be part of the reason for the disparate behavior of benzoic acid, as Yepez showed a drop in the ability of acids to solvate iron below C10.(Yépez 2007) In the literature, the presence of substitutions and heteroatoms on various sites in benzoic acids has been shown to have a great effect on the strength of the acid in benzene.(Davis & Hetzer 1958; Maran et al. 1991; Sarmini & Kenndler 1999) Finally, naphthenic acids produced naturally often contain heteroatoms, which will alter the stability of the carboxylate anion. (Clemente & Fedorak 2005) The results of this study suggest that there may be a maximum corrosivity over a range of pKa, which provides the optimum combination of ease of adsorption, as well ability to be solvated by the oil.

Comparison of the half wave potential with molecular weight and boiling point did not yield any correlation. There was however a weak correlation (R^2=0.5) between the plateau currents of the single acid voltammetry experiments and corrosion rate, as shown in Figure 119. In general, larger steady state currents were associated with higher experimental corrosion rates. Due to the low number of acids tested, a definitive correlation cannot be determined, however the data does suggest a relationship. The relationship between plateau current and corrosivity can be understood most simply as the current associated with the voltammetry experiment is analogous to the reaction rate of the acid on the metal, assuming that the rate-limiting step is the same in both cases. In total, the combination of pKa (half-wave potential) and steady state current provides

information that can be used to estimate the corrosivity of a naphthenic acid containing oil.

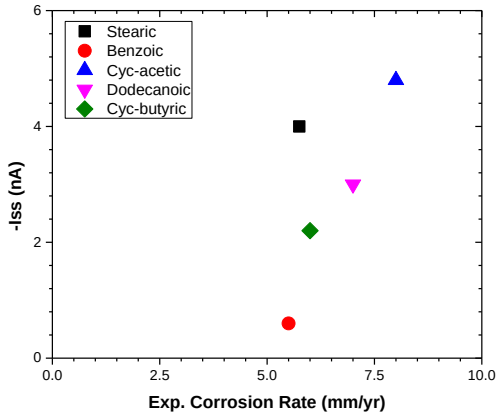


Figure 119. Steady State Current vs. Experimental Corrosion Rate

As the results presented have shown, the cyclic voltammetry technique is able to determine the presence of single naphthenic acids in nonpolar solutions. The electrochemical detection of naphthenic acids is an important incremental step towards improving the ability to detect naphthenic acids in crude oil. Additional testing with larger single naphthenic acids is needed to confirm whether or not pKa is an effective measurement for determining corrosivity. Expanding this study to include heteroatom substitutions in the acid, larger structures containing more cycloalkane rings, as well multiple isomers of complex acid structures will greatly aid in evaluating whether cyclic voltammetry is effective for determining the corrosivity of oils that contain naphthenic acids. Finally, comparison of corrosion data with voltammetry data for a large number of single acids will greatly aid in further evaluating the optimum experimental parameter for association with the corrosivity of naphthenic acids.

Conclusions

Precise monitoring of the corrosion rates in a refinery is of utmost importance because corrosion by the crudes on steel is a serious problem in the oil and gas industry. The new method of microbalance based measurement of dynamic corrosion rates has established that maximum corrosion of the commercial naphthenic acid mixture takes place in the temperature ranges between 290-320^{o}C. The interrupted tests performed on the corroded sample affixed to gallium orthophosphate crystal provided valuable insight into the mechanistic details of the naphthenic corrosion process prevalent in the crudes for decades. The microbalance technique is effective in detecting corrosion at very short times, and therefore can be an indispensable tool for monitoring corrosion in the refinery. The corrosion rates measured by the microbalance technique are comparable to those reported in the literature, making it a very practical method to monitor and mitigate corrosion. Utilization of this technique allows for experimental times to be significantly

reduced, as the mass sensitivity is over 1000 times greater than conventional corrosion measurements.

The corrosion of iron in high temperature mineral oil with three weight percent naphthenic acid was investigated by a combination of dynamic measurements of corrosion rate as a function of time and SEM examination of the corroded surface at various times. Measurements of corrosion rate of iron as a function of time in high temperature oil were made possible by the use of a gallium orthophosphate crystal microbalance. A three-stage corrosion process was indicated by the measurement of corrosion rate versus time. In stage I the iron sample sustained a barely detectable weight loss, which SEM indicated was due to etch pitting of the air-formed oxide. Throughout stage II the corrosion rate increased with time. In stage II, corrosion had locally penetrated the air-formed oxide and the underlying iron was rapidly corroding and undercutting the etch-pitted oxide. Finally, in stage III, the entire surface of the iron sample was corroding and the corrosion rate reached its maximum and steady state value. These results identify the mechanism of failure of carbon steels, and suggest that if the etch pitting of the iron oxide can be stifled, then carbon steel is resistant to NAC. The implication of these results can aid in design of corrosion inhibitors that can be used with carbon steels to stifle acid adsorption on sites that are susceptible to etch pitting.

By looking at iron individually, as well as the common alloying elements used in corrosion resistant alloys, it is possible to elucidate the specific resistance of each of these materials. The metals tested other than iron that actively corroded were copper and zinc. Copper corroded at a rate roughly equivalent of iron for a short time and then stopped, while zinc corroded at an extremely high rate in naphthenic acid media. The reason for corrosion of copper stopping has been attributed to the low corrosion resistance of copper's native oxide. Once the oxide is removed, then the copper metal itself is resistant to naphthenic acid attack. This result is interesting as iron behaves in a completely opposite manner; iron's oxide is resistant to NAC, while the base metal is readily reacted. Chromium, molybdenum, and nickel were resistant to naphthenic acid corrosion in three wt. percent naphthenic acid at 270°C. The mechanism of corrosion inhibition of molybdenum and chromium is the passive oxide formed on these metals. These results suggest that the reason 304 and the 400 series stainless steels are not resistant to naphthenic acid attack is local dissolution / removal of chromium oxide and an inability to reform that oxide. The result of molybdenum corroding without a passive film was surprising, as molybdenum containing alloys are significantly more resistant to naphthenic acid attack. A possible reason for the improved corrosion resistance of Mo bearing alloys is the high stability of molybdenum oxide in crude oil. Nickel was the only material that did not corrode under any of the testing conditions. Nickel formed an NiO type oxide, even in the oxide removal experiments, suggesting that nickel and nickel oxide are resistant to naphthenic acid attack.

Exposure of silicon, nickel, and molybdenum caused a decrease in naphthenic acid concentration even though there was not formation of a metal naphthenate corrosion product. An FT-IR study determined that the naphthenic acids were decarboxylated by exposure to these elements at temperature. The decrease of naphthenic acid

concentration upon exposure to the aforementioned elements suggests that there is another breakdown pathway for these elements, which may account for the resistance of alloys containing them. While all of these elements are expensive, the ability of nickel to remove naphthenic acids from solution may have commercial applications if the low sulfidation resistance of nickel can be overcome. Nickel could be used to remove naphthenic acids in a refinery by addition of a short bed of nickel alloy shavings to at the bottom of the distillation columns or via electrodeposition of a thin nickel layer on to selected areas of refinery piping.

An electrochemical technique for studying the reactivity of naphthenic acids in crude was developed. The electrochemical portion of the work was able to create an ionic liquid that dissociates significantly in low dielectric constant solvents as well as a reference electrode that functions in aprotic solvents. The $[P_{6,6,14}][TKIS]$ ionic liquid is able to reduce the resistivity of toluene by nine orders of magnitude, allowing for electrochemical testing. This novel ionic liquid performs markedly better than other phosphonium based ionic liquids because of its low ability to self-associate due to stearic hindrances. Additionally, the palladium hydride electrode functions as a reference electrode in aprotic solutions. While this research was not able to confirm that palladium hydride is a thermodynamic reference electrode due to the anti-Nernstian behavior that was observed; it does provide insight into how the electrode is able to form a stable potential in solutions that do not contain protons. The anionic model for palladium hydride is able to explain this behavior, and hopefully research in the future will be able to confirm the identity of hydrogen ions on palladium hydride surfaces in nonpolar aprotic solvents. If the equilibrium controlling reaction can be confirmed, then palladium hydride will be the first thermodynamic reference electrode that can function in both protic and aprotic solvents

Finally, by utilizing cyclic voltammetry, the reduction of single naphthenic acids was studied, illustrating that the presence of corrosive acids could be detected with the technique. Single naphthenic acids were able to be detected at the 0.1mM acid concentration, which is much below the threshold for naphthenic acid corrosion in crudes (~1 wt. %). The results suggest that both the half wave potential (pKa) and plateau currents can be used in tandem to identify whether a crude will be corrosive due to naphthenic acid attack. Additional testing with crude oils will determine whether naphthenic acids can be identified uniquely from the mixtures of species present within a crude. The main species of concern for naphthenic acid identification are sulfur species present in crude, however if required naphthenic acids can be isolated from a crude prior to testing.

Future work on this project would include an expansion of the cyclic voltammetry work to include mixtures of acids, as well as more acid structures to further establish the relationship between peak parameters and corrosivity. Determination of guidelines for values of pKa and a minimum threshold current will allow for experimentation on actual crude oil. Additional study into the mechanism of action of the palladium hydride reference electrode is also warranted, as a reference electrode that can function in a wide range of solution chemistries would have broad implications for organic

electrochemistry. The GPCM technique has been successfully applied to naphthenic acid corrosion, and the technique is aptly suited for study of sulfidation corrosion also. As sulfidation is the other major concern for corrosion within the crude distillation unit, this technique can be applied to study sulfidation individually, as well as the interplay between naphthenic acid corrosion and sulfidation. Mechanistic information about sulfidation and the synergistic behavior between sulfidation and naphthenic acid corrosion would be immensely helpful for refiners to predict when failures will occur.

References

Abuhijleh, A.L., 1994. Mononuclear and binuclear copper(II) complexes of the antiinflammatory drug ibuprofen: synthesis, characterization, and catecholase-mimetic activity. *Journal of Inorganic Biochemistry*, 55, pp.255–262.

Ahmadjian, M. & Brown, C.W., 1976. Petroleum Identification by Laser Raman Spectroscopy. *Anal. Chem.*, 48(8), pp.1257–1259.

Ahmed, S. et al., 2007. Hydrogen bonding association in the electroreduced intermediates of benzoquinones and naphthoquinones. *Russian Journal of Electrochemistry*, 43(7), pp.811–819. Available at: http://link.springer.com/10.1134/S1023193507070117 [Accessed April 21, 2014].

Alvisi, P.P. & Lins, V.F.C., 2011. An overview of naphthenic acid corrosion in a vacuum distillation plant. *Engineering Failure Analysis*, 18, pp.1403–1406.

Anamet, I., 2013. *Final Report: Metallurgical Evaluation of Samples from the Chevron U.S.A. Inc., Richmond # Crude Unit*, Hayward, CA.

Anon, 1979. *Corrosion Resistance of Nickel-Containing Alloys in Organic Acids and Related Compounds*, Toronto, Canada: The Nickel Institute.

Anon, 2014a. *CSB Analysis of 2009 Silver Eagle Refinery Accident*, Washington, D.C.

Anon, 2014b. Fractional Distillation Of Crude Oil for Beginners. Available at: http://www.green-planet-solar-energy.com/fractional-distillation-of-crude-oil.html [Accessed May 6, 2014].

Anon, 2013. *Improving Public and Worker Safety at Oil Refineries: Draft Report of the Interagency Working Group on Refinery Safety*, Sacramento, CA.

Anon, 1977. *The Role of Stainless Steels in Petroleum Refining*, Washington, D.C.

Aoki, K., 1993. Theory of Ultramicroelectrodes. *Electroanalysis*, 5, pp.627–639.

Aranzaes, J.R., Daniel, M.-C. & Astruc, D., 2006. Metallocenes as references for the determination of redox potentials by cyclic voltammetry — Permethylated iron and cobalt sandwich complexes, inhibition by polyamine dendrimers, and the role of hydroxy-containing ferrocenes. *Canadian Journal of Chemistry*, 84(2), pp.288–299. Available at: http://www.nrcresearchpress.com/doi/abs/10.1139/v05-262 [Accessed September 9, 2014].

ASTM Standard, D., 2009. Standard Test Method for Acid Number of Petroleum Products by Potentiometric Titration. *ASTM International*, pp.1–10.

Atobe, M., Matsuda, K. & Nonaka, T., 1996. Ultrasonic Effects on Electroorganic Processes. Part 4: Theoretical and Experimental Studies on Product-Selectivity in Electroreduction of Benzaldehyde and Benzoic Acid. *Electroanalysis*, 8(8-9), pp.784–788.

Babaian-Kibala, E., 1993. Naphthenic Acid Corrosion in Refinery Settings. *Materials Performance*, 32(4), pp.50–55.

Babaian-Kibala, E., 1994. Phosphate Ester Inhibitors Solve Naphthenic Acid Corrosion Problems. *Oil and Gas Journal*, pp.31–37.

Bacon, R. & Tordo, S., 2005. *Crude oil price differentials and differences in oil qualities: a statistical analysis*, Washington, D.C. Available at: http://www.esmap.org/sites/esmap.org/files/08105.Technical Paper_Crude Oil Price Differentials and Differences in Oil Qualities A Statistical Analysis.pdf.

Bard, A.J. & Faulkner, L.R., *Electrochemical Methods: Fundamentals and Applications* 2nd ed., New York, NY: Wiley.

Barrette, W.C., Johnson, H.W. & Sawyer, D.T., 1984. Voltammetric Evaluation of The Effective Acidities for Bronstead Acids in Aprotic Solvents. *Anal. Chem.*, 56, pp.1890–1898.

Barrow, M.P. et al., 2003. Determination of the Nature of Naphthenic Acids Present in Crude Oils Using Nanospray Fourier Transform Ion Cyclotron Resonance Mass Spectrometry : The Continued Battle Against Corrosion. *Anal. Chem.*, 75(4), pp.860–866.

Baumgartner, B.M.E. & Raub, C.J., 1988. The electrodeposition of platinum and platinum alloys. *Platinum Metals Rev.*, 32(4), pp.188–197. Available at: http://www.mendeley.com/research/electrodeposition-platinum-platinum-alloys-3/.

Bechmann, R., 1956. Frequency-Temperature-Angle Characteristics of AT-Type Resonators Made of Natural and Synthetic Quartz. *Proceedings of the IRE*, 44, pp.1600–1607.

Behar, F.H. & Albrecht, P., 1984. Correlations between carboxlic acids and hydrocarbons in several crude oils. Alteration by biodegradation. *Organic Geochemistry*, 6, pp.597–604.

Bockris, J., Reddy, A. & Gamboa-Aldeco, M., 2000. *Modern Electrochemistry* 2nd ed., New York, NY: Kluwer.

Bohle, D.S., Kosar, A.D. & Madsen, S.K., 2002. Propionic acid side chain hydrogen bonding in the malaria pigment beta-hematin. *Biochemical and biophysical research communications*, 294, pp.132–135.

Brantley, S.L., 2008. Kinetics of Mineral Dissolution. In S. L. Brantley, J. Kubicki, & A. White, eds. *Kinetics of Water Rock Interaction*. New York, NY, pp. 151–210.

Breen, A.J., 1974. Primary Petroleum Distillation Plant - Selection of Materials. *Br. Corros. J.*, 9(4), pp.197–203.

De Bruyn, H.J., 1998. Naphthenic Acid Corrosion in Synthetic Fuels Production. In *CORROSION Paper No. 576*. NACE.

Buriak, J.M., 2002. Organometallic chemistry on silicon and germanium surfaces. *Chemical reviews*, 102(5), pp.1271–308.

Da Campo, R. et al., 2009. Characterization of Naphthenic Acid Singly Charged Noncovalent Dimers and Their Dependence on the Accumulation Time within a Hexapole in Fourier Transform Ion Cyclotron Resonance Mass Spectrometry. *Energy & Fuels*, 23(11), pp.5544–5549.

Canhoto, C. et al., 2004. Voltammetric analysis of weak acids with microelectrodes. *Journal of Electroanalytical Chemistry*, 570(1), pp.63–67. Available at: http://linkinghub.elsevier.com/retrieve/pii/S0022072804001603 [Accessed April 20, 2014].

Chakravarti, R. et al., 2013. Toward the Mechanism of Corrosion in Crude Oil: A Study Using Vibrational Spectroscopic Techniques at Elevated Temperatures. *Energy & Fuels*, 27(12), pp.7905–7914. Available at: http://pubs.acs.org/doi/abs/10.1021/ef401898e.

Chan, C.T. & Louie, S.G., 1984. Hydrogen in Subsurface Sites of Pd(111): Self-consistent Electronic Structure. *Physical Review B*, 30(8), pp.4153–4163.

Chan, C.T. & Louie, S.G., 1983. Self-consistent pseudopotential calculation of the electronic structure of PdH and Pd4H. *Physical Review B*, 27(6), pp.3325–3337.

Clemente, J.S. & Fedorak, P.M., 2005. A review of the occurrence, analyses, toxicity, and biodegradation of naphthenic acids. *Chemosphere*, 60(5), pp.585–600.

Colthup, N.B., Daly, L.H. & Wiberley, S.E., 1990. *Introduction to Infrared and Raman Spectrscopy* 3rd ed., Boston, MA: Academic Press.

Compton, R.G. & Banks, C.E., 2007. *Understanding Voltammetry*, Hackensack, NJ: World Scientific.

Compton, R.G., Batchelor-McAuley, C. & Dickinson, E.J.F., 2012. *Understanding Voltammetry: Problems and Solution*, Hackensack, NJ: World Scientific.

Connelly, N.G. & Geiger, W.E., 1996. Chemical Redox Agents for Organometallic Chemistry. *Chemical reviews*, 96(2), pp.877–910.

Czarnecki, M. a., 2003. Near-infrared spectroscopic study of self-association of octanoic acid. *Chemical Physics Letters*, 368, pp.115–120.

Davis, J.R., 1996. *Cast Irons*, Materials Park, OH: ASM Intl.

Davis, M.M. & Hetzer, H.B., 1958. Relative strengths of forty aromatic carboxylic acids in benzene at 25-degrees-C. *Journal of Research of the National Bureau of Standards*, 60(6), pp.569–592.

Derungs, W.A., 1956. Naphthenic acid corrosion–an old enemy of the petroleum industry. *Corrosion*, 42, pp.750–758.

Dettman, H.D. et al., 2010. The Influence of Naphthenic Acid and Sulphur Compound Structure on Global Crude Corrosivity under Vacuum Distallation Conditions. In *Northern Area Western Conference*. NACE.

Dettman, H.D., Li, N. & Luo, J., 2009. Refinery Corrosion, Organic Acid Structure, and Athabasca Bithumen. In *CORROSION Paper. No. 09336*. NACE.

Dobson, J.V. & Brims, G., 1987. The Measurement by the (a+b) Palladium Hydride Electrode of the Approximate pH of Phosphate and Acetate Buffer Solution at Elevated Temperatures and Pressures. *Electrochimica Acta*, 32(1), pp.149–153.

Dobson, J.V., Dagless, N. & Thirsk, H.R., 1972. Plateau Potentials of the a+b Palladium Hydride Electrode at Temperatures between 25 and 195C. *J. Chem. Soc., Faraday Trans. 1*, 68, pp.764–772.

Dresseyn, H.O., 1992. *The Chemistry of Funcational Groups, Suppl. B, Vo. 2*, Chichester, UK: Wiley.

Dus, R., Nowicka, E. & Zbiginiew, W., 1989. Surface Phenomena and Isotope Effects at Low Temperature Palladium Hydride Fromation and During Its Decomposition. *Surface Science*, 216, pp.1–13.

Eberle, D.C., 2004. Update on Crude Oil Corrosivity Measurement Techniques Using Radioactive Tracer Technology. , p.31.

Elder, G.B., 1975. *Process Industries Corrosion*, Houston, TX: NACE.

Fahim, M.A., Al-Sahhaf, T.A. & Elkilani, A.S., 2010. *Fundamentals of Petroleum Refining* 1st ed., Oxford, U.K.: Elsevier.

Fan, T.P., 1991. Characterization of Naphthenic Acids in Petroleum by Fast Atom Bombardment Mass Spectrometry. *Energy & Fuels*, 5, pp.371–375.

Farraro, T. & Stellina Jr., R.M., 1996. Materials of construction for Refinery Applications. In *CORROSION Paper No. 614*. NACE.

Flanagan, T.B. & Oates, W.A., 1991a. THE PALLADIUM-HYDROGEN. *Annu. Rev. Mater. Sci.*, 21, pp.269–304.

Flanagan, T.B. & Oates, W.A., 1991b. The Palladium-Hydrogen System. *Annu. Rev. Mater. Sci.*, 21, pp.269–304.

Fraser, K.J. et al., 2007a. Liquids intermediate between "molecular" and "ionic" liquids: Liquid Ion Pairs? *Chemical Communications*, (37), p.3817. Available at: http://xlink.rsc.org/?DOI=b710014k [Accessed June 18, 2014].

Fraser, K.J. et al., 2007b. Liquids Intermediate Between "Molecular" and "Ionic" Liquids: Liquid Ion Pairs? *Chemical Communications*, pp.3817–3819. Available at: http://xlink.rsc.org/?DOI=b710014k [Accessed June 18, 2014].

Fraser, K.J. & MacFarlane, D.R., 2009. Phosphonium-Based Ionic Liquids: An Overview. *Australian Journal of Chemistry*, 62, pp.309–321. Available at: http://www.publish.csiro.au/?paper=CH08558.

Fu, J. et al., 2006. Nonpolar Compositional Analysis of Vacuum Gas Oil Distillation Fractions by Electron Ionization Fourier Transform Ion Cyclotron Resonance Mass Spectrometry. *Energy & Fuels*, 20(2), pp.661–667.

Gagne, R.R., C.A., K. & Lisensky, G.C., 1980. Ferrocene as an Internal Standard for Electrochemical Measurements. *Inorg. Chem.*, 19, pp.2854–2855.

Garverick, L., 1994. *Corrosion in the Petrochemical Industry*, Materials Park, OH: ASM Intl.

Gary, J.H. & Handwerk, G.E., 1994. *Petroleum Refining - Technology and Economics* 3rd ed., New York, NY: Marcel Dekker.

Gelder, J.D. et al., 2007. Reference Database of Raman Spectra of Biological Molecules. *Journal of Raman Spectroscopy*, 38, pp.1133–1147.

Gibson, N. & Lloyd, F.C., 1970. Electrification of Toluene Flowing in Large-diameter Metal Pipes. *J. Phys. D*, 3, pp.563–573.

Graedel, T.E., Franey, P. & Kammlott, G.W., 1983. The Corrosion of Copper by Atmospheric Sulphurous Gases. *Corrosion Science*, 23(11), pp.1141–1152.

Gritzner, G. & Kuta, J., 1984. Recommendations of Reporting Electrode Potentials in Nonaqueous Solvents, IUPAC Commission on Electrochemistry. *Electrochimica Acta*, 29(6), pp.869–873.

Guo, D.J. et al., 2005. Reaction of porous silicon with both end-functionalized organic compounds bearing alpha-bromo and omega-carboxy groups for immobilization of biomolecules. *The journal of physical chemistry. B*, 109(43), pp.20620–20628.

Gupta, N. & Linschitz, H., 1997. Hydrogen-Bonding and Protonation Effects in Electrochemistry of Quinones in Aprotic Solvents. *J. Am. Chem. Soc.*, 119, pp.6384–6391.

Gutzeit, J., 1977. Naphthenic Acid Corrosion in Oil Refineries. *Materials Performance*, 16(10), pp.24–35.

Harper, J.M.E., 1996. Effect of Hydrogen Concentration on Superconductivity and Clustering in Palladium Hydride. *Physics Letters A*, 47A(1), pp.69–70.

Hartley, F.R. ed., 1987. *The Chemistry of the Metal - Carbon Bond: Volume 4*, Chichester, UK: Wiley.

Hau, J., 2009. Predicting Sulfidic and Naphthenic Acid Corrosion. *Corrosion*, 65(12), pp.831–844.

Hau, J.L. et al., 1999. The Iron Powder Test of Naphthenic Acid Corrosion Studies. In *CORROSION Paper No. 379*. NACE.

Ho, T.Y. et al., 1974. Evolution of Sulfur Compounds in Crude Oils. *The American Association of Petroleum Geologists Bulletin*, 58(11), pp.2338–2348.

Holowenko, F.., Mackinnon, M.D. & Fedorak, P.M., 2002. Characterization of Napthenic Acids in Oil Sands Wastewaters by Gas Chromatography-Mass Spectrometry. *Water Research*, 36, pp.2843–2855.

Holowenko, F.M., MacKinnon, M.D. & Fedorak, P.M., 2001. Naphthenic acids and surrogate naphthenic acids in methanogenic microcosms. *Water Research*, 35(11), pp.2595–2606.

Hsu, C.S. et al., 2000. Naphthenic Acids in Crude Oils Characterized by Mass Spectroscopy. *Energy and Fuels*, 14, pp.217–223.

Hughey, C.A., Rodgers, R.P. & Marshall, A.G., 2002. Resolution of 11,000 compositionally distinct components in a single electrospray ionization Fourier

transform ion cyclotron resonance mass spectrum of crude oil. *Analytical chemistry*, 74(16), pp.4145–9.

Hui, Y. et al., 2010. Voltammetric method for determining the trace moisture content of organic solvents based on hydrogen-bonding interactions with quinones. *Analytical chemistry*, 82(5), pp.1928–34. Available at: http://www.ncbi.nlm.nih.gov/pubmed/20143888.

Humphries, M. & Sorell, G., 1976. Corrosion Contrl in Crude Oil Distillation. *Materials Performance*, 15(2), pp.13–21.

Hunger, J., Stoppa, A. & Cuchner, R., 2008. From Ionic Liquid to Electrolte Solution: Dynamics of 1-N-Butyl-3M-Methylimidazolium Tetrafluoroborate / Dichloromethane Mixtures. *J. Phys. Chem. B.*, 112(41).

Ives, D.J.G. & Janz, G.J. eds., 1961. *Reference Electrodes: Theory and Practice* 1st ed., Waltham, MA: Academic Press.

Kanazawa, K.K. & Gordon II, J.G., 1985. The Oscillaton Frequency of a Quartz Resonator in Contact with a Liquid. *Analytica Chimica Acta*, 175, pp.99–105.

Kanukuntla, V. et al., 2009. Experimental Study of Concurrent Naphthenci aCid and Sulfidation Corrosion. In *Paper No. 2764*. pp. 1–21.

Kaye, G.W.C. & Laby, T.H., 1995. *Tables of physical and chemical constants* 16th ed., Essex, England: Longman.

Kelesoglu, S. et al., 2012. Adsorption of Naphthenic Acids onto Mineral Surfaces Studied by Quartz Crystal Microbalance with Dissipation Monitoring (QCM-D). *Energy & Fuels*, 26, pp.5060–5068.

Kim, H.S., Chung, T.D. & Kim, H., 2001. Voltammetric Determination of the pKa of Various Acids in Polar Aptrotic Solvents Using 1,4-benzoquinone. *Journal of Electroanalytical Chemistry*, 498, pp.209–215.

King, R.B., 2000. Structure and bonding in homoleptic transition metal hydride anions. *Coordination Chemistry Reviews*, 200-202, pp.813–829.

Koroteev, Y.M., Gimranova, O.V. & Chernov, I.P., 2011. Hydrogen Migration in Palladium: First-Principles Calculations. *Physics of the Solid State*, 53(5), pp.896–900. Available at: http://link.springer.com/10.1134/S1063783411050143 [Accessed April 25, 2014].

Koteswaram, P., 1939. Molecular Association in Fatty Acids. *J. Chem. Phys.*, 88(7), p.88.

Krempl, P.W., 1997. Quartzhomeotypic gallium orthophosphate: A new high-tec piezoelectric crystal. *Ferroelectrics*, 202(1), pp.65–69.

Kruger, J., 2011. Cost of metallic corrosion. In R. W. Revie, ed. *Uhlig's Corrosion Handbook*. New York, NY: Wiley, pp. 15–20.

Kumar, A., 2000. Biosensors Based on Piezoelectric Crystal Detectors: Theory and Application. *JOM*, 52(10).

Kvaratskheliya, R.K. & Kvaratskheliya, E.R., 2000. Voltammetry of Dicarboxylic Acids on Solid Electrodes in Aqueous and Mixed Media. *Russian Journal of Electrochemistry*, 36(3), pp.369–373.

Lewis, B.F.A., 1982. The Palladium-Hydrogen System A SURVEY OF HYDRIDE FORMATION AND THE EFFECTS. , (l), pp.20–27.

Lewis, F.A., 1960. The Hydrides of Palladium and Palladium Alloys. *Platinum Metals Rev.*, 4(4), pp.132–137.

Lewis, F.A., 1982. The Palladium-Hydrogen System. *Platinum Metals Rev.*, 26(1), pp.20–27.

Liphard, M. et al., 1980. Adsorption of Carboxyli Acids and Other Chain Molecules from n-heptane onto Graphite. *Progr. Colloid and Polymer Sci.*, 67, pp.131–140.

Lu, C.S. & Lewis, O., 1972. Investigation of film-thickness determination by oscillating quartz resonators with large mass load. *J. Appl. Phys.*, 43(11), pp.4385–4390.

Luo, N. & Miley, G.H., 2003. First-Principles Studies Of Ionic And Electronic Transport In Palladium Hydride. *10th International Conference on Cold Fusion*.

Macdonald, D.D., 1978. An Impedance Interpretation of Small Aplitude Cyclic Voltmmetry. *J. Electrochem. Soc.*, 125(9), p.14431449.

Maran, F. et al., 1991. Electrochemical determination of the pKa of weak acids in N,N-dimethylformamide.pdf. *J. Am. Chem. Soc.*, 113(d), pp.9320–9329.

Marshall, A.G. & Rodgers, R.P., 2004. Petroleomics : The Next Grand Challenge for Chemical Analysis Petroleum and Mass Spectrometry : Divergent. *Accounts of Chemical Research*, 37, pp.53–59.

Martin, S.J., Granstaff, V.E. & Frye, G.C., 1991. Characterization of a Quartz Crystal Microbalance with Simultaneous Mass and Liquid Loading. *Anal. Chem.*, 63, pp.2272–2281.

Mehrota, R.C. & Bohra, R., 1983. *Metal Carboxylates*, London, UK: Academic Press.

Meredith, W., Kelland, S. & Jones, D.M., 2000. Influence of biodegradation on crude oil acidity and carboxylic acid composition. *Organic Geochemistry*, 31, pp.1059–1073.

Mohammed, M.A. & Sorbie, K.S., 2009. Naphthenic Acid Extraction and Characterization from Naphthenate Field Deposits and Crude Oils using ESMS and APCI-MS. *Colloids and Surfaces A: Physiochemical Engineering Aspects*, 349, pp.1–18.

Morris, J., MSE 200 Reader.

Nace, D.M. & Aston, J.G., 1957. Palladium Hydride I: The Thermodynamic Properties of Pd2H Between 273 and 345K. *J. Am. Chem. Soc.*, 79, p.3619.

Nakabayashi, T. & Nishi, N., 2002. States of molecular associates in binary mixtures of acetic acid with protic and aprotic polar solvents: A Raman spectroscopic study. *Journal of Physical Chemistry A*, 106, pp.3491–3500.

Newman, J., 1966. Resistance for Flow of Current to a Disk. *Journal of The Electrochemical Society*, 113(5), pp.501–502.

Ng, J.B. & Shurvell, H.F., 1987. Application of factor analysis and band contour resolution techniques to the Raman spectra of acetic acid in aqueous solution. *The Journal of Physical Chemistry*, 91(17), pp.496–500. Available at: http://pubs.acs.org/doi/abs/10.1021/j100286a046.

Nishi, Y. & Doering, R. eds., 2007. *Handbook of Semiconductor Manufacturing Technology*, Boca Raton, FL: CRC Press.

Nugent, M.J. & Dobis, J.D., 1998. Experience with Naphthenic Acid Corrosion in Low TAN Crudes. In *CORROSION Paper No. 577*. NACE, p. 8.

Okada, Y., 1998. *Properties of Crystalline Silicon* 1st ed. R. Hull, ed., Stevenage, U.K.: INSPEC.

Oliveira, M.C.F., 2006. A new approach to prepare highly loaded palladium. *Electrochemistry Communications*, 8, pp.647–652.

Orzazem, M. & Tribollet, B., 2008. *Electrochemical Impedance Spectroscopy*, New York, NY: Wiley.

Palacios, E.G., Juárez-López, G. & Monhemius, a. J., 2004. Infrared spectroscopy of metal carboxylates: II. Analysis of Fe(III), Ni and Zn carboxylate solutions. *Hydrometallurgy*, 72, pp.139–148.

Patrick, B.N., Chakravarti, R. & Devine, T.M., 2015a. Dynamic measurements of corrosion rates at high temperatures in high electrical resistivity media. *Corrosion*

Science, 94, pp.99–103. Available at: http://linkinghub.elsevier.com/retrieve/pii/S0010938X15000566.

Patrick, B.N., Chakravarti, R. & Devine, T.M., 2015b. Dynamic measurements of corrosion rates at high temperatures in high electrical resistivity media. *Corrosion Science*, 94, pp.99–103.

Pavlishchuk, V. & Addison, A., 2002. Converson Constants for Redox Potentials Measured Versus Different Reference Electrodes in Acetonitrile Solutions at 25C. *Inorganica Cheimica Acta*, 298, pp.97–102.

Pham, H.H., Taylor, C.D. & Henson, N.J., 2013. First-principles prediction of the effects of temperature and solvent selection on the dimerization of benzoic acid. *Journal of Physical Chemistry B*, 117, pp.868–876.

Piehl, R.L., 1959. Correlation of Corrosion In a Crude Distillation Unit with Chemistry of the Crudes. *Corrosion*, 15, pp.139–141.

Piehl, R.L., 1988. Naphthenic Acid Corrosion in Crude Distillation Units. *Materials Performance*, 27(1), pp.37–43.

Pons, S. & Khoo, S.B., 1981. Reductions in Aprotic Media-I Cathodic Reduction Limits at a Platinum Electrode in Acetonitrile. *Electrochimica Acta*, 27(9), pp.1161–1169.

Qu, D.R. et al., 2007. Correlation between the corrosivity of naphthenic acids and their chemical structures. *Anti-Corrosion Methods and Materials*, 54(4), pp.211–218.

Qu, D.R. et al., 2006. High temperature naphthenic acid corrosion and sulphidic corrosion of Q235 and 5Cr1/2Mo steels in synthetic refining media. *Corrosion Science*, 48(8), pp.1960–1985.

Ramadan, K.S., Sameoto, D. & Evoy, S., 2014. A review of piezoelectric polymers as functional materials for electromechanical transducers. *Smart Materials and Structures*, 23(033001), p.26.

Rappoport, Z. & Marek, I. eds., 2006. *The Chemistry of Organozinc Compounds*, Chichester, UK: Wiley.

Reynolds, J.G., 2007. Nickel in Petroleum Refining. *Petroleum Science and Technology*, 19(7-8), pp.979–1003.

Rogers, V.V., Liber, K. & Mackinnon, M.D., 2002. Isolation and Characterization of Naphthenic Acids from Athabasca Oil Sands Tailings Pond Water. *Chemosphere*, 48, pp.519–527.

Ryde, U., 1999. Carboxylate binding modes in zinc proteins: a theoretical study. *Biophysical journal*, 77(November), pp.2777–2787.

Saab, J. et al., 2005. Quantitative Extraction Procedure of Naphthenic Acids Contained in Crude Oils. Characterization with Different Spectroscopic Methods. *Energy and Fuels*, 19, pp.525–531.

Sakintuna, B., Lamaridarkrim, F. & Hirscher, M., 2007. Metal Hydride Materials for solid Hydrogen Storage: A Review. *International Journal of Hydrogen Energy*, 32(9), pp.1121–1140.

Sarı, A. & Kaygusuz, K., 2003. Some Fatty Acids Used for Latent Heat Stormage: Thermal Stability and Corrosion of Metals with Respect to Thermal Cycling. *Renewable Energy*, 28(6), pp.939–948.

Sarmini, K. & Kenndler, E., 1999. Ionization constants of weak acids and bases in organic solvents. *Journal of biochemical and biophysical methods*, 38(2), pp.123–137.

Sauerbrey, G., 1959. Verwendung von Schwingquarzen zur Wagungdiinner Schichten und zur Mikrowagung. *Zeitschrift fur Physik*, 155, pp.206–222.

Saxena, R.C., 2013. Corrosion Control of Heavy Crude in Refineries. *Chemical Industry Digest*, pp.53–58.

Schuldiner, S., Castellan, W. & Hoare, J.P., 1958. Electrochemical Behavior of the Palladium-Hydrogen System. I. Potential-Determining Mechanisms. *The Journal of Chemical Physics*, 28(1), pp.16–19.

Schultz, J.W. et al., 1989. Prospects and Problems of Electrochemically Induced Cold Nuclear Fusion. *Electrochimica Acta*, 34(9), pp.1289–1313.

Seifert, W.K. & Teeter, R.M., 1970. Identification of Polycyclic Naphthenic, Mono-, and Diaromatic Crude Oil Carboxylic Acids. *Analytical chemistry*, 42(2), pp.180–189.

Setterlund, R.B., 2007. Selecting Process Piping Materials. *Element Materials Technology*, 2007, pp.1–7. Available at: http://www.element.com/docs/technical-articles/technicalarticle_selectingprocesspipingmaterials.pdf?Status=Master.

Simanzhenkov, V. & Idem, R., 2003. *Crude Oil Chemistry*, New York, NY: Marcel Dekker.

Slavcheva, E., Shone, B. & Turnbull, A., 1999. Review of naphthenic acid corrosion in oil refining. *British Corrosion Journal*, 34(2), pp.125–131.

Smith, D.F. et al., 2009. Effect of thermal treatment on acidic organic species from athabasca bitumen heavy vacuum gas oil, analyzed by negative-ion electrospray fourier transform ion cyclotron resonance (FT-ICR) mass spectrometry. *Energy and Fuels*, 23(5), pp.314–319.

Smith, D.F. et al., 2007. Self-association of organic acids in petroleum and Canadian bitumen characterized by low- and high-resolution mass spectrometry. *Energy and Fuels*, 21(12), pp.1309–1316.

Smits, F.M., 1958. Measurement of Sheet Resistivities with the Four-Point Probe. *Bell Labs Technical Journal*, 37(3), pp.711–718.

Socrates, G., 2004. *Infrared and Raman Characteristic Group Frequencies* Third., New York, NY: Wiley.

Spink, G.M. & Ives, M.B., 1971. Morphology of Crystallographic Etch Pits in Iron. *Journal of Applied Physics*, 42(2), pp.511–515.

Stahl, K.-E. Von & Ke, W., 2002. Corrosion and erosion-corrosion behaviors of carbon steel in naphthenic acid media. , 844, pp.833–844.

Sternberg, H.W., Markby, R. & Wender, I., 1963. Electrochemical Reduction of the Benzene Ring. *Journal of The Electrochemical Society*, 110(5), p.425.

Stienhem, C. & Janshoff, A. eds., 2006. *Piezoelectric Sensors*, New York, NY: Springer.

Stock, J.T. & Purdy, W.C., 1957. Potentiometreic Electrode Systems in Nonaqueous Titrimetry. *Chemical reviews*, 57(6), pp.1159–1171.

Sunder, S., Mendelsohn, R. & Bernstein, H.J., 1976. Raman Studies of the C-H and C-D Stretching Regions in Stearic Acid and Some Specifically Deuterated Derivatives. *Chemistry and Physics of Lipids*, 17, pp.456–465.

Supryadkina, I.A., Bazhanov, D.I. & Ilyushin, A.S., 2014. Ab initio study of the formation of vacancy and hydrogen-vacancy complexes in palladium and its hydride. *Journal of Experimental and Theoretical Physics*, 118(1), pp.80–86.

Switendick, A.C., 1970. Electronic Band Structures of Metal Hydrides. *Solid State Comm.*, 8, pp.1463–1467.

Switendick, A.C., 1972. Electronic Energy Bands of Metal Hydrides - Palladium and Nickel Hydride. *Berichte der Bunsengesellschaft für physikalische Chemie*, 76(6), pp.535–542.

Switendick, A.C., 1971. Metal Hydrides-Structure and Band Structure. *Int. J. Quant. Chem.*, 470(5), pp.459–470.

Szab'o, S. & Bkos, J., 2010. Reference Electrodes in Metal Corrosion. *International Journal of Corrosion*, 2010.

Tanaka, N., Kitano, H. & Ise, N., 1991. Raman Spectroscopic Study of Hydrogen Bonding in Aqueous Carboxylic Acid Solutions. *J. Phys. Chem.*, 94, pp.6920–6292.

Templeton, H.C., 1970. Corrosion of Alloys in Tall Oil Distillation Service. *J. Am. Oil Chemists' Soc.*, 47, p.138A–.

Thanner, H. et al., 2002. GaPO4 high temperature crystal microbalance with zero temperature coefficient. *Vacuum*, 67(3), pp.687–691.

Tokuda, H. et al., 2006. How ionic are room-temperature ionic liquids? An indicator of the physicochemical properties. *Journal of Physical Chemistry B*, 110(39), pp.19593–19600.

Tokuda, H. et al., 2004. Physicochemical Properties and Structures of Room Temperature Ionic Liquids. 1. Variation of Anionic Species. *The Journal of Physical Chemistry B*, 108(42), pp.16593–16600. Available at: http://pubs.acs.org/doi/abs/10.1021/jp047480r.

Tomczyk, N.A. & R.E., W., 2001. On the Nature and Origin of Acidic Species in Petroleum. 1. Detailed Acid Type Distribution in a California Crude Oil. *Energy and Fuels*, 15, pp.1498–1504.

Tooke et al., Infrared and Raman Spectroscopy, Vol. 1 Pt. B. In E. G. Brame & J. G. Graselli, eds. *Infrared and Raman Spectroscopy, Vol. 1 Pt. B*. New York, NY: Dekker.

Turnbull, A., Slavcheva, E. & Shone, B., 1998. Factors Controlling Naphthenic Acid Corrosion. *Corrosion*, 54(11), pp.922–930.

Vasile, M.J. & Enke, C.G., 1965. The Preparation and Thermodynamic Properties of a Palladium-Hydrogen Electrode. *Journal of The Electrochemical Society*, 112(8), p.865. Available at: http://jes.ecsdl.org/cgi/doi/10.1149/1.2423713.

Verbruggen, A.H., Griessen, R. & Rector, J.H., 1984. Hall Voltage Induced by Hydrogen Diffusion in Palladium. *Physical Review Letters*, 52(18), pp.1625–1628.

Virmani, Y.P., 2003. The United States Cost of Corrosion Study. *NACE International*. Available at: http://www.nace.org/Publications/Cost-of-Corrosion-Study/ [Accessed May 6, 2014].

Wagenknecht, J.H., 1972. Electrochemical reduction of aromatic acids to the corresponding aldehydes. *The Journal of Organic Chemistry*, 37(10), pp.1513–1516. Available at: http://pubs.acs.org/doi/abs/10.1021/jo00975a010.

Walch, R., 2008. Bond Dissociation Energies in Organosilicon Compounds. In B. Arkles & G. Larson, eds. *Silicone Compound: Silanes and Silicones*. Morrisville, PA: Gelest Inc.

Wang, M. & Yao, S., 2002. A Long Term Stable Iridium Oxide pH Electrode. *Sensors and Actuators*, 81(313-325).

Washburn, E.W. ed., *International Critical Tables of Numerical Data, Physics, Chemistry and Technology (1st Electronic Edition)* 1st ed., New York, NY: Knovel.

Weaver, E.R., 1920. The Generation of Hydrogen by the Reaction Between Ferrosilicon and a Solution of Sodium Hydroxide. *The Journal of Industrial and Engineering Chemistry*, 12(3), pp.232–240.

Whitby, C., 2010. Microbial Naphthenic Acid Degradation. *Advances in Mpplied microbiology*, 70, pp.93–125.

Wieckowski, A., 1999. *Interfacial Electrochemistry: Theory: Experiment, and Applications*, Boca Raton, FL: CRC Press.

Wu, N. et al., 2004. Interaction of Fatty Acid Monolayers with Cobalt Nanoparticles. *Nano Letters*, 4(2), pp.383–386.

Wu, X. et al., 2004. Erosion–corrosion of various oil-refining materials in naphthenic acid. *Wear*, 256, pp.133–144.

Wu, X.Q. et al., 2004. Resistance of Mo-bearing stainless steels and Mo-bearing stainless-steel coating to naphthenic acid corrosion and erosion–corrosion. *Corrosion Science*, 46(4), pp.1013–1032.

Wynd, F.L., 1935. A Note on the Application of the Glass Electrode to the Determination of Oxidation-Reduction Potentials. *Annals of the Missouri Botanical Garden*, 22(4), pp.861–865.

Yang, B.B. et al., 2013. Thermal transformation of acid compounds in high TAN crude oil. *Science China Chemistry*, 56(7), pp.848–855.

Yépez, O., 2005. Influence of different sulfur compounds on corrosion due to naphthenic acid. *Fuel*, 84(1), pp.97–104.

Yépez, O., 2007. On the chemical reaction between carboxylic acids and iron, including the special case of naphthenic acid. *Fuel*, 86, pp.1162–1168.

Yu, J., Jiang, L. & Gan, F., 2008. High temperature naphthenic acid corrosion of steel in high TAN refining media. *Anti-Corrosion Methods and Materials*, 55(5), pp.257–263.

Zaginaichenko, S.Y. et al., 2011. The structural vacancies in palladium hydride. Phase diagram. *International Journal of Hydrogen Energy*, 36(1), pp.1152–1158.

Zbasnik, J. & Mahnig, M., 1976. The Electronic Structure of Beta-Phase Palladium Hydride. *Z. Physik B*, 23, pp.15–21.

Zhang, S. & Yu, F., 2011. Piezoelectric Materials for High Temeprature Sensors. *J. Am. Ceram. Soc.*, 94(10), pp.3153–3170.